THE OHIO STATE UNIVERSITY

BISTATIC SCATTERING FROM A CONE FRUSTUM

by

W. Ebihara and R.J. Marhefka

The Ohio State University

ElectroScience Laboratory

Department of Electrical Engineering
Columbus, Ohio 43212

Technical Report No. 716148-16
Grant No. NSG 1613
August 1986

National Aeronautics and Space Administration
Langley Research Center
Hampton, VA 23665

and

Naval Air Station
Pacific Missile Test Center
Point Mugu, CA 93042

NOTICES

When Government drawings, specifications, or other data are used for any purpose other than in connection with a definitely related Government procurement operation, the United States Government thereby incurs no responsibility nor any obligation whatsoever, and the fact that the Government may have formulated, furnished, or in any way supplied the said drawings, specifications, or other data, is not to be regarded by implication or otherwise as in any manner licensing the holder or any other person or corporation, or conveying any rights or permission to manufacture, use, or sell any patented invention that may in any way be related thereto.

50272-101

REPORT DOCUMENTATION PAGE	1. REPORT NO. 716148-16	2.	3. Recipient's Accession No.

4. Title and Subtitle

BISTATIC SCATTERING FROM A CONE FRUSTUM

5. Report Date: August 1986

6.

7. Author(s)

W. Ebihara and R.J. Marhefka

8. Performing Organization Rept. No. 716148-16

9. Performing Organization Name and Address

The Ohio State University
ElectroScience Laboratory
1320 Kinnear Road
Columbus, Ohio 43212

10. Project/Task/Work Unit No.

11. Contract(C) or Grant(G) No.

(C)

(G) NSG-1613

12. Sponsoring Organization Name and Address **DUAL SPONSORSHIP**

National Aeronautics & Space Admin.
Langley Research Center
Hampton, VA 23665

Naval Air Station
Pacific Missile Test Ctr.
Point Mugu, CA 93042

13. Type of Report & Period Covered: Technical Report

14.

15. Supplementary Notes

16. Abstract (Limit: 200 words)

The bistatic scattering from a perfectly conducting cone frustum is investigated using the Geometrical Theory of Diffraction (GTD). The first-order GTD edge-diffraction solution has been extended by correcting for its failure in the specular region off the curved surface and in the rim-caustic regions of the endcaps. The corrections are accomplished by the use of transition functions which are developed and introduced into the diffraction coefficients. Theoretical results are verified in the principal plane by comparison with the moment method solution and experimental measurements. The resulting solution for the scattered fields is accurate, easy to apply, and fast to compute.

17. Document Analysis a. Descriptors

b. Identifiers/Open-Ended Terms

c. COSATI Field/Group

18. Availability Statement	19. Security Class (This Report) Unclassified	21. No. of Pages 163
	20. Security Class (This Page) Unclassified	22. Price

(See ANSI-Z39.18) See Instructions on Reverse

OPTIONAL FORM 272 (4-77)
(Formerly NTIS-35)
Department of Commerce

TABLE OF CONTENTS

LIST OF FIGURES

LIST OF TABLES

CHAPTER I

Introduction

1.1 Objective and Motivation

In this thesis, the electromagnetic scattering from a cone frustum is investigated using the high-frequency techniques of the geometrical theory of diffraction. The emphasis in this work is on the development of a solution which, besides being accurate, is easy to apply and fast to calculate. In other words, we want a solution suitable for engineering applications. Even though the scattering from basic shapes, like the cone frustum, is fundamental, there is much to be gained from its study.

The solution to such a problem can give insight into the development of solutions to other scattering problems. There are many subtleties that need to be considered when the solution to the scattered fields of such a geometry is attempted; the experience gained may be applied to similar situations in other geometries. In fact, the topic of this thesis was inspired by the recent work of Kuei-Chien Chiang [1] who investigated the scattering from a cylinder.

From a more practical standpoint, the study of high-frequency scattering from basic geometrical shapes has applications in the modeling of complex scatterers. Due to the highly local nature of high-frequency scattering, the solution to complex scatterers may be modeled approximately as a superposition of the scattered fields from simpler shapes—such as cone frustums, cylinders, ellipsoids, plates, and oth-

ers. A fast and accurate solution for these basic geometries may lead to analytical computer-generated scattering patterns for aircraft, ships, reflector antennas, or even a space station. This can result in the computer design of scatterers to meet various engineering specifications.

1.2 The Problem

This is an electromagnetic scattering problem. The objective is to find the scattered electric and magnetic fields for a known incident illumination of the scatterer. The scattered fields consist of those fields that are reflected and diffracted from the scatterer. For this problem let us specify the following conditions:

- Shape—elliptical right cone frustum (see Figure 1)
- Material—perfect conductor in free space
- Size—greater than a wavelength (high frequencies)
- Illumination—a plane wave polarized in either of the orthogonal polarizations (vertical or horizontal)
- Observation—bistatic, in the far field with matched polarization

The variables in this problem are

- Frequency
- Polarization
- Positions of source and receiver
- Cone frustum dimensions

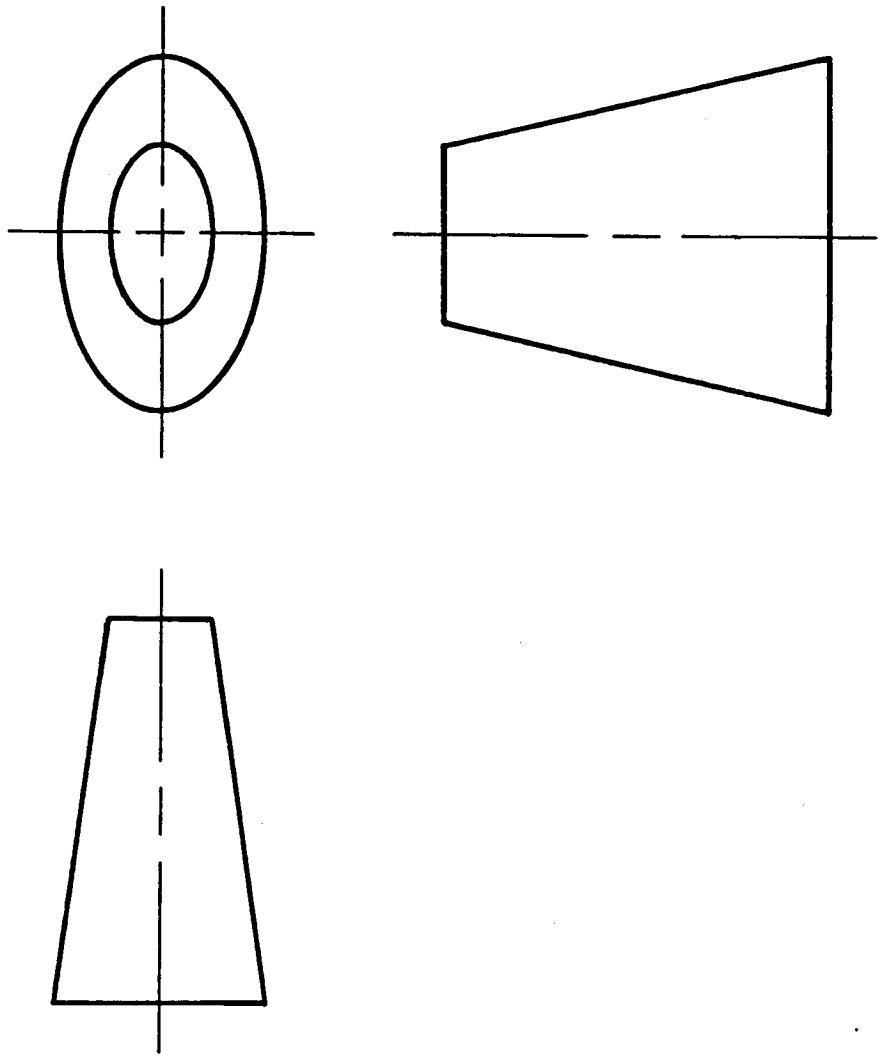

Figure 1: An elliptical right cone frustum

1.3 Solution Strategy

To solve our problem, we depend a great deal on the work which has been done in the past. We mentioned previously that a techinique called the geometrical theory of diffraction (GTD) would be used. It was originally developed by Keller [2], and it has been improved by many others which include the work of Kouyoumjian and Pathak [3]. The improved version of GTD, which corrects the areas where Keller's original theory had failed, is usually referred to as the uniform geometrical theory of diffraction (UTD). A brief background on UTD is provided in Chapter 2.

In the past, GTD has been applied to the scattering from a circular cone frustum by Bectel and Ross [4,5,6] and Ryan and Peters [7]. The GTD solution consists of a superposition of high-frequency semi-infinite wedge solutions associated with each local scattering center at the edges. The total scattered field is obtained by summing the diffracted fields from each scattering center. (Chapter 3 provides a more detailed explaination.) By considering only first-order edge diffraction, their results show good agreement with experimental measurements (in the region where GTD is valid).

The only drawback to the GTD solution for a cone frustum is that the edge diffraction coefficients lack important information about the surface curvature and about the presence of "rim caustics". The information dealing with the surface is necessary to obtain the proper reflected field. The "rim caustics" are places where the diffracted field contributions come from the entire rim rather than local scattering centers. And to get the correct edge diffracted field, the behavior near rim caustics must be known.

Due to this missing information, the original GTD solution fails in the rim-

caustic regions and in the region associated with specular reflection (a reflection caustic region) from the curved surface. Bectel and Ross had avoided these regions by switching to the physical optics solution for both the specular region of the curved surface and in the rim caustic regions associated with specular scattering off the endcaps. Ryan and Peters had also used physical optics for the specular region of the curved surface, but for the rim-caustic regions the scattered fields were evaluated by a technique called the "equivalent current concept". This worked fairly well, however, it would be more convienient if we could somehow preserve the GTD edge-diffraction form of the solution in all regions—without having to switch from one form to another. More recently, Chu [8], based on similar work by Ryan [9], has modified the "caustic distance" in the GTD solution to provide the physical optics result in the specular direction for the curved side of the frustum. While sufficient for cone frustums with small cone angles, it does not provide a uniform solution. A uniform solution is one that provides the correct result uniformly (from the regions where the GTD edge diffraction solution is valid) through the regions of failure.

In this work, we will try to retain the GTD form of the solution, and yet have a uniform solution. In our approach, we will develop "transition functions" that multiply terms in the GTD diffraction coefficients (thereby, generating a modified UTD diffraction coefficient). These transition functions will come into effect at the caustic regions to correct the edge-diffraction solution; outside the caustic regions they will have no effect. This approach has certain advantages in a computer code. The transition functions will eliminate the need to decide when to switch from one solution to another. The simplicity of the GTD edge diffraction solution is preserved with only a slight modification to the diffraction coefficients.

In the following chapters we will show how the transition functions can be

obtained. We will show that by using "equivalent line currents" on the curved surface of the cone frustum, a transition function to correct the failure in the specular region (of the curved surface) can be developed. In a similar way, the use of equivalent edge currents on the rim will lead to transition functions to correct the failure in the rim caustic regions.

For the cylinder, Chiang [1] had obtained a uniform solution through the rim caustic regions. Even though there are some differences for the cone frustum, her work will be applied (in addition to the rim caustic correction of Ryan and Peters).

Basically, the approach used in obtaining our solution is as follows:

1. The theory is developed.

2. Using the theory, calculated results are generated for sample cases.

3. The calculated results are compared with measurements or other known solutions.

4. If the match is good enough then this will be considered the approximate solution. Otherwise, the theory will be refined, and the procedure repeated.

This approach is illustrated as a block diagram in Figure 2. It outlines the contents of this report. Information about each block in the figure will be provided in the following chapters. Chapter 3 discusses the diffraction-point method solution, which provides the basic form of the solution. Chapters 4 and 5 deal with the corrections to the diffraction-point method solution and the development of the transition functions. A comparison with experimental measurements is made in Chapter 6, and with the moment method solution in Chapter 7.

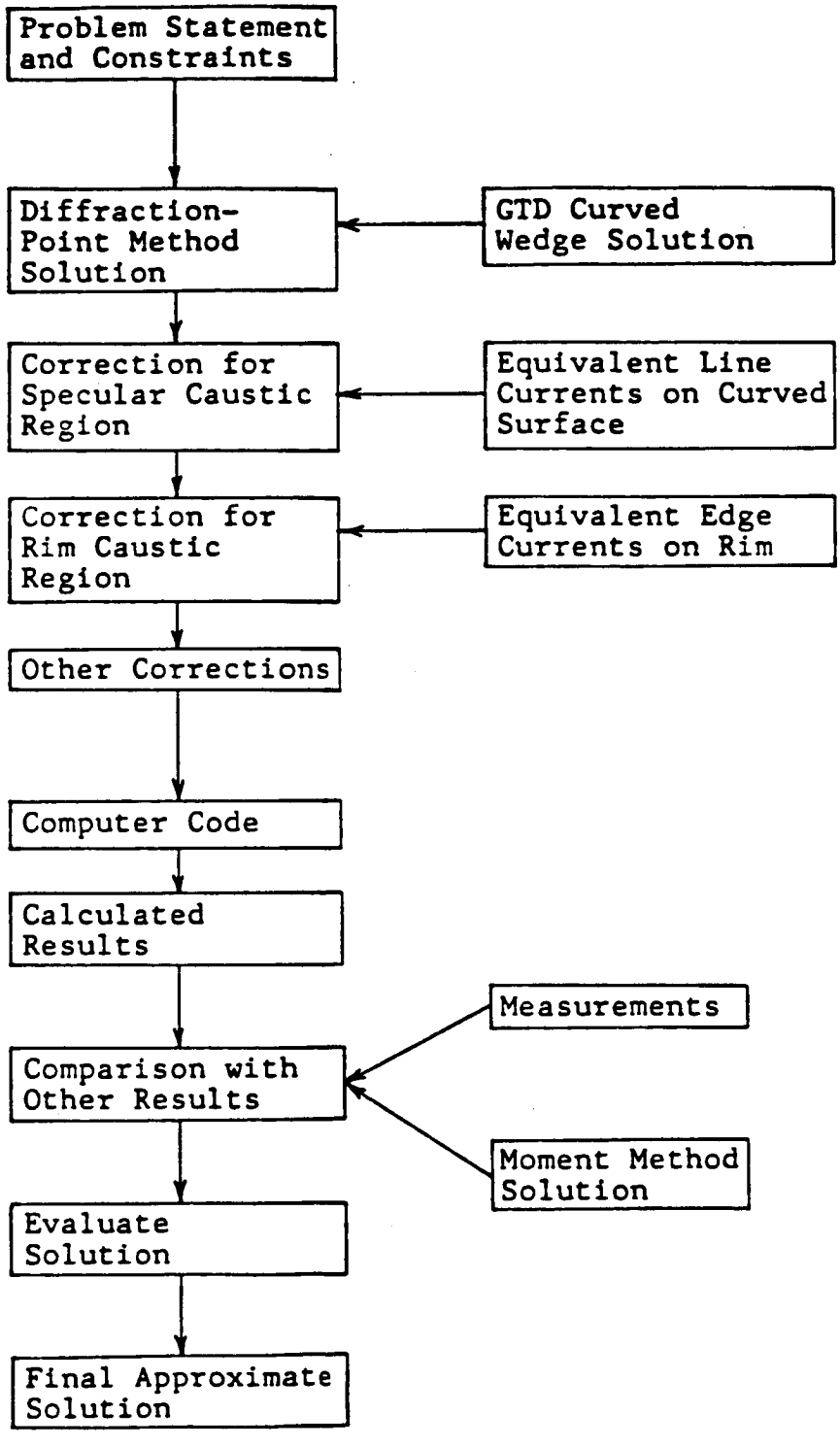

Figure 2: A solution strategy for the cone frustum scattering problem using UTD.

1.4 Notation, Abbreviations, and Symbols

This section contains some information on the notation, abbreviations, and symbols which may be encountered in this report. It is provided as a help to the reader.

1.4.1 Notation

In this work, the $e^{j\omega t}$ time variation will be assumed, and it will be suppressed. Numbers in parentheses ( ) refer to equations. Numbers in brackets [ ] refer to references.

For quantities superscripted with a $\pm$ or $\mp$, the top (bottom) sign corresponds to the top (bottom) sign of similarly subscripted quantities in the expression. For expressions containing quantities with subscripts like, $R_{s,h}$, the first (second) subscript corresponds to the first (second) subscripts of other quantities in the expression. Also for expressions like: $R_{s,h} = \mp 1$, the first (second) subscript corresponds to the top (bottom) sign. A quantity with a named point in parentheses, such as $\rho(Q)$, means that it refers to the parameters at the point Q, or is a function of the parameters at that point.

For most cases, however, (standard) notation usually found in the literature is used. Vectors are indicated by an arrow $\vec{A}$, and unit vectors are indicated by a hat $\hat{a}$. A dyadic quantity is indicated by a double overline $\overline{\overline{A}}$. Coordinates and vectors with a $'$ (prime) usually refer to the source, and unprimed coordinates will usually refer to the receiver or observer.

1.4.2 Symbols

These are just a few of the symbols used. Most of them are defined more specifically in the text.

α_c = cone (half) angle

β_0 = angle of diffraction

β_s = bistatic angle

β = angle from cone surface

γ_e = $kz_e\hat{z}\cdot(\hat{r}+\hat{r}')$

ϵ = permitivity, or a small angle

ε_c = b/a = ellipticity

η = $\sqrt{\mu/\epsilon}$ = impedance of material

θ = theta coordinate, or azimuth angle

λ = wavelength

μ = permiability

π = 3.1415...

ρ^d = caustic distance for the diffracted ray

ρ^r = caustic distance for the reflected ray

σ = radar cross section

τ = distance along cone surface

$\hat{\tau}$ = tangent vector

Φ = angle from wedge face

ϕ_e = ϕ for point on edge

ϕ_s = ϕ for shadow on rim

ψ = angle from wedge face

ψ_e = $ka_e\hat{n}_e\cdot(\hat{r}+\hat{r}')$

ω = angular frequency

$a_{1,2}$ = circular cone fustrum radii

a_e = radius of edge curvature

a = radius,semiminor axis

A_{ave} = average spread factor

b = semimajor axis

$\hat{b}$ = binormal vector

c = speed of light

C_A, C_B, C_C = partial half-rim corrections

$D_{s,h}$ = soft, hard diffraction coefficients

$\overline{\overline{D}}$ = the dyadic edge diffraction coefficient

$\hat{e}$ = edge vector

$\hat{e}_\perp$ = perpendicular direction to plane of incidence

$\hat{e}_\parallel$ = parallel direction to plane of incidence

$\vec{E}^d, \vec{H}^d$ = diffracted field

$\vec{E}^i, \vec{H}^i$ = incident field

$\vec{E}^r, \vec{H}^r$ = reflected field, radiated field

$\vec{E}^e, \vec{H}^e, \vec{E}_e, \vec{H}_e$ = field radiated by electric currents

$\vec{E}^m, \vec{H}^m, \vec{E}_m, \vec{H}_m$ = field radiated by magnetic currents

$f_{0,1,2}$ = equivalent-current half-rim integrals

$f_{c0,c1,c2}$ = equivalent-current corrected half-rim integrals

F = transition function

$F_{0,1,2}$ = equivalent-current rim integrals

h = cone frustum height

$\mathbf{H}_0$ = zero order Struve function

$\mathbf{H}_1$ = first order Struve function

$I^{e,m}$ = electric, magnetic currents

$I_{1,2}$ = equivalent line current integral

j = $\sqrt{-1}$

J_0 = zero order Bessel function

J_1 = first order Bessel function

k = $2\pi/\lambda$

l = length

$\mathbf{M}$ = confluent hypergeometric function

n = wedge angle parameter

$\hat{n}$ = normal vector

$\hat{n}_c$ = normal to cone surface

$\hat{n}_o$ = normal to o-face, endcap

$\hat{n}_e$ = normal edge curvature

$Q_{1,2,3,4}$ = diffraction points

Q_e = point on edge, diffraction point

Q_r = reflection point

r = distance from coordinate origin

$\vec{r}_{1,2,3,4}$ = vector from origin to $Q_{1,2,3,4}$

$\vec{r}_e$ = vector from origin to edge

$\vec{r}_s$ = vector from origin to surface

$\vec{r}_c$ = vector from origin to cone surface

$R_{1,2}$ = principal radii of surface curvature

$R^c_{1,2}$ = principal radii of cone surface curvature

$R_{s,h}$ = reflection coefficient, soft and hard case

$\overline{\overline{R}}$ = dyadic reflection coefficient

s = distance from diffraction point to receiver

$\hat{s}^i$ = incident ray direction

$\hat{s}^r$ = reflected ray direction

$\mathbf{T}$ = transition function curved-side specular region

$\mathbf{T}_{e,e1,e2}$ = transition function rim-caustic region

u = u coordinate in elliptical cylindrical system

U = rim-caustic transition function argument

$\mathbf{U}$ = confluent hypergeometric function

v = v coordinate in elliptical cylindrical system

X = curved-side specular transition function argument

z = z coordinate, or a complex number

1.4.3 Abbreviations

GO = Geometrical Optics

GTD = Geometrical Theory of Diffraction

MM = Moment Method

PO = Physical Optics

PTD = Physical Theory of Diffraction

RB = Reflection Boundary

RCS = Radar Cross Section

SB = Shadow Boundary

UTD = Uniform Geometrical Theory of Diffraction

CHAPTER II

Theoretical Background

2.1 Introduction.

This chapter contains a brief description of the techniques of Geometrical Optics (GO), Physical Optics (PO), and the Uniform Geometrical Theory of Diffraction (UTD). It outlines (without proof) some of the key equations and concepts which provide the foundations for this work. More information on these high-frequency approximate-solution methods can be found in references [2,3,10,11].

In this report, emphasis is placed on the canonical problem of diffraction from a curved wedge. For the cone frustum, edge diffraction is a dominant scattering mechanism. The canonical problem is important because solutions to more complex problems can be constructed by the principle of superposition. This will be demonstrated in Chapter 3 when the diffraction-point method is discussed.

2.2 Geometrical Optics (GO)

The technique of geometrical optics provides a high-frequency approximate solution to the incident, reflected, and refracted fields. In our problem, we will be only concerned with the reflected field. GO can be obtained from an asymptotic solution of Maxwell's equations, and it corresponds to the leading term of the Luneberg-Kline asymptotic expansion for large values of angular frequency [3].

According to geometrical optics, electromagnetic waves can be seen as trav-

eling along certain lines called rays. The ray path is determined by Fermat's principle. It states that the ray path taken by the light from one point to another is an extremum. This is usually a minimum, or the path that requires the least amount of time, but not always. From Fermat's principle, the law of reflection and the law of refraction can be obtained. Later we shall see that it can also be extended to include the law of edge diffraction.

In geometrical optics, phase is proportional to the distance along the ray path from some reference point, and the amplitude is governed by the conservation of power in a tube of rays. Figure 3 shows one such tube of rays. The distances ρ_1 and ρ_2 are from a fixed reference point to the "caustics", or places where rays converge.

In geometrical optics, however, the fields can not directly be evaluated at the caustics. At caustics, the approximation of power conservation in a tube of rays is no longer valid. The field near a caustic appears to become infinite as a finite amount of power gets squeezed into a vanishing area. The fields near caustics must be found by other means.

2.2.1 GO Reflected Field

The GO expression for the reflected field [11] from a smooth conducting convex surface with radius of curvature greater than λ is (see Figure 4),

$$\vec{E}^r(\vec{r}) = \vec{E}^i(Q_r) \cdot \overline{\overline{R}} \sqrt{\frac{\rho_1^r \rho_2^r}{(\rho_1^r + s^r)(\rho_2^r + s^r)}} e^{-jks^r} \tag{2.1}$$

where

$$\begin{aligned} Q_r &= \text{reflection point} \\ \vec{E}^i(Q_r) &= \text{incident field at } Q_r \\ s^r &= \text{distance from } Q_r \text{ to receiver} \end{aligned}$$

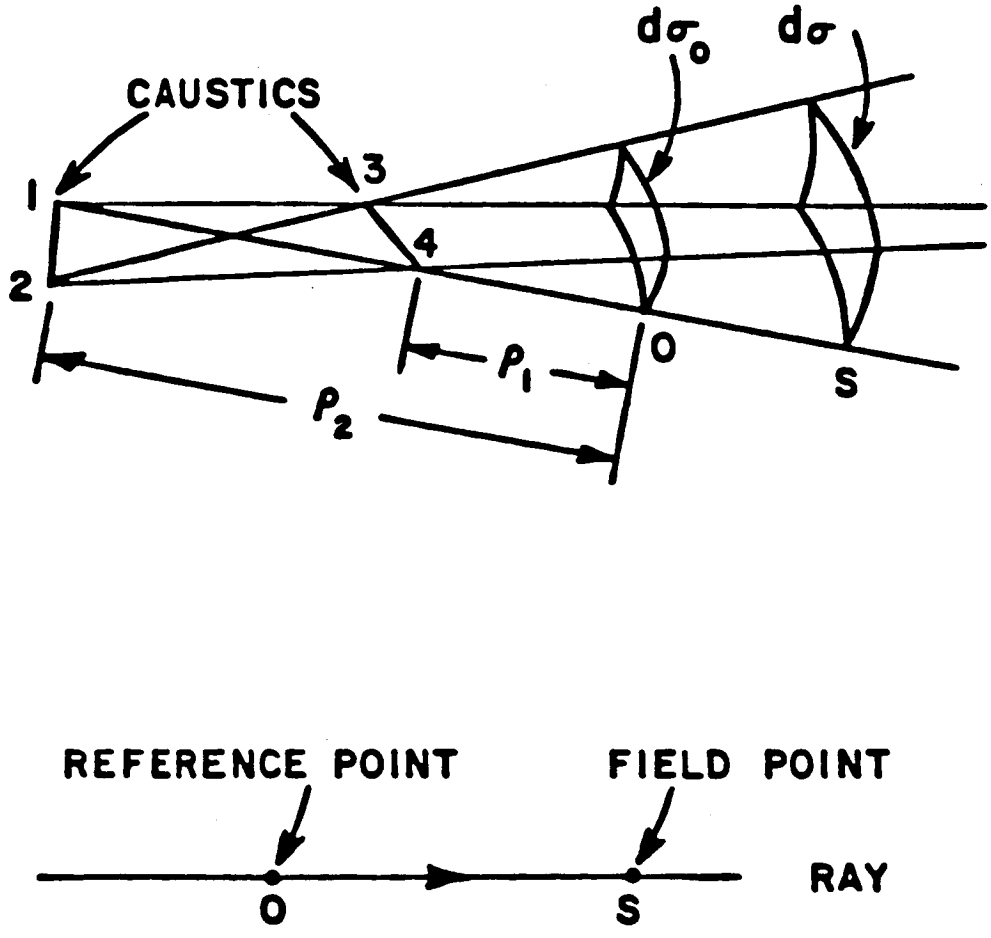

Figure 3: An astigmatic tube of rays

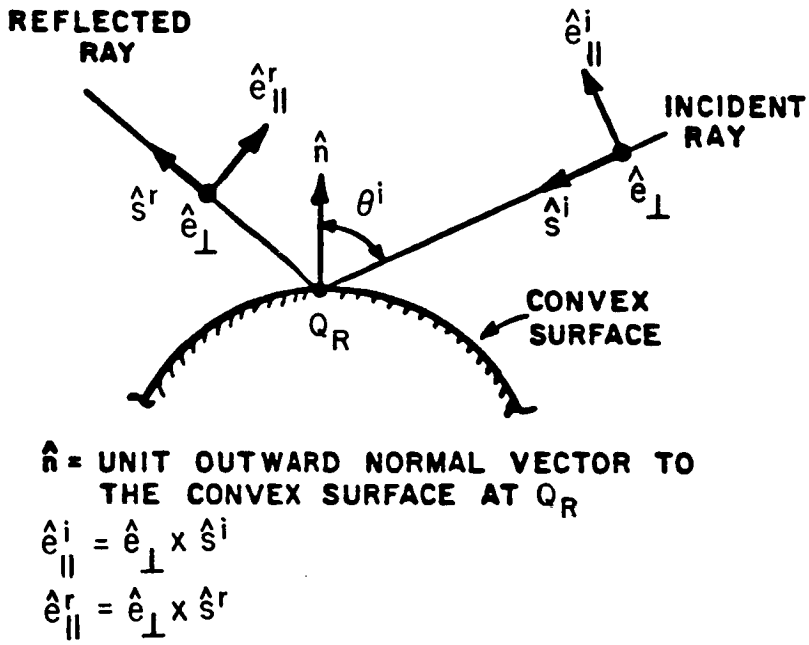

Figure 4: Reflection off a convex conducting surface.

$$\overline{\overline{R}} = \text{the dyadic reflection coefficient}$$

$$\overline{\overline{R}} = R_s \hat{e}^i_\perp \hat{e}^r_\perp + R_h \hat{e}^i_\parallel \hat{e}^r_\parallel \tag{2.2}$$

$$R_{s,h} = \mp 1 \tag{2.3}$$

$$\rho^r_{1,2} = \text{caustic distances for the reflected rays}$$

$$\begin{aligned}\frac{1}{\rho^r_{1,2}} = \frac{1}{\rho^i_m} + \frac{f}{\rho_g(Q_r)\cos\theta^i}\Bigg(1 \pm \Bigg[&\frac{\rho_g^2(Q_r)\cos^2\theta^i}{4f^2} \\ &\cdot\left(\frac{1}{\rho^i_1} - \frac{1}{\rho^i_2}\right)^2 + \frac{\rho_g^2(Q_r)\cos\theta^i}{f^2}\left(\frac{1}{\rho^i_1} - \frac{1}{\rho^i_2}\right) \\ &\cdot\left\{\frac{g\cos 2\alpha_o}{\rho_g(Q_r)} - \sin 2\alpha_o \sin 2\omega_o \cos\theta^i \left(\frac{1}{R_1} - \frac{1}{R_2}\right)\right\} \\ &+1 - \frac{4\rho_g^2(Q_r)\cos^2\theta^i}{f^2 R_1 R_2}\Bigg]^{\frac{1}{2}}\Bigg)\end{aligned} \tag{2.4}$$

where

$$\theta^i = \text{angle of incidence} = \cos^{-1}(-\hat{s}^i \cdot \hat{n})$$

$$R_{1,2} = \text{principal radii of surface curvature at } Q_r$$

$$f = 1 + \frac{\rho_g(Q_r)}{\rho_t(Q_r)}\cos^2\theta^i$$

$$g = 1 - \frac{\rho_g(Q_r)}{\rho_t(Q_r)}\cos^2\theta^i .$$

Note that ρ_g is the radius of surface curvature at Q_r in the plane of incidence. The plane of incidence contains $\hat{s}^i$, $\hat{n}$, and $\hat{t}$. Further, ρ_t is the radius of surface curvature at Q_r in the plane containing $\hat{n}$ and $\hat{b}$ where,

$$\hat{n} = \text{normal to the surface at } Q_r$$

$$\hat{t} = \text{tangent to the surface at } Q_r$$

$$\hat{b} = \hat{t} \times \hat{n}$$

$\hat{s}^i$ = direction of the incident ray

$\hat{s}^r$ = direction of the reflected ray

$\hat{r}'$ = direction of the source from Q_r

$\hat{r}$ = direction of the receiver from Q_r .

The direction of the reflected ray is defined by the law of reflection which is given by

$$\hat{n} \cdot \hat{s}^r = -\hat{n} \cdot \hat{s}^i \tag{2.5}$$

The point of reflection, Q_r, is a point on the surface such that the law of reflection is satisfied. At Q_r, one finds that

$$\hat{n} \cdot \hat{r} = \hat{n} \cdot \hat{r}' . \tag{2.6}$$

2.3 Physical Optics (PO)

If the true currents on a scatterer were known, then we would be able to find the true scattered field. However, these currents are unknown. The technique of physical optics approximates the currents by using the geometrical optics currents. For an electrically large conducting scatterer, the surface currents are approximately

$$\vec{J} \approx \vec{J_{GO}} = \begin{cases} 2\hat{n} \times \vec{H}^i & \text{on the lit surface, and} \\ 0 & \text{on the shadowed surface.} \end{cases} \tag{2.7}$$

The PO scattered field is obtained by substituting these approximate currents into the radiation integral.

In this work, PO is used only in an indirect manner. We will use the knowledge that PO is known to give good results in the direction of specular scattering. References [1,10] provide some discussion on this subject.

2.4 Uniform Geometrical Theory of Diffraction (UTD)

Classical geometrical optics considers scattering due to reflection, but not diffraction. Keller [2] extended GO to include diffraction into the approach known as the geometrical theory of diffraction (GTD). With the knowledge that wave propagation is a local phenomena at high frequencies, it was reasoned that the diffracted field, like the reflected field, must also propagate along rays. GTD assumes that diffracted rays are produced when incident rays encounter surface discontinuites (edges, tips, vertices) or when they graze the surface of a scatterer. It is found that various laws of diffraction can result by using these assumptions in a generalized form of Fermat's principle. Experimental results confirm that these assumptions are valid for electrically large scatterers.

In GTD, the initial value of the diffracted rays are obtained by multiplying the incident field with a diffraction coefficient at the point of diffraction, analogous to the reflection coefficient for a reflected ray. The expression for the diffraction coefficient depends on the scattering mechanism (edge diffraction, tip diffraction, etc.). The development of new valid diffraction coefficients is presently a major area of investigation. The application of GTD is limited only by the availability of accurate coefficients. The uniform geometrical theory of diffraction (UTD) is an improved version of GTD that uses diffraction coefficients which remain valid near the shadow boundaries—where Keller's original coefficients had failed.

Two major contributors to the diffracted field considered by UTD are diffraction from edges and diffraction from curved surfaces (or creeping wave diffraction). In this report, only edge diffraction will be considered.

2.4.1 UTD Edge Diffracted Field

The diffracted field from a semi-infinite perfectly-conducting curved wedge is given by the following expression:

$$\vec{E}^d(s) = \vec{E}^i(Q_e) \cdot \overline{\overline{D}} \sqrt{\frac{\rho^d}{s(\rho^d + s)}} e^{-jks} \tag{2.8}$$

where

$$\begin{aligned} Q_e &= \text{point of diffraction on edge} \\ \vec{E}^i(Q_e) &= \text{incident field at } Q_e \\ s &= \text{distance from } Q_e \text{ to receiver} \\ \rho^d &= \text{caustic distance for the diffracted ray} \\ \overline{\overline{D}} &= \text{the dyadic edge diffraction coefficient .} \end{aligned}$$

The dyadic edge diffraction coefficient is given by

$$\overline{\overline{D}} = -\hat{\beta}_0' \hat{\beta}_0 D_s - \hat{\Phi}' \hat{\Phi} D_h \,. \tag{2.9}$$

The following is the form of the diffraction coefficient which was developed by Kouyoumjian and Pathak [3]. The coefficients of a perfectly-conducting curved wedge are

$$D_{s,h} = \frac{-e^{-j\frac{\pi}{4}}}{2n\sqrt{2\pi k}\sin\beta_0} \cdot \left\{ D^{in} + D^{io} \mp (D^{rn} + D^{ro}) \right\} \tag{2.10}$$

where

$$D^{in} = \cot\left(\frac{\pi + (\Phi - \Phi')}{2n}\right) F(kL^{in} a^+(\Phi - \Phi')) \tag{2.11}$$

$$D^{io} = \cot\left(\frac{\pi - (\Phi - \Phi')}{2n}\right) F(kL^{io} a^-(\Phi - \Phi')) \tag{2.12}$$

$$D^{rn} = \cot\left(\frac{\pi + (\Phi + \Phi')}{2n}\right) F(kL^{rn} a^+(\Phi + \Phi')) \tag{2.13}$$

$$D^{ro} = \cot\left(\frac{\pi - (\Phi + \Phi')}{2n}\right) F(kL^{ro} a^-(\Phi + \Phi')) \,. \tag{2.14}$$

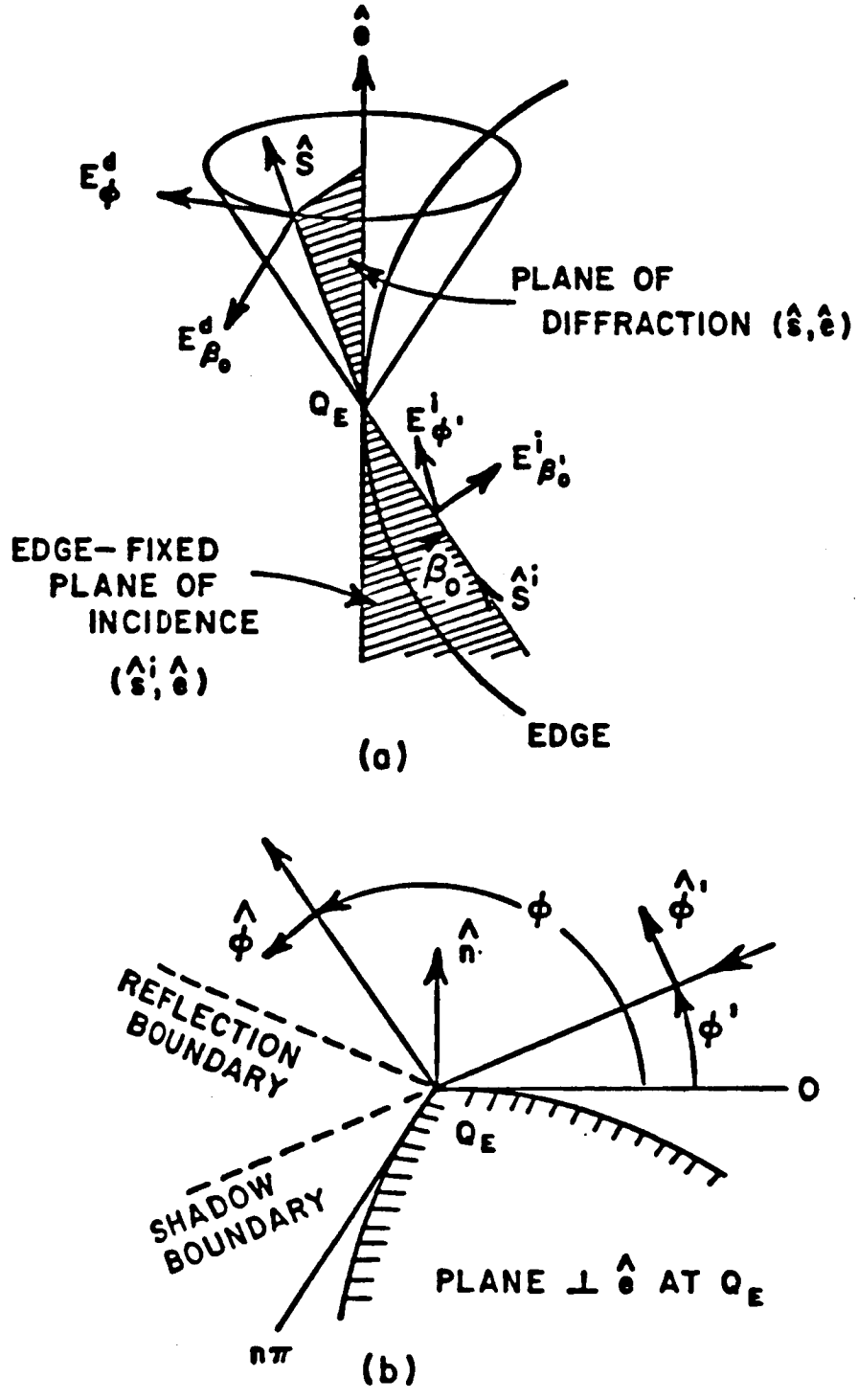

Figure 5: Edge geometry.

The angles β_0, Φ, and Φ' are shown in Figure 5, and n is a wedge angle parameter, where the wedge angle is $(2-n)\pi$. The cotangent terms in the diffraction coefficient become singular at various reflection and shadow boundaries of the surfaces. Table 2.1 and Figure 6 show where each cotangent term becomes singular. The function F is a transition function which is defined by

$$F(x) = 2j\sqrt{x}e^{jx}\int_{\sqrt{x}}^{\infty} e^{-j\tau^2}\,d\tau\,. \tag{2.15}$$

Figure 7 shows the magnitude and phase of this function. L is a distance parameter, where

$$L^{i,r} = s\frac{(\rho_e^{i,r}+s)\rho_1^{i,r}\rho_2^{i,r}}{\rho_e^{i,r}(\rho_1^{i,r}+s)(\rho_2^{i,r}+s)}\sin^2\beta_0\,. \tag{2.16}$$

The parameters $\rho_e^{i,r}$ are the (incident,reflected) radii of curvature in the plane containing the (incident,reflected) ray and $\hat{e}$; and $\rho_{1,2}^{i,r}$ are the principal radii of curvature of the (incident,reflected) wavefront at Q_e. The superscripts n,o on L denote that the radii of curvature are determined at the respective reflection boundaries $(2n-1)\pi-\Phi'$ and $\pi-\Phi'$. The reflected field caustic distance in the plane of the reflected ray and edge tangent is given by

$$\frac{1}{\rho_e^r} = \frac{1}{\rho_e^i} - \frac{2(\hat{n}\cdot\hat{n}_e)(\hat{s}^i\cdot\hat{n})}{a_e\sin^2\beta_0} \tag{2.17}$$

where

$\hat{n}$ = normal to the surface atQ_e

$\hat{n}_e$ = normal to edge curvature atQ_e

$\hat{s}^i$ = incident ray direction

a_e = radius of edge curvature

$$a^{\pm}(x) = 2\cos^2\left(\frac{2n\pi N^{\pm}-x}{2}\right)\,. \tag{2.18}$$

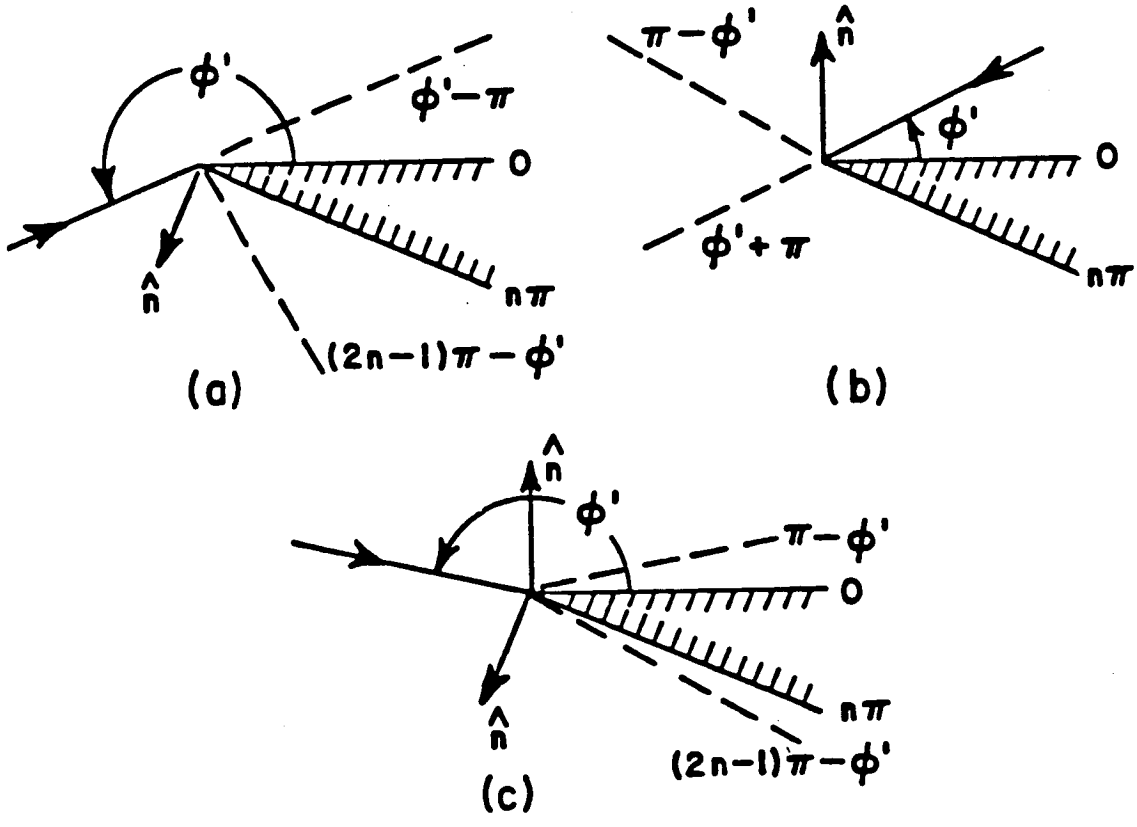

Figure 6: Shadow and reflection boundaries for different angles of incidence.

Table 2.1: Table showing where cotangent terms are singular.

	The cotangent is singular when	value of N at the boundary
$\cot\left(\frac{\pi+(\phi-\phi')}{2n}\right)$	$\phi = \phi' - \pi$, a SB surface $\phi=0$ is shadowed	$N^+ = 0$
$\cot\left(\frac{\pi-(\phi-\phi')}{2n}\right)$	$\phi = \phi' + \pi$, a SB surface $\phi=n\pi$ is shadowed	$N^- = 0$
$\cot\left(\frac{\pi+(\phi+\phi')}{2n}\right)$	$\phi = (2n-1)\pi-\phi'$, a RB reflection from surface $\phi=n\pi$	$N^+ = 1$
$\cot\left(\frac{\pi-(\phi+\phi')}{2n}\right)$	$\phi=\pi - \phi'$, a RB reflection from surface $\phi=0$	$N^- = 0$

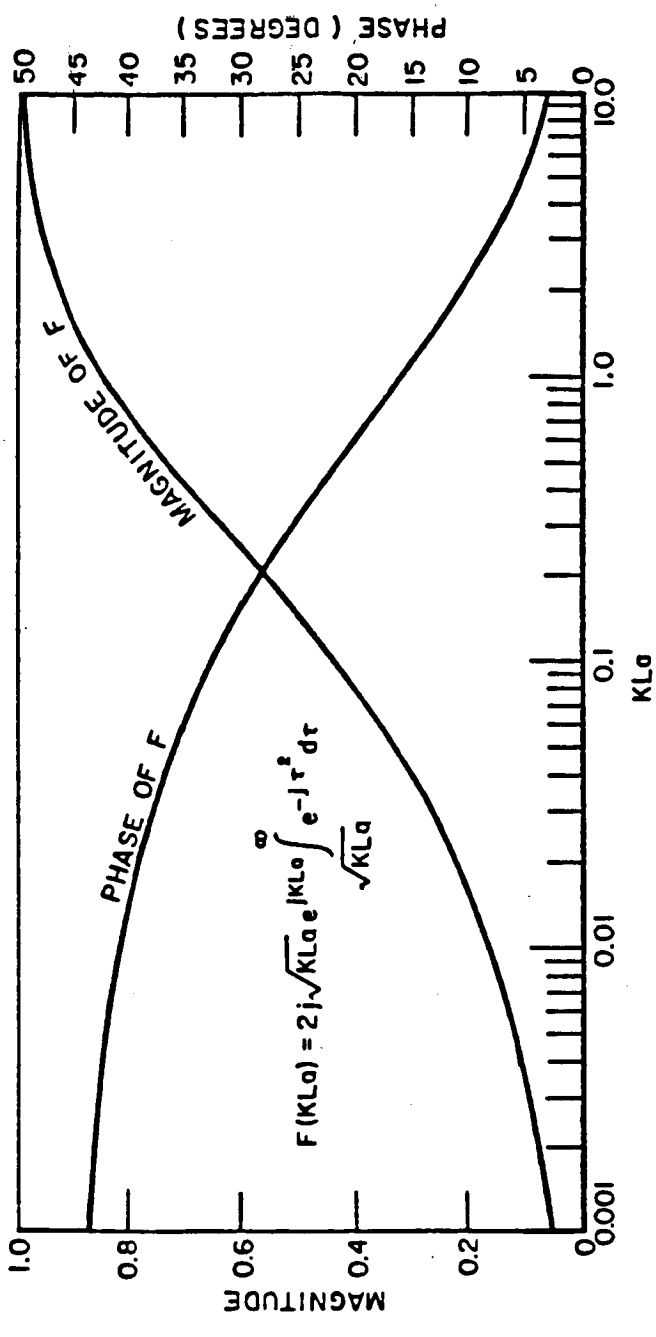

Figure 7: The transition function F.

And $N^{\pm}$ are integers which most nearly satisfy the equation,

$$2\pi\, nN^{\pm} - x = \pm\pi \tag{2.19}$$

where $x = \Phi \pm \Phi'$. See Figure 8.

Law of Edge Diffraction

The direction of the diffracted rays are defined by the law of edge diffraction. This law arises from a generalized statement of Fermat's principle where the diffracted ray path is the minimum distance from source to edge to observation point. The law of edge diffraction is given by

$$\hat{s}^i \cdot \hat{e} = \hat{s} \cdot \hat{e} \tag{2.20}$$

where

$\hat{e}$ = unit edge vector

$\hat{s}^i$ = direction of the incident ray, and

$\hat{s}$ = direction of the diffracted ray.

Note that an incident ray hitting a point on the edge gives rise to a cone of diffracted rays (see Figure 5).

A diffraction point, Q_e, is a point on the edge such that the law of diffraction is satisfied, or

$$-\hat{r}' \cdot \hat{e} = \hat{r} \cdot \hat{e} \tag{2.21}$$

where

$\hat{r}'$ = direction of the source from Q_e

$\hat{r}$ = direction of the receiver from Q_e

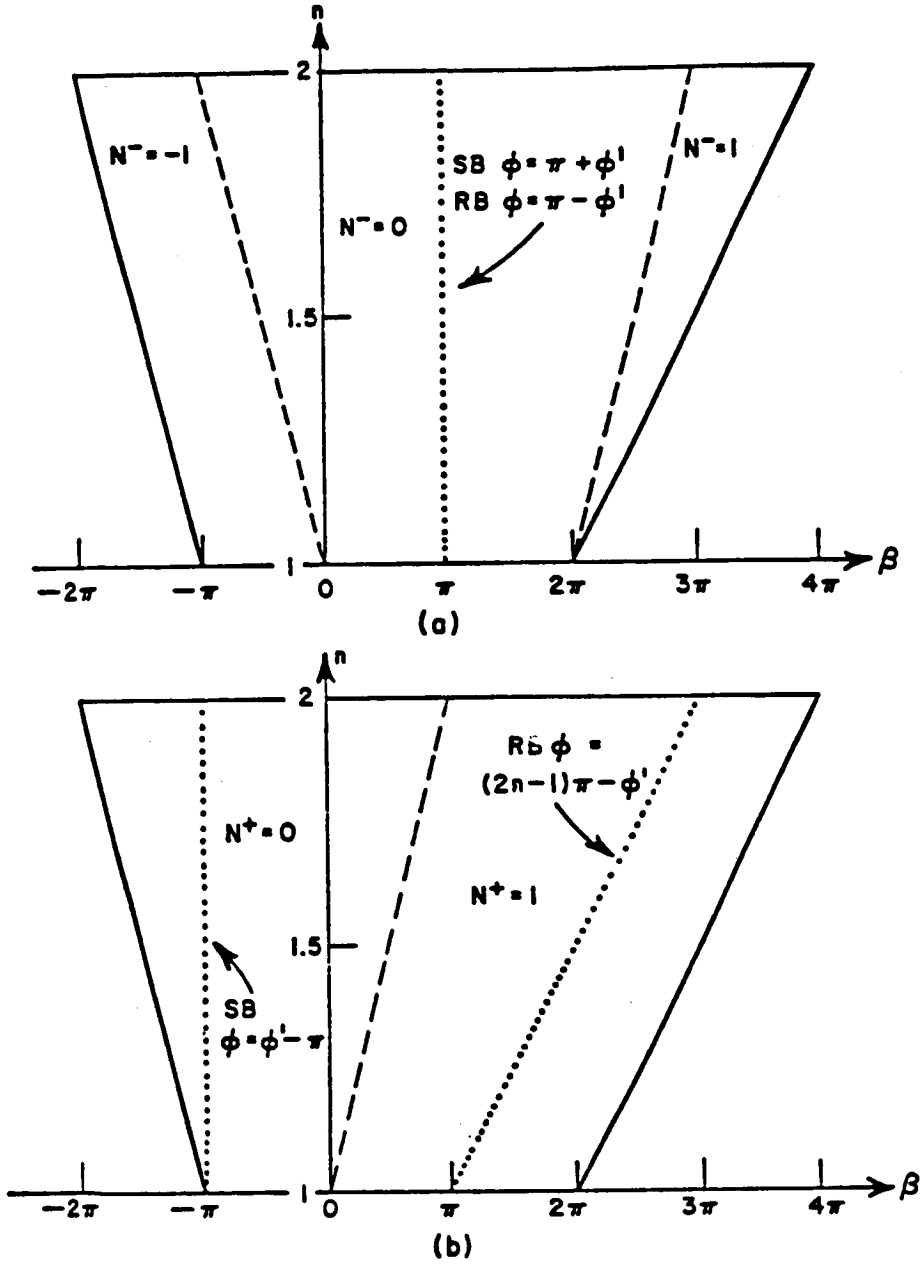

Figure 8: N^+ and N^- as functions of β_0 and n.

Reasons to Use UTD

The following are some of the reasons why we choose UTD for our problem:

1. No exact solution is available for the cone frustum. Exact solutions exist only for the most simple shapes (that fit a general coordinate frame). Therefore, we have to use an approximate-solution technique.

2. UTD is accurate for high frequencies. Our problem deals with frequencies at the high end of the resonance region and into the optical region. High-frequency asymptotic methods, such as UTD, work well at these frequencies. Past experiments have shown good agreement with measurements and other solutions. The moment method can also provide solutions in the resonance region, but computations can become costly with increasing frequency.

3. It complements low-frequency solutions, such as those obtained by the moment method.

4. It can yield bistatic solutions.

5. It is easy to apply. The local nature of high-frequency asymptotic approximations can resolve a complex scatterer into simpler components.

6. It is a ray method. Ray methods can provide physical insight into the scattering mechanisms. Also due to the continuous nature of physical phenomena, the accuracy of a calculated scattering pattern can be readily determined. The inaccuracies caused by missing scattering components appear as discontinuites in the pattern.

In the next chapter we will show how a solution for the cone frustum can be obtained using UTD, and the advantages mentioned above will be demonstrated.

CHAPTER III

The Diffraction-Point Method

3.1 Introduction.

The previous chapter briefly discussed the UTD solution to a curved semi-infinite wedge. This chapter applies those results to obtain an approximate solution to the scattered fields from a cone frustum. The technique used to generate the solution is called the "diffraction-point method".

3.2 How does the diffraction-point method work?

We recall that at high frequencies, wave propagation and scattering have a very local nature. Ray techniques are therefore applicable. According to the geometrical theory of diffraction, diffracted rays occur when incident rays hit geometric discontinuities on a scatterer, such as the edges. For an edge, the direction of these diffracted rays are determined by the law of edge diffraction.

In order to apply the diffraction-point method, one must first be able to isolate the source of these diffracted rays to separate points. The points are sometimes called "scattering centers" or "diffraction points". For the cone frustum, the scattering centers are located on the edges forming the rim. The location and number of points will change depending on the position of source and receiver. Note that for the cone frustum, there can be as many as four diffraction points.

This local character—our ability to isolate points of diffraction, simplifies

the solution to the problem greatly. Since diffraction is a local phenomena, only the local geometry in the neighborhood of the scattering center is important in determining how the incident energy gets scattered. The diffracted field from a scattering center can be approximated with a known solution for a scatterer having the same local geometry. The problem of finding the cone frustum's scattered field is now reduced to the problem of finding the diffraction from curved wedges that match the geometry at the diffraction points.

Therefore, the diffraction-point method involves a superposition of semi-infinite wedge solutions. The total scattered field is approximated by summing the diffracted field contributions from each wedge. This gives a solution that is both fast to compute and aesthetically pleasing due to its simple form and physical insight of the scattering components.

Again, however, it must be emphasized that the method only works well when the local nature of the scattering centers is not violated. The spacing between scattering centers should usually be greater than a wavelength. This is true for most regions of observation, but in some places the diffraction-point method can fail. These difficulties will be discussed later, but happily these problems can be corrected using other techniques.

A short note on the wording: in this report, the "diffraction-point method solution" will be defined as the "first-order edge diffraction solution without corrections". Where "first-order" means that only the primary interaction of the incident ray with the edge is considered.

Another item worth mentioning is that the previous condition about the "wavelength spacing between scattering centers", should only be taken as a rule-of-thumb. The diffraction-point method solution fails gracefully when this condition is violated. The solution may be extended to lower frequncies by including higher

order terms (multiple ray interactions).

3.3 History

The idea of the diffraction-point method is not new. Since exact solutions are often difficult to obtain and apply, GTD techniques are usually the most convienient way to get an approximate high-frequency solution. Some of the people who have used this method in the past for the cone frustum include Bectel and Ross [4,5,6] and Ryan and Peters [7]. The results of their work show good agreement with measurement (in the region where the method is valid). Besides the cone frustum, this method has been successfully applied to other scatterers, including plates and cylinders.

3.4 Application of the Diffraction-Point Method to the Cone Frustum

Now let us proceed with how the diffraction-point method can be applied to the cone frustum. The procedure consists of the following four steps:

1. A coordinate system for the scatterer is assigned.

2. The location of the diffraction points is determined.

3. The diffracted fields are calculated for each edge corresponding to the local conditions at the point of diffraction. This involves finding the incident field at the diffraction point, angles of incidence and observation, and the wedge angle and curvature.

4. The diffracted fields from each diffraction point are summed to obtain the approximate scattered field.

These steps will be shown in greater detail on the following pages. Also given are examples of calculated scattering patterns. To simplify things, the examples are restricted to a circular cone frustum with source and receiver confined to the a plane containing the axis of symmetry. This plane will be called the principal plane. (But there is nothing in the theory that limits us to these specific cases.)

3.4.1 Coordinate System

For this example, the standard spherical polar coordinate system (r,θ,ϕ) is chosen. When determining the fields (incident or diffracted) for each diffraction point, we will need to convert between their own ray-fixed coordinates to this system.

The cone frustum is aligned with its axis along the z-axis and with its center at the origin. Figure 9 shows the setup. Here we will define the principal plane as being the x-z plane. Later, when considering the orthogonal polarizations of incoming and scattered waves, "horizontal" (parallel to the axis) and "vertical" (perpendicular to the axis) will be referred to this plane.

3.4.2 Diffraction Points

The location of the diffraction points on the frustum's rims can be found by applying the law of edge diffraction. The law of edge diffraction states that

$$-\hat{r}' \cdot \hat{e}(\phi_e) = \hat{r} \cdot \hat{e}(\phi_e)$$

or

$$(\hat{r}' + \hat{r}) \cdot \hat{e}(\phi_e) = 0 \tag{3.22}$$

where

$$\hat{r}' = \hat{x}\sin\theta'\cos\phi' + \hat{y}\sin\theta'\sin\phi' + \hat{z}\cos\theta' \tag{3.23}$$

$$\hat{r} = \hat{x}\sin\theta\cos\phi + \hat{y}\sin\theta\sin\phi + \hat{z}\cos\theta \tag{3.24}$$

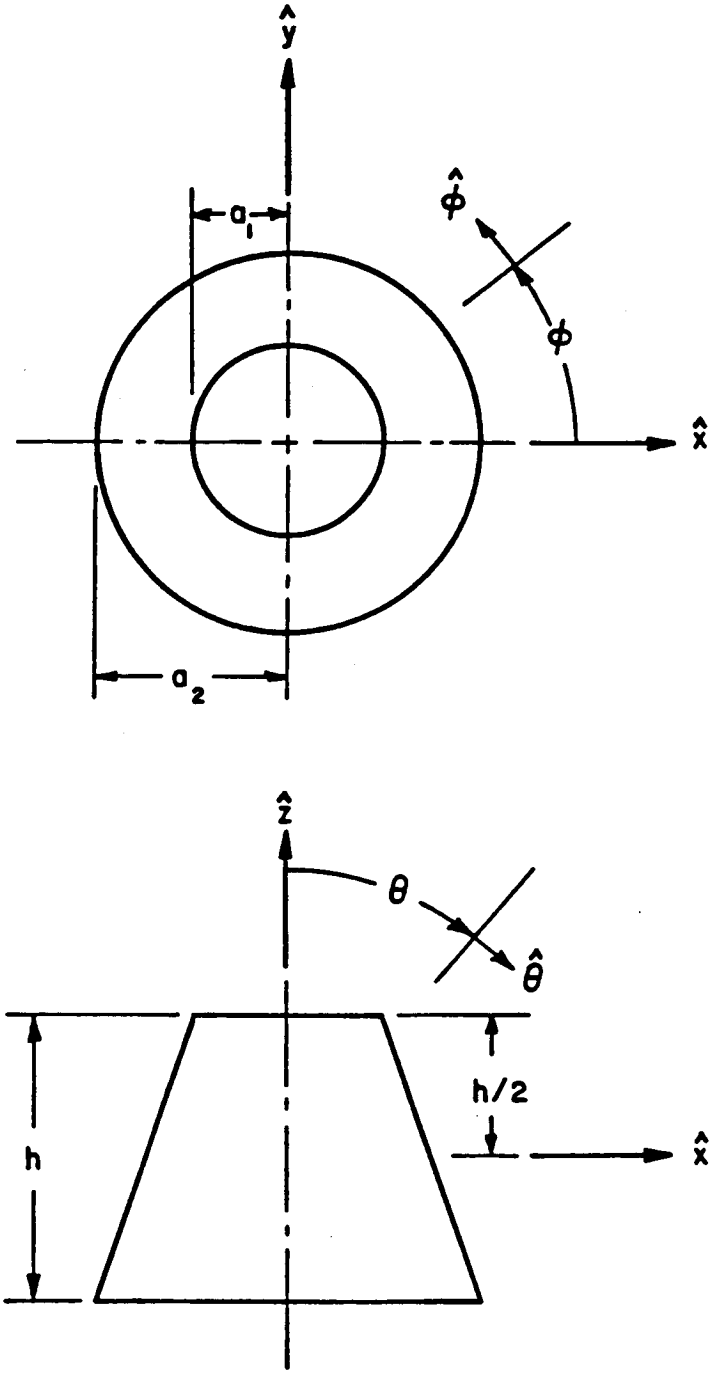

Figure 9: The cone frustum in the (x, y, z) coordinate system.

and for a circular cone frustum,

$$\hat{e}(\phi_e) = -\hat{x}\sin\phi_e + \hat{y}\cos\phi_e \,. \tag{3.25}$$

The source and receiver positions are (θ',ϕ') and (θ,ϕ), respectively. The location of the diffraction point on the edge is ϕ_e. Substituting for $\hat{r}'$, $\hat{r}$, and $\hat{e}$, and solving for ϕ_e yields

$$\phi_e = \tan^{-1}\left[\frac{\pm(\sin\theta'\sin\phi' + \sin\theta\sin\phi)}{\pm(\sin\theta'\cos\phi' + \sin\theta\cos\phi)}\right] . \tag{3.26}$$

We find that there are two possible diffraction points associated with each endcap rim, or a total of four possible diffraction points for the frustum. In the principal plane, the diffraction points are located at $\phi_e = 0$ and $\phi_e = \pi$. These correspond to the points Q_1, Q_2, Q_3, and Q_4 shown in Figure 10.

Note, however, that for certain cases all points on the rim satisfy the law of edge diffraction (such as for $\theta = \theta' = 0$). For these instances, we cannot locate isolated diffraction points, and the diffraction-point method cannot be applied. These are called "rim caustic regions" and other techniques will have to be used to calculate the proper field. More will be said about this later.

3.4.3 Diffracted Fields from an Edge

From Chapter 2, the diffracted field from a curved edge corresponding to a diffraction point Q_e is

$$\vec{E}_e^d = \vec{E}^i(Q_e)\cdot\overline{\overline{D}}(Q_e)\sqrt{\frac{\rho^d}{s(s+\rho^d)}}e^{-jks}$$

where

$$\overline{\overline{D}}(Q_e) = -\hat{\beta}_0{}'\hat{\beta}_0 D_s(Q_e) - \hat{\Phi}'\hat{\Phi}D_h(Q_e) \,.$$

Far Field Approximations

Several approximations can be made for the far field (see Figure 11).

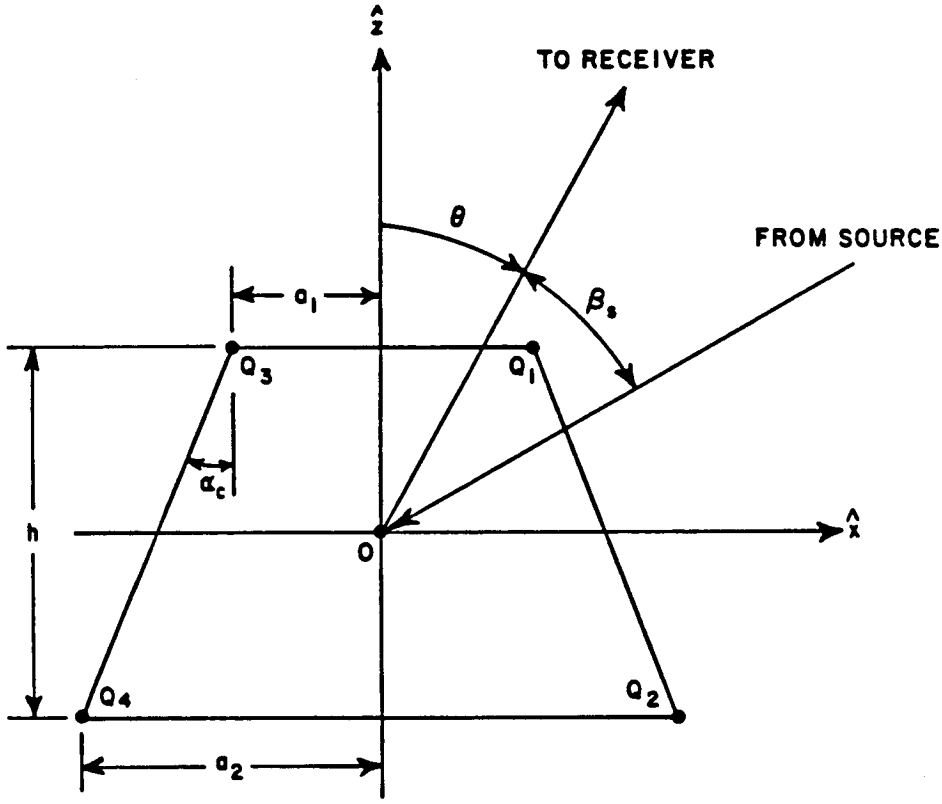

Figure 10: Cone frustum geometry in the principal plane.

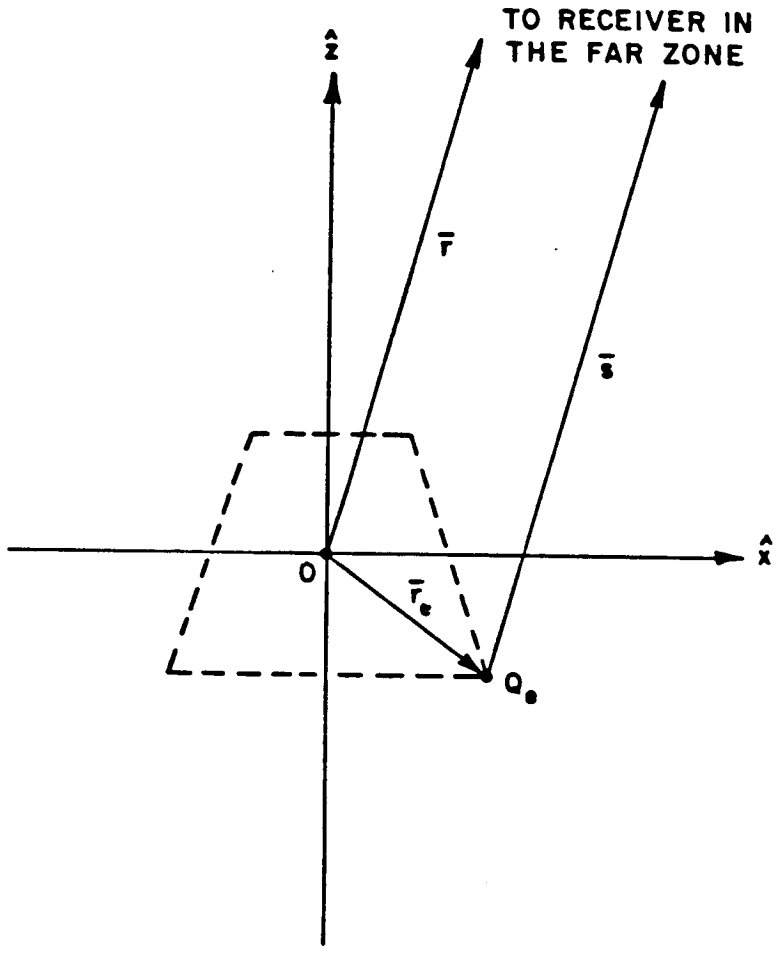

Figure 11: Far-zone approximation for the diffracted field from a point Q_e on the edge.

$$\sqrt{\frac{\rho^d}{s(s+\rho^d)}} \approx \frac{\sqrt{\rho^d}}{r} \tag{3.27}$$

$$e^{-jks} \approx e^{-jkr} e^{jk\vec{r_e}\cdot\hat{r}} \tag{3.28}$$

and since $F(kLa) \approx 1$ as $L \to \infty$,

$$D_{s,h} \approx \frac{-e^{-j\frac{\pi}{4}}}{2n\sqrt{2\pi k}\sin\beta_0} \left\{ \cot\left(\frac{\pi + (\Phi - \Phi')}{2n}\right) + \cot\left(\frac{\pi - (\Phi - \Phi')}{2n}\right) + \right.$$

$$\left. + R_{s,h}\left[\cot\left(\frac{\pi + (\Phi + \Phi')}{2n}\right) + \cot\left(\frac{\pi - (\Phi + \Phi')}{2n}\right)\right]\right\} . \tag{3.29}$$

The far field expression becomes

$$\vec{E}_e^d \approx \vec{E}^i(Q_e) \cdot [-\hat{\beta_0}'\hat{\beta}_0 D_s(Q_e) - \hat{\Phi}'\hat{\Phi} D_h(Q_e)] \sqrt{\rho^d(Q_e)} e^{jk\vec{r_e}\cdot\hat{r}} \frac{e^{-jkr}}{r} . \tag{3.30}$$

Incident Field

Since we assume plane wave illumination, the magnitude of the incident field is the same at each edge. However, we still must consider the phase and the shadowing of the diffraction points by the structure. The incident field is given by

$$\vec{E}^i(Q_e) = \vec{E_0}^i(Q_e) e^{jk\vec{r_e}\cdot\hat{r}'} e^{-jkr'} \tag{3.31}$$

where

$$\vec{E_0}^i(Q_e) = \begin{cases} E^i_{\beta_0}\hat{\beta_0}' + E^i_{\Phi}\hat{\Phi}' & \text{if point is illuminated, and} \\ 0 & \text{if in shadow.} \end{cases} \tag{3.32}$$

Depending on the position of the source, different diffraction points are shadowed. In the principal plane, six different regions must be considered. This is shown in Figure 12.

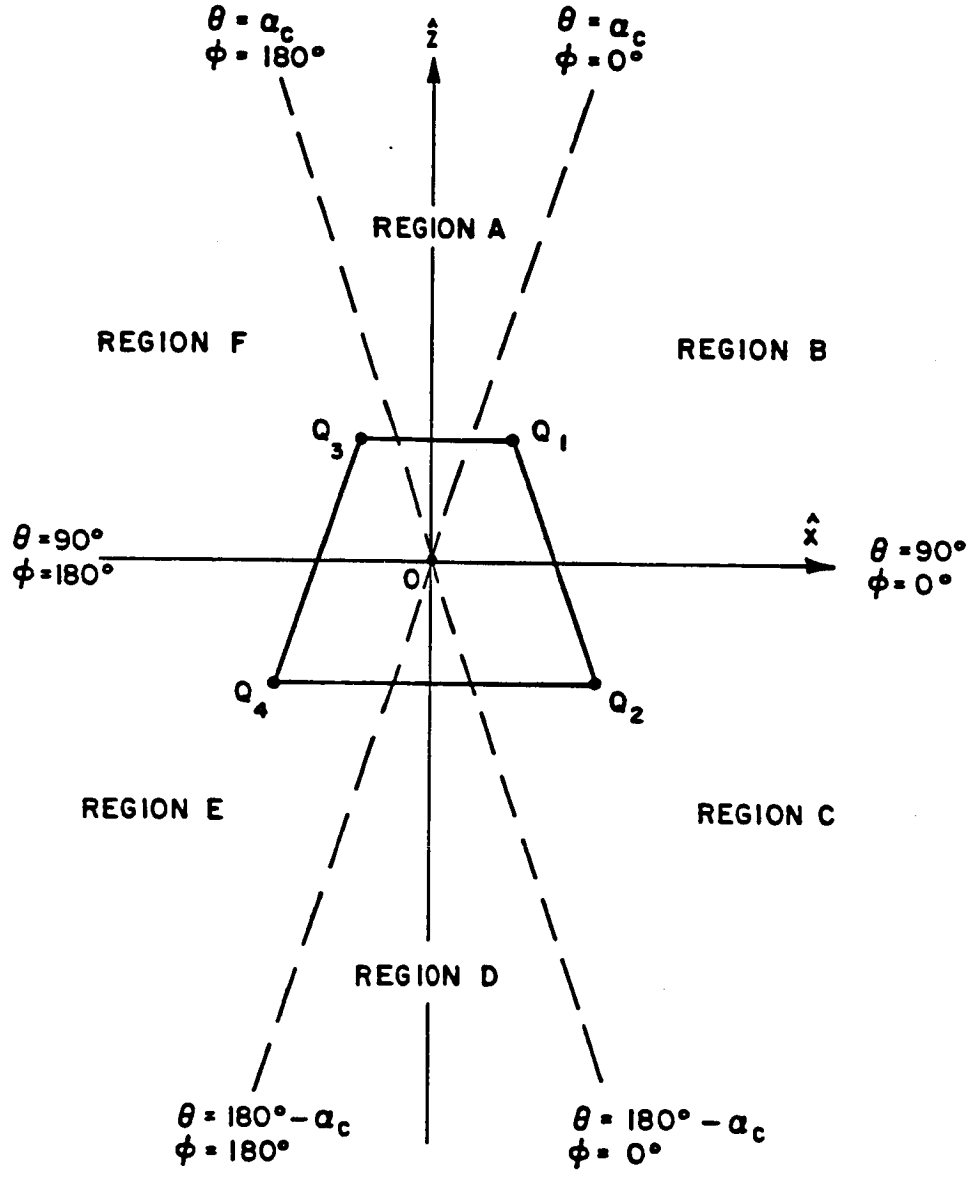

Figure 12: Regions where different diffraction points are considered.

Geometry at Diffraction Points

The diffraction points for source and receiver in the principal plane are located at Q_1, Q_2, Q_3, and Q_4 as shown in Figure 10. The values of ρ^d, β_0, Φ, Φ', and n depend on which diffraction point is considered. The angles Φ and Φ' are measured from the o-face. For this problem we define the flat face (endcap) as the o-face. See Figure 13.

For the principal plane,

$$\rho^d = \frac{a_e \sin^2 \beta_0}{\hat{n}_e \cdot (\hat{r} + \hat{r}')}$$

$$a_e = \begin{cases} a_1 & \text{for } Q_1, Q_3 \\ a_2 & \text{for } Q_2, Q_4 \end{cases} \tag{3.33}$$

$$\hat{n}_e = \begin{cases} \hat{x} & \text{for } Q_1, Q_2 \\ -\hat{x} & \text{for } Q_3, Q_4 \end{cases} \tag{3.34}$$

$$\beta_0 = \frac{\pi}{2} \text{ for } Q_1, Q_2, Q_3, \text{ and } Q_4 . \tag{3.35}$$

The value of the wedge angle parameter, n, can be related to the cone angle α_c. For a circular cone frustum,

$$n = \begin{cases} \frac{3}{2} - \frac{\alpha_c}{\pi} & \text{for } Q_1, Q_3 \\ \frac{3}{2} + \frac{\alpha_c}{\pi} & \text{for } Q_2, Q_4 \end{cases} \tag{3.36}$$

where the cone angle is defined as

$$\alpha_c = \tan^{-1}\left(\frac{a_2 - a_1}{h}\right) \tag{3.37}$$

for $a_2 > a_1$.

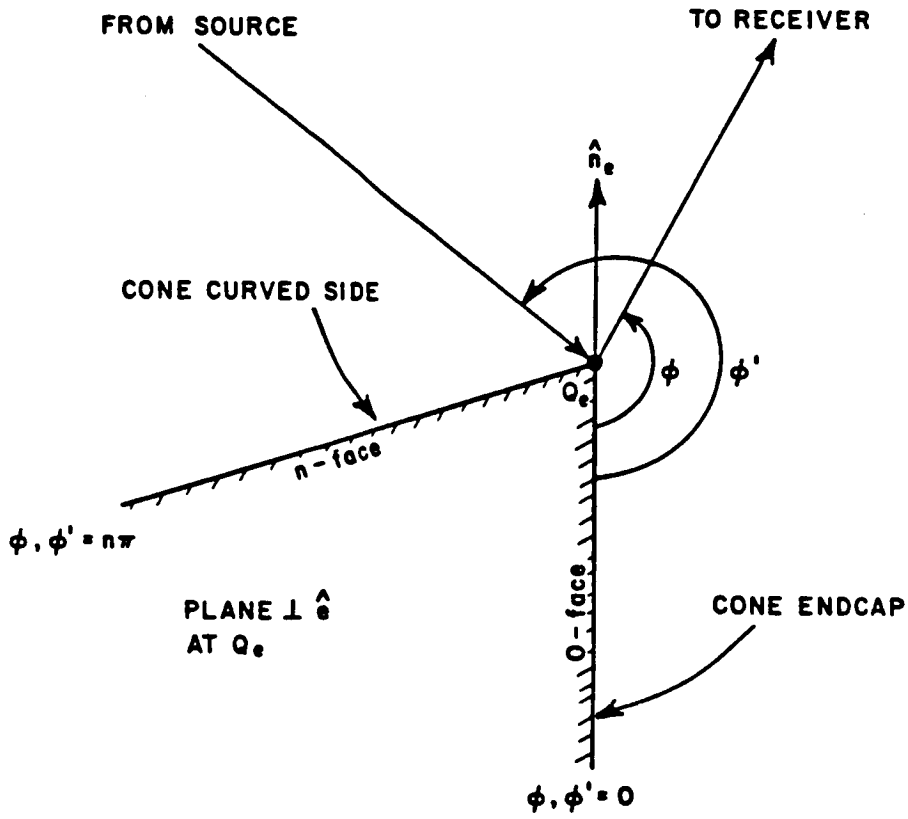

Figure 13: Cone frustum edge geometry.

Transformation of Coordinates

The expression for the diffracted field from an edge uses the coordinates (r,β_0,Φ) which is a ray-fixed coordinate system at the edge. In order to find the incident fields and to sum the fields in the next step, it is necessary to convert to a common set of coordinates which we defined as (r,θ,ϕ)(see Figure 14).

Let

$$\begin{aligned}
\hat{d} &= \hat{r} \text{ or } \hat{r}' \\
\hat{n}_o &= \text{unit normal to the endcap (o-face)} \\
\hat{b} &= \text{unit binormal vector} \\
&= -(\hat{x}\cos\phi_e + \hat{y}\sin\phi_e) \\
\hat{e} &= \text{unit edge vector, and} \\
&= \hat{b} \times \hat{n}_o \,.
\end{aligned}$$

In the principal plane, one finds that

$$\hat{n}_o = \begin{cases} +\hat{z} & \text{for } Q_1, Q_3 \\ -\hat{z} & \text{for } Q_2, Q_4 \end{cases} \tag{3.38}$$

$$\hat{b} = \begin{cases} +\hat{x} & \text{for } Q_3, Q_4 \\ -\hat{x} & \text{for } Q_1, Q_2 \end{cases} \tag{3.39}$$

$$\hat{e} = \begin{cases} +\hat{\phi} & \text{for } Q_1, Q_3 \\ -\hat{\phi} & \text{for } Q_2, Q_4. \end{cases} \tag{3.40}$$

Since $\hat{d}$ is the same for both coordinate systems, we can set them equal such that

$$\begin{aligned}
\hat{d} &= \hat{x}\sin\theta\cos\phi + \hat{y}\sin\theta\sin\phi + \hat{z}\cos\theta \\
&= \hat{b}\sin\beta_0\cos\Phi + \hat{n}_o\sin\beta_0\sin\Phi + \hat{e}\cos\beta_0 \,.
\end{aligned} \tag{3.41}$$

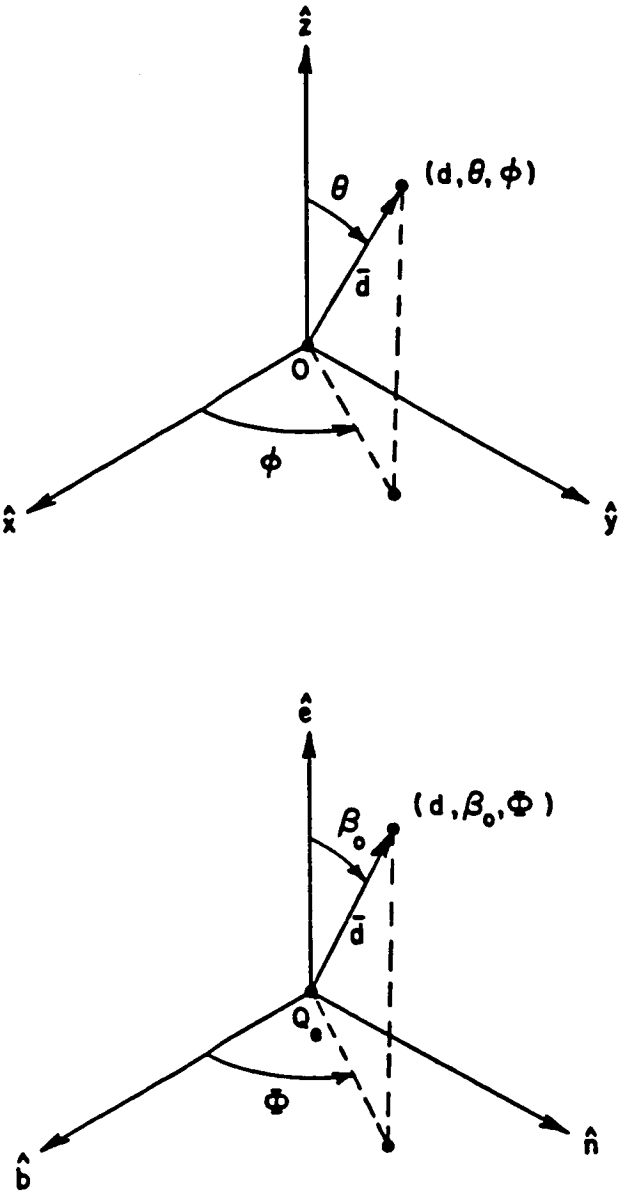

Figure 14: The (d,θ,ϕ) and (d,β_0,Φ) coordinate systems.

Noting that

$$\hat{n}_o \cdot \hat{d} = \sin\beta_0 \sin\Phi$$

$$\hat{b} \cdot \hat{d} = \sin\beta_0 \cos\Phi$$

$$\frac{\hat{n}_o \cdot \hat{d}}{\hat{b} \cdot \hat{d}} = \tan\Phi$$

$$\Phi = \tan^{-1}\left(\frac{\hat{n}_o \cdot \hat{d}}{\hat{b} \cdot \hat{d}}\right) \tag{3.42}$$

$$\beta_0 = \cos^{-1}(\hat{e} \cdot \hat{d}) \tag{3.43}$$

and

$$\hat{\Phi} = \frac{\hat{e} \times \hat{d}}{|\,\hat{e} \times \hat{d}\,|} \tag{3.44}$$

$$\hat{\beta}_0 = -\hat{\Phi} \times \hat{d}\,. \tag{3.45}$$

The above expressions are best carried out on the computer. Expanding them out in terms of θ and ϕ can become a trigonometric mess. But in the principal plane,

for $\phi = 0$,

$$\hat{\beta}_0 = \begin{cases} +\hat{\phi} & \text{for } Q_2, Q_4 \\ -\hat{\phi} & \text{for } Q_1, Q_3 \end{cases} \tag{3.46}$$

$$\hat{\Phi} = \begin{cases} +\hat{\theta} & \text{for } Q_1, Q_4 \\ -\hat{\theta} & \text{for } Q_2, Q_3. \end{cases} \tag{3.47}$$

for $\phi = \pi$,

$$\hat{\beta}_0 = \begin{cases} +\hat{\phi} & \text{for } Q_1, Q_3 \\ -\hat{\phi} & \text{for } Q_2, Q_4 \end{cases} \tag{3.48}$$

$$\hat{\Phi} = \begin{cases} +\hat{\theta} & \text{for } Q_2, Q_3 \\ -\hat{\theta} & \text{for } Q_1, Q_4. \end{cases} \tag{3.49}$$

3.4.4 The Diffraction-Point Method Solution

The diffraction-point method solution is obtained by summing the diffracted fields from each edge. The scattered field is approximately

$$\vec{E}^s \approx \vec{E}^d_{total} = \vec{E}^d_1 + \vec{E}^d_2 + \vec{E}^d_3 + \vec{E}^d_4 \tag{3.50}$$

where

$$\vec{E}^d_1 = \vec{E}^i(Q_1) \cdot \overline{\overline{D}}(Q_1) \sqrt{\rho^d(Q_1)} e^{jk\vec{r}_1 \cdot \hat{r}} \frac{e^{-jkr}}{r} \tag{3.51}$$

$$\vec{E}^d_2 = \vec{E}^i(Q_2) \cdot \overline{\overline{D}}(Q_2) \sqrt{\rho^d(Q_2)} e^{jk\vec{r}_2 \cdot \hat{r}} \frac{e^{-jkr}}{r} \tag{3.52}$$

$$\vec{E}^d_3 = \vec{E}^i(Q_3) \cdot \overline{\overline{D}}(Q_3) \sqrt{\rho^d(Q_3)} e^{jk\vec{r}_3 \cdot \hat{r}} \frac{e^{-jkr}}{r} \tag{3.53}$$

$$\vec{E}^d_4 = \vec{E}^i(Q_4) \cdot \overline{\overline{D}}(Q_4) \sqrt{\rho^d(Q_4)} e^{jk\vec{r}_4 \cdot \hat{r}} \frac{e^{-jkr}}{r}. \tag{3.54}$$

Please keep in mind that $\vec{E}^d_e = 0$ if the diffraction point is shadowed or not visible (see Figure 12). As an example, the diffraction-point method solution for which the source is in Region B and receiver in Region C is

$$\vec{E}^s \approx \vec{E}^d_1 + \vec{E}^d_2 \tag{3.55}$$

which can also be written as

$$\vec{E}^s \approx \hat{\phi} E^i_\phi e^{-jkr'} \frac{e^{-jkr}}{r} \quad \left[D_s(Q_1) \sqrt{\rho^d(Q_1)} e^{jk\vec{r}_1 \cdot (\hat{r} + \hat{r}')} \right.$$

$$- D_s(Q_2)\sqrt{\rho^d(Q_2)}e^{jk\vec{r}_2\cdot(\hat{r}+\hat{r}')}\Big]$$

$$-\hat{\theta}E_\theta^i e^{-jkr'}\frac{e^{-jkr}}{r} \quad \Big[D_h(Q_1)\sqrt{\rho^d(Q_1)}e^{jk\vec{r}_1\cdot(\hat{r}+\hat{r}')}$$

$$- D_h(Q_2)\sqrt{\rho^d(Q_2)}e^{jk\vec{r}_2\cdot(\hat{r}+\hat{r}')}\Big] . \qquad (3.56)$$

3.4.5 Calculated Principal Plane Patterns Using the Diffraction-Point Method

The patterns shown in Figure 15 and 16 are typical scattering patterns for a circular cone frustum in the principal plane which were calculated using the diffraction-point method. The horizontal axis is the aspect angle which is measured from the z-axis. The vertical axis is the radar cross section in decibels above a square meter.

The diffraction-point method solution provides a fairly good approximate solution, but it doesn't work everywhere. It fails in the regions near the forward scatter direction, the specular direction off the endcaps, and in the specular direction off the curved side. Since these are directions of significant scattering, we cannot ignore these problems.

The observed failure is due to elements which are missing in the present solution. We recall that for some regions, diffracted ray contributions come from the entire rim. This is called a "rim caustic" (a system of parallel rays from the rim creates a caustic at infinity), and it cannot be handled by the ordinary diffraction-point method. From the law of edge diffraction, these caustics occur in the specular direction off the endcap (which can involve both front and back rims) and in the forward scatter direction. To correct the diffraction-point method solution, the contributions from the rims must be considered and added to the solution. In Chapter 5, we will show how this can be accomplished.

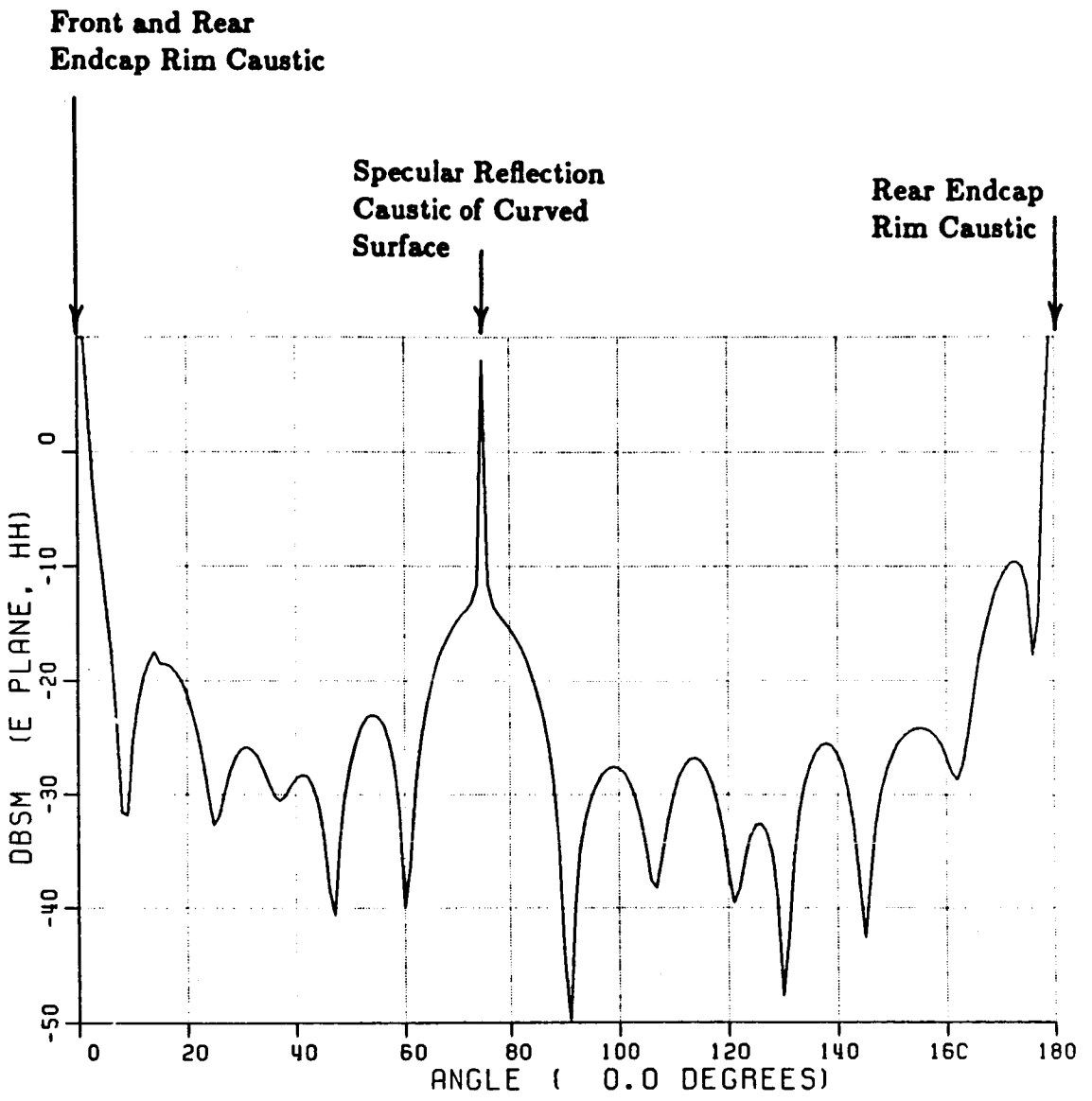

Figure 15: The calculated pattern of a 15° cone frustum using the diffraction-point method for backscatter.

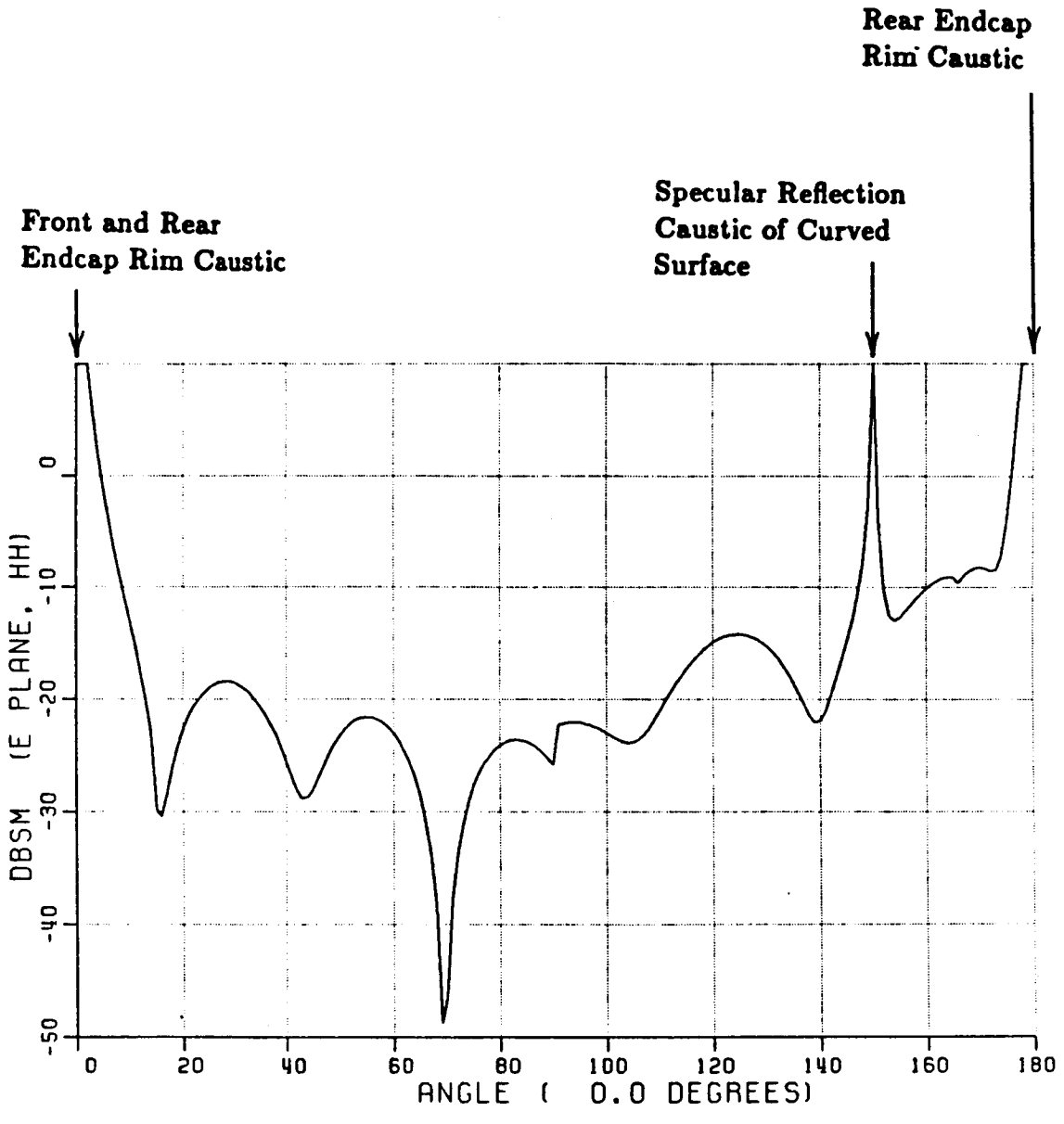

Figure 16: The calculated pattern of a 15° cone frustum using the diffraction-point method for bistatic scatter with fixed axial incidence at 0 degrees.

Next we need to explain why the solution fails near the specular direction off the curved side. This direction also corresponds to a caustic—since reflected ray contributions come from the entire side of the cone frustum. However this caustic does not present quite the same problem as for the rim caustic. The diffraction-point method solution, to some degree, does take care of some reflection caustics, since the diffraction-point method solution does work for a cylinder [1]. Let us take a closer look at the diffraction-point method solution near the specular direction for the curved side. We note that in Eq. (3.50), as one approaches the specular direction, the solution becomes dominated by the diffracted fields coming from the two edges forming the reflecting surface. In the region near specular, one finds that

$$e^{jk\vec{r}_1\cdot(\hat{r}+\hat{r}')} \approx e^{jk\vec{r}_2\cdot(\hat{r}+\hat{r}')}$$

$$D_{s,h}(Q_{1,2}) \to \infty$$

and

$$\begin{aligned}\vec{E}^s \approx & \left\{\hat{\phi}E^i_\phi\left[D_s(Q_1)\frac{\sqrt{\rho^d(Q_1)}}{r} - D_s(Q_2)\frac{\sqrt{\rho^d(Q_2)}}{r}\right] + \right. \\ & \left. +\hat{\theta}E^i_\theta\left[D_h(Q_2)\frac{\sqrt{\rho^d(Q_2)}}{r} - D_h(Q_1)\frac{\sqrt{\rho^d(Q_1)}}{r}\right]\right\}\cdot \\ & \cdot e^{-jk(r+r')}e^{jk\vec{r}_1\cdot(\hat{r}+\hat{r}')}\,. \end{aligned} \tag{3.57}$$

The GTD diffraction coefficients for the two dominant edges become infinite in the specular direction. "Infinite" because the diffraction coefficients arise from a "semi-infinite" wedge solution —the reflected field from a semi-infinite wedge is infinite in the far zone. The two dominant edge-diffracted fields have opposite signs; each contains the (infinite) diffraction coefficient weighted by the spread factor which contains the radius of edge curvature. We note that if the radius of

curvature is equal for both edges, as in the case of a cylinder, the total field at specular will be correct. The infinities will cancel each other, leaving the correct bounded result. However, for the cone frustum, due to the difference in the radius of curvature (spread factor) at each edge, this cancellation of infinities does not occur, and the solution fails.

This failure is due to the missing information about the cone's surface. The edge diffraction coefficients have no knowledge of the variation in curvature along the cone's side. This information is necessary in order to determine the correct reflected field. If one looks at the situation in terms of rays, there are reflected ray contributions to the reflected field from the entire side of the cone (a caustic). Each spreads energy differently depending on the radii of curvature at the point of reflection. Since this information is not built into the diffraction coefficients, the diffracted field is not able to go to the reflected field at the specular direction. In the next chapter we will look at ways to correct for this failure.

CHAPTER IV

Curved-Surface Specular-Region Corrections

4.1 Introduction.

In the preceding chapter, we discussed the failures of the diffraction-point method solution. This chapter is devoted to fixing one of them—the failure in the specular region for the curved surface.

As mentioned in Chapter 1, we want to avoid changing back and forth between different forms of the solution, such as between GTD and PO. Instead, we would like to preserve the GTD form of the solution in all regions. Corrections will be accomplished through a modification to the present GTD solution. Two different modifications will be presented. One we will call the "spread-factor modification" which was shown in a Ph.D. dissertation by T.T. Chu [8] based on similar work by Ryan [9]. And the other is a new way that we will call the "equivalent- line-current correction".

4.2 Physical Optics Result

In the specular direction, the result based on physical optics gives a good approximate value for the scattered field. We will use this result to check our solution in later sections. The scattered field (expressed as a radar cross section) is given by [4]

$$\sigma(\text{at specular}) = \frac{8\pi}{9\lambda}\frac{(a_2^{3/2} - a_1^{3/2})}{\sin^2\alpha_c \cos\alpha_c}\cos\left(\frac{\beta_s}{2}\right) \tag{4.58}$$

where β_s is the azimuth bistatic angle (see Figure 10).

4.3 Spread-Factor Modification

In Chapter 2, we showed that the diffraction-point solution failed in the specular direction due to an incomplete cancellation of infinities. This was caused by a difference in the spread factors for the two edges forming the reflecting surface. The spread factors contain the caustic distances which differ due to the different radii of edge curvature. Chu has shown that by introducing a modified spread factor, one can obtain a finite and valid result for the UTD solution in the specular direction. The modified spread factor is called the "average" spread factor; it is used in place of the actual spread factors for the two edges forming the face (n-face). The average spread factor is given by

$$A_{ave} = \frac{\sqrt{\rho^d_{ave}}}{r} \tag{4.59}$$

where

$$\sqrt{\rho^d_{ave}} = \frac{1}{L}\int_{-L/2}^{L/2} \sqrt{\rho^d(Q_2) + \frac{z+\frac{L}{2}}{L}[\rho^d(Q_1) - \rho^d(Q_2)]}\, dz \tag{4.60}$$

$$= \frac{2}{3}\left[\frac{\rho^d(Q_1)^{3/2} - \rho^d(Q_2)^{3/2}}{\rho^d(Q_1) - \rho^d(Q_2)}\right] . \tag{4.61}$$

Note that the spread factor is no longer local for each edge of the frustum.

The scattered field with Chu's modified spread factor can be written in the same form as the diffraction-point method solution, Equation (3.50), except that the diffraction coefficient is now given by

$$D_{s,h} = \frac{-e^{-j\frac{\pi}{4}}}{2n\sqrt{2\pi k}\sin\beta_0} \cdot \left\{ D^{in} + D^{io} \mp \left(D^{rn}\frac{\sqrt{\rho^d_{ave}}}{\sqrt{\rho^d(Q_e)}} + D^{ro}\right)\right\} \tag{4.62}$$

where

$$D^{in} = \cot\left(\frac{\pi + (\Phi - \Phi')}{2n}\right)$$
$$D^{io} = \cot\left(\frac{\pi - (\Phi - \Phi')}{2n}\right)$$
$$D^{rn} = \cot\left(\frac{\pi + (\Phi + \Phi')}{2n}\right)$$
$$D^{ro} = \cot\left(\frac{\pi - (\Phi + \Phi')}{2n}\right) .$$

4.3.1 Calculated Patterns Using the Spread-Factor Modification

Figure 17 compares the patterns calculated by the original diffraction-point method solution with the diffraction-point method solution using the spread-factor modification. Note that the spike at the specular direction is now gone. It can be verified that the solution using the spread-factor modification gives the physical optics result, Eq. (4.58), at the specular direction. However, we can also see that the modification has slightly affected the pattern outside of the specular region. The modified solution does not exactly go to the diffraction-point method solution outside the specular region—it is not a uniform solution.

The integral in Eq. (4.60) may be viewed as being related to the integral of the in-phase currents that give rise to the PO scattered field in the specular direction. The lack of a uniform solution is a result of the phase not being considered in the integral for the calculation of the average spread factor.

Even though the solution is not uniform, the spread-factor modification is sufficiently accurate for small cone angles. It has the advantages of being extremely easy to apply and fast to compute. But for larger cone angles a better correction is needed. Next we will investigate a correction that is based on the use of "equivalent line currents".

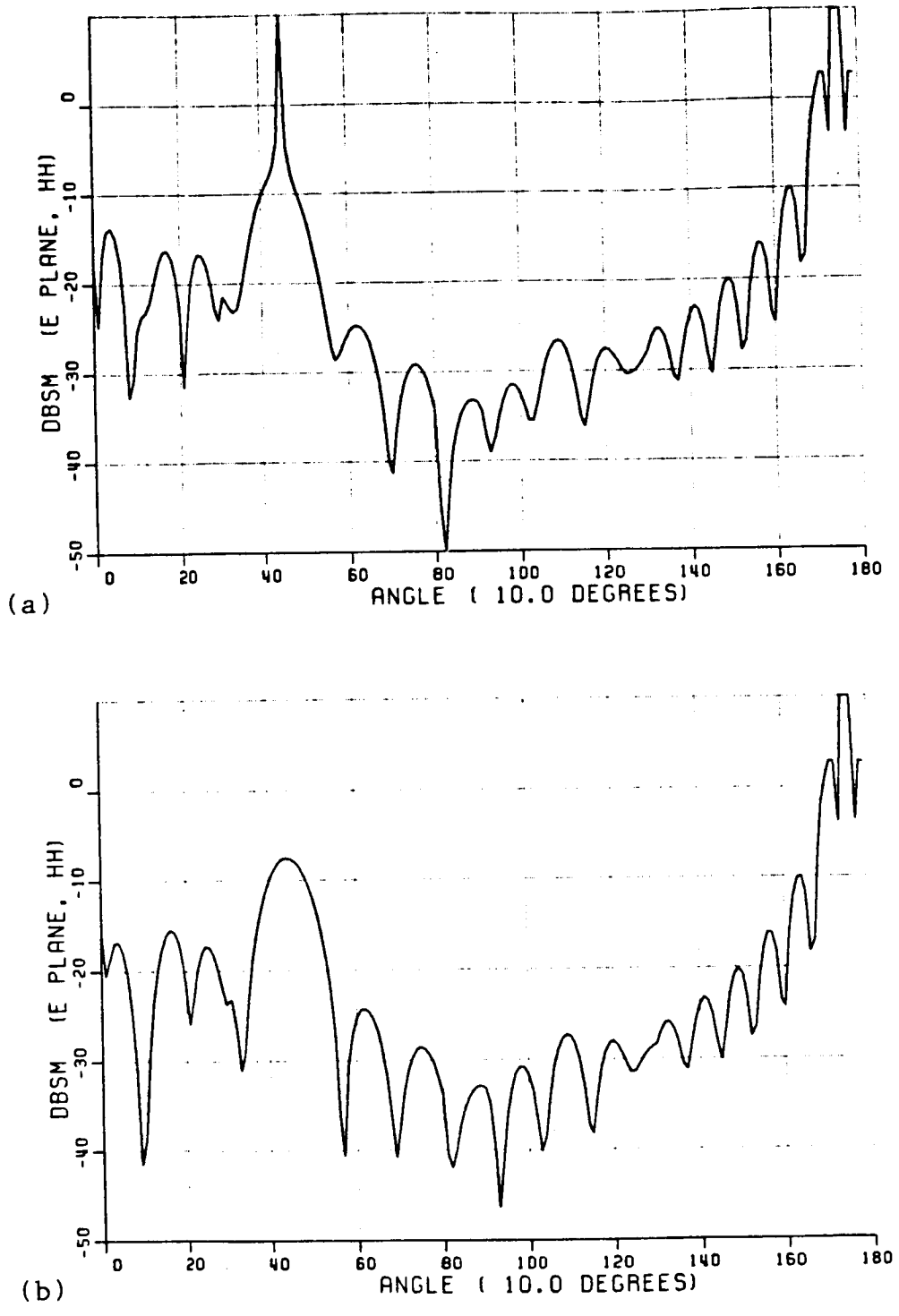

Figure 17: Bistatic 10° scatter from a 40° cone using (a) the diffraction-point method, and (b) the diffraction-point method with spread-factor modification.

4.4 GO Equivalent-Line-Current Correction

The "equivalent current concept" is a technique that can evaluate the fields in a caustic region. Recall from Chapter 3 that we have a system of parallel reflected rays off the curved surface of the frustum which creates a caustic at infinity. Ordinary GO expressions cannot be used to find this reflected field. However, by using "GO equivalent line currents", the reflected field in the caustic region may be determined [1,12].

Now one might ask, how can we correct the diffraction-point solution by using this technique? This is not an easy question. The approach uses a great deal of heuristic argument and physical intuition, but we will show later that it is possible. The observations used by K.C. Chiang [1] for the cylinder give us an idea how this may be accomplished.

Chiang had obtained an equivalent-line-current expression for the reflected field from a cylinder. She also did an asymptotic evaluation of the physical optics solution for an open (no endcaps) cylinder and found that it gave a similar result. (And we recall that PO also provides an accurate result in the specular region.) Chiang then observed the similarity of the cylinder's equivalent-line-current solution with the portion of the diffraction-point method solution that corresponds to the reflection boundary (RB) of the curved surface. And it was then rationalized by Chiang that they could be set equal.

For the cone frustum, we will assume a similar situation where the equivalent-line-current solution will yield a PO-type result that is similar in form to the RB portion of the diffraction-point method solution (except for the failure in the specular region). We cannot justify a direct subsitution for the two solutions, but this gives us some insight that it might be possible to provide a "modified"

equivalent-line-current solution to replace the RB portion of the diffraction-point method solution that fails in the specular region. We will return to the subject of correcting the diffraction-point method solution after showing the formulation of the equivalent-line-current solution.

4.4.1 Equivalent-Line-Current Solution Procedure

The following steps are used to find the equivalent-line-current solution for the cone frustum:

1. First, the GO reflected field over an infinite cylinder is obtained (a two-dimensional problem).

2. Next, the radiated fields from infinite traveling-wave line currents, $\vec{I}^e$ and $\vec{I}^m$, are determined. $\vec{I}^e$ is an electric current and $\vec{I}^m$ is a magnetic current.

3. The currents $\vec{I}^e$ and $\vec{I}^m$ are substituited for the cylinder's surface, and the currents $\vec{I}^e$ and $\vec{I}^m$ are then adjusted so that they give the same field as the GO reflected field. In the principal plane, $\vec{I}^e$ gives a horizontally polarized field, and $\vec{I}^m$ gives a vertically polarized field. The currents $\vec{I}^e$ and $\vec{I}^m$ are the "GO equivalent line currents" for the cylinder. These are "fictitious" currents that vary with the observation position.

4. The cylinder's equivalent line currents are broken up into infinitesimal current elements (see Figure 18). The current elements are placed at the equivalent location of the cone's reflecting surface, and they are varied according to the local radius of curvature for the "equivalent cylinder" at that point.

5. The radiated fields due to the above currents are evaluated. This involves a line integral. The resulting expression is the equivalent-line-current solution.

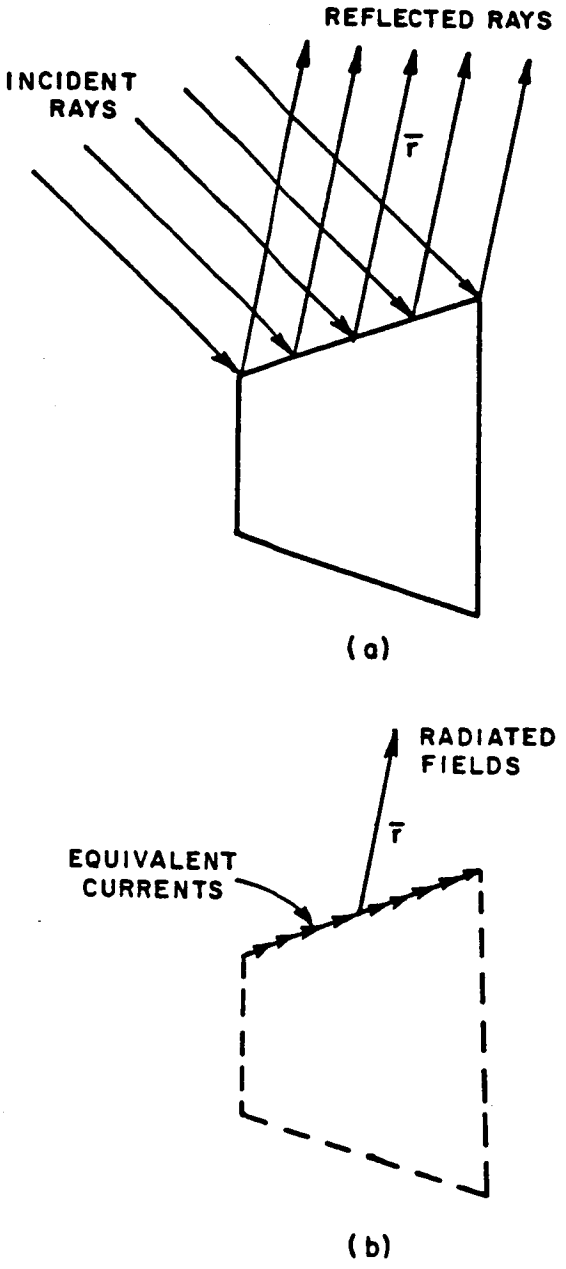

Figure 18: The GO reflected field off the curved side of the cone frustum produced by (a) rays, and (b) equivalent currents.

It gives the correct value of the reflected field off the curved-side of the cone frustum.

The preceding steps will be shown in greater detail on the following pages.

4.4.2 GO Reflected Field Over an Infinite Circular Cylinder

The GO reflected field can be obtained using Equations (2.1) and (2.4) in Chapter 2. For a circular cylinder with plane-wave incidence, the expressions simplify greatly. For a circular cylinder, $R_1 = a$ and $R_2 = \infty$. The values for ρ_g and ρ_t can be determined by using Euler's equation (see Figure 19 and Figure 20) such that

$$\frac{1}{\rho_g} = \frac{1}{a}\cos^2\alpha \tag{4.63}$$

$$\frac{1}{\rho_t} = \frac{1}{a}\sin^2\alpha\,. \tag{4.64}$$

Substituting for $R_{1,2}$, f, ρ_g, and ρ_t in the expressions for $\rho^r_{1,2}$ yields

$$\frac{1}{\rho^r_1} = \frac{2}{a}\left(\frac{\cos^2\alpha + \cos^2\theta^i \sin^2\alpha}{\cos\theta^i}\right) \tag{4.65}$$

$$\frac{1}{\rho^r_2} = 0\,. \tag{4.66}$$

If an angle β is used, where

$$\beta = \cos^{-1}\left(\hat{s}^r \cdot \hat{u}_2\right) \tag{4.67}$$

then

$$\rho^r_1 = \frac{a}{2}\frac{\hat{s}^r \cdot \hat{n}}{\sin^2\beta} \tag{4.68}$$

$$\rho^r_2 = \infty\,. \tag{4.69}$$

Approximations for the far field can be made (see Figure 21) such that

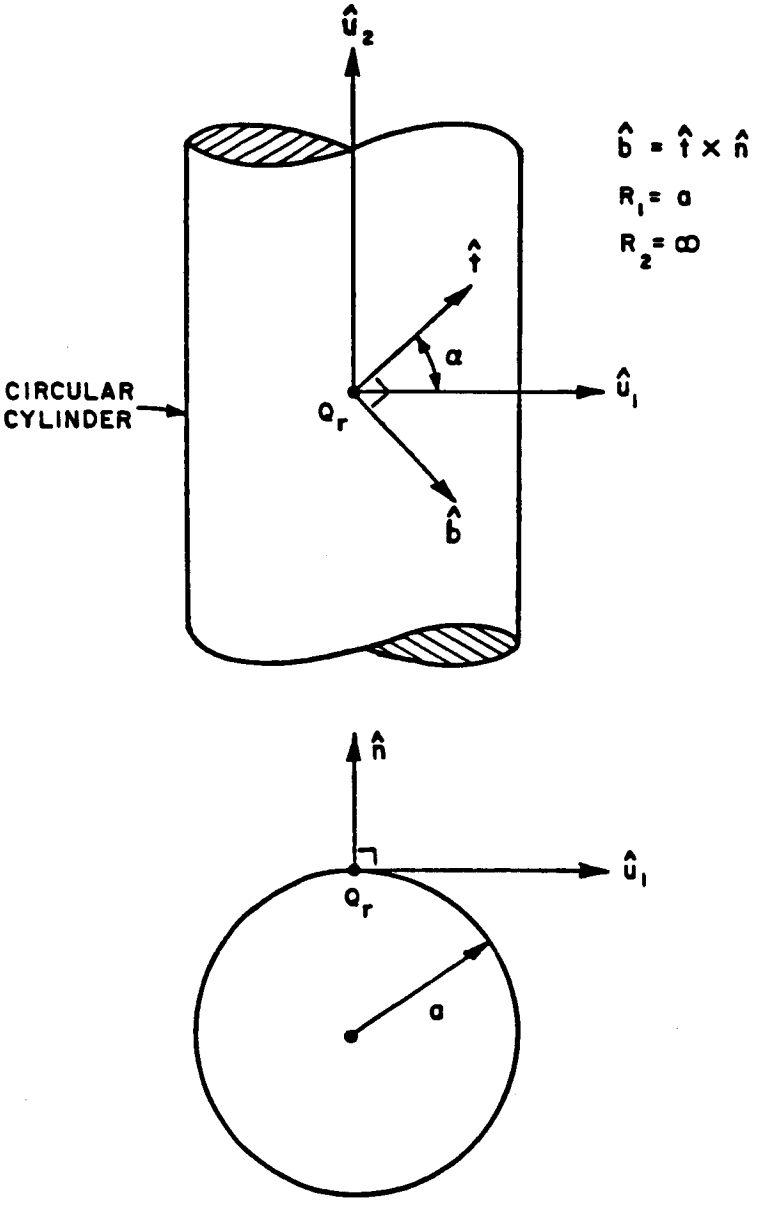

Figure 19: Reflected field geometry for the cylinder.

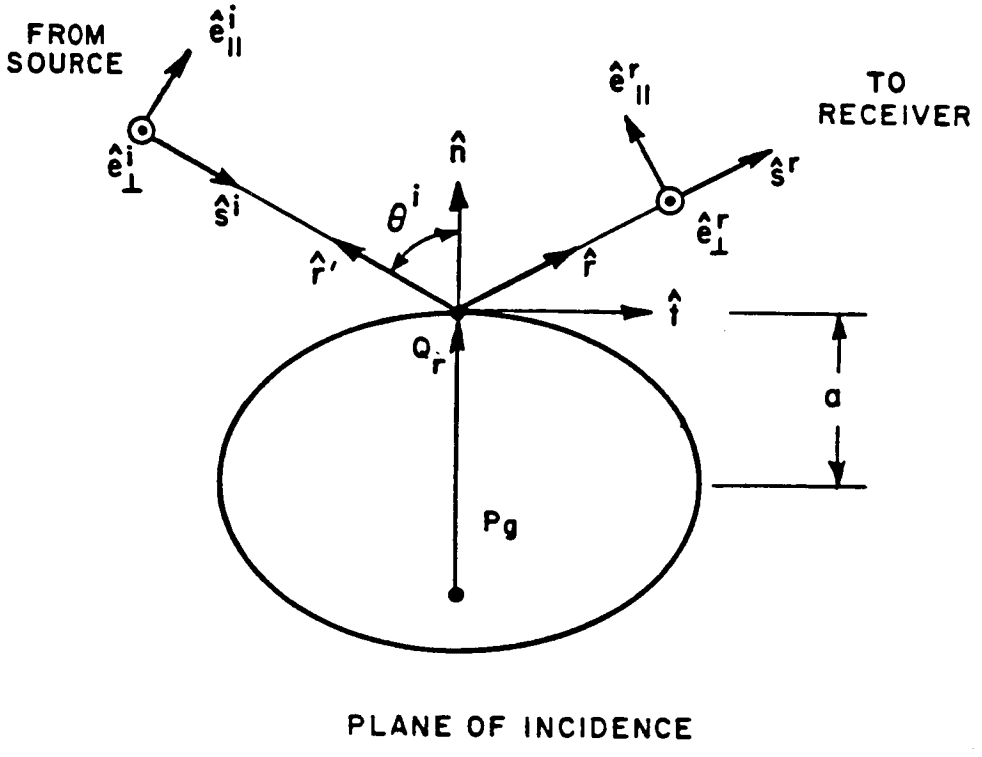

Figure 20: Reflected field geometry for the cylinder in the plane of incidence.

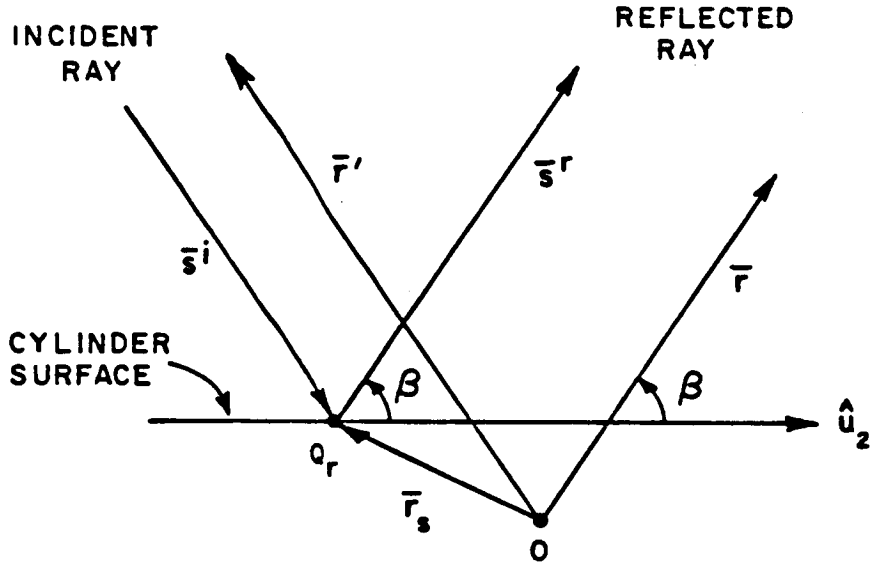

Figure 21: Reflected ray off cylinder surface.

$$\frac{e^{-jks^r}}{\sqrt{s^r}} \approx e^{jk\vec{r}_s\cdot\hat{r}}\frac{e^{-jkr}}{\sqrt{r}} \tag{4.70}$$

$$e^{-jks^i} \approx e^{jk\vec{r}_s\cdot\hat{r}'}e^{-jkr'} . \tag{4.71}$$

And for a two-dimensional cylinder, the spread factor is

$$\sqrt{\frac{\rho_1^r\rho_2^r}{(\rho_1^r+s^r)(\rho_2^r+s^r)}} \approx \sqrt{\frac{\rho_1^r}{s^r}} . \tag{4.72}$$

Therefore the far-zone GO reflected field is

$$\vec{E}^r \approx \vec{E}^i(0)\sqrt{\rho_1^r}e^{jk\vec{r}_s\cdot(\hat{r}+\hat{r}')}\frac{e^{-jkr}}{\sqrt{r}} \tag{4.73}$$

where the reflection caustic distance ρ_1^r is given in (4.68).

4.4.3 Far-Field Radiation of an Infinite Traveling-Wave Line Source

Let an infinite traveling-wave electric line current be given by

$$\vec{I}^e = \hat{u}I^e e^{-jku\cos\beta} . \tag{4.74}$$

The current flows along the $\hat{u}$-axis where β is the angle measured between the $\hat{u}$-axis and the observation direction, $\hat{s}^r$ (see Figure 22). The far-zone radiated electric field [1] is

$$\vec{E}^e = \hat{\beta}\sqrt{\frac{k}{8\pi}}\eta I^e e^{j\frac{\pi}{4}}\frac{e^{-jks^r}}{\sqrt{s^r}} . \tag{4.75}$$

By using duality we can replace

$$\begin{aligned} \vec{E} &\rightarrow \vec{H} \\ I^e &\rightarrow I^m \\ \eta &\rightarrow \frac{1}{\eta} \\ k &\rightarrow k \end{aligned}$$

and we obtain

$$\vec{H}^m = \hat{\beta}\sqrt{\frac{k}{8\pi}}\frac{1}{\eta}I^m e^{j\frac{\pi}{4}}\frac{e^{-jks^r}}{\sqrt{s^r}} . \tag{4.76}$$

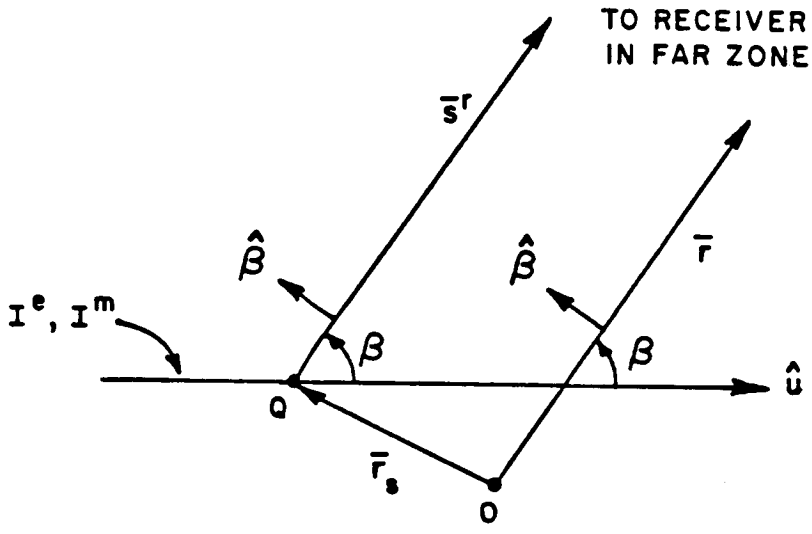

Figure 22: Geometry for line source.

By use of the plane-wave relation, the fields are

$$\vec{H}^e = (\hat{s}^r \times \hat{\beta})\sqrt{\frac{k}{8\pi}} I^e e^{j\frac{\pi}{4}} \frac{e^{jks^r}}{\sqrt{s^r}} \tag{4.77}$$

$$\vec{E}^m = (\hat{\beta} \times \hat{s}^r)\sqrt{\frac{k}{8\pi}} I^m e^{j\frac{\pi}{4}} \frac{e^{jks^r}}{\sqrt{s^r}} . \tag{4.78}$$

If the reference point is moved from the $\hat{u}$-axis origin Q to some other point O, adjustments will have to be made for the phase. In the far field, one obtains

$$s^r \approx \begin{cases} r - \vec{r}_s \cdot \hat{r} & \text{in phase, and} \\ r & \text{in amplitude} \end{cases} \tag{4.79}$$

where $\vec{r}_s$ is the position vector from the reference point to the u-axis origin. The far-zone radiated fields with phase reference at O are as follows:

$$\vec{E}^e = \hat{\beta}\sqrt{\frac{k}{8\pi}} \eta I^e e^{j\frac{\pi}{4}} e^{jk\vec{r}_s \cdot \hat{r}} \frac{e^{-jkr}}{\sqrt{r}} \tag{4.80}$$

$$\vec{H}^e = (\hat{r} \times \hat{\beta})\sqrt{\frac{k}{8\pi}} I^e e^{j\frac{\pi}{4}} e^{jk\vec{r}_s \cdot \hat{r}} \frac{e^{-jkr}}{\sqrt{r}} \tag{4.81}$$

$$\vec{E}^m = (\hat{\beta} \times \hat{r})\sqrt{\frac{k}{8\pi}} I^m e^{j\frac{\pi}{4}} e^{jk\vec{r}_s \cdot \hat{r}} \frac{e^{-jkr}}{\sqrt{r}} \tag{4.82}$$

$$\vec{H}^m = \hat{\beta}\sqrt{\frac{k}{8\pi}} \frac{1}{\eta} I^m e^{j\frac{\pi}{4}} e^{jk\vec{r}_s \cdot \hat{r}} \frac{e^{-jkr}}{\sqrt{r}} . \tag{4.83}$$

4.4.4 Cone Frustum Geometry

To keep the mathematical expressions relatively simple, it is important to choose a good coordinate system. For expressions dealing with equivalent currents

on the curved surface of an elliptical cone frustum, the elliptical cylindrical coordinate system (u, v, z) is chosen. Details on elliptical cylindrical coordinates can be found in Reference [13].

The cone frustum should be aligned properly to take full advantage of the elliptical cylindrical coordinates. The cone axis is the z-axis; the elliptical endcaps are surfaces of constant z. The major axis of the ellipse is oriented with the x-axis, and the minor axis with the y-axis. The curved surface of the cone then corresponds to a surface of constant u. And the equivalent line currents flow on the cone surface, along a line of constant v.

For elliptical cylindrical coordinates,

$$x = (\gamma \cosh u) \cos v \tag{4.84}$$

$$y = (\gamma \sinh u) \sin v \tag{4.85}$$

$$z = z\,. \tag{4.86}$$

Let $a(z)$ be the semimajor axis, and $b(z)$ be the semiminor axis. It can be shown that

$$a = \gamma \cosh u \tag{4.87}$$

$$b = \gamma \sinh u \tag{4.88}$$

where

$$a = a_1 + (z - z_1) \tan \alpha_c \tag{4.89}$$

$$b = \epsilon_c a \tag{4.90}$$

$$a_1 = a(z_1) \tag{4.91}$$

$$a_2 = a(z_2) \tag{4.92}$$

$$\epsilon_c = \text{ellipticity} = \frac{b}{a} \tag{4.93}$$

$$\alpha_c = \text{cone angle} = \tan^{-1}\left(\frac{a_2 - a_1}{z_2 - z_1}\right). \tag{4.94}$$

The following parameters are used in determining the equivalent line currents and their radiated fields (see Figure 23):

$\vec{r}_c$ = position vector from the reference origin to a point on the cone's surface.

$$= a(\hat{x}\cos v + \hat{y}\varepsilon_c \sin v) + \hat{z}z \tag{4.95}$$

$\hat{n}_c$ = unit vector in the direction of the normal to the cone's curved surface.

$$= \frac{\hat{x}\varepsilon_c \cos v + \hat{y}\sin v - \hat{z}\varepsilon_c \tan\alpha_c}{\sqrt{\varepsilon_c^2\cos^2 v + \sin^2 v + \varepsilon_c^2 \tan^2\alpha_c}} \tag{4.96}$$

$\hat{\tau}$ = unit vector tangent to the surface in the direction along the cone's side.

$$= \frac{\tan\alpha_c(\hat{x}\cos v + \hat{y}\varepsilon_c \sin v) + \hat{z}}{\sqrt{\tan^2\alpha_c(\cos^2 v + \varepsilon^2 \sin^2 v) + 1}} \tag{4.97}$$

β = angle between $\hat{\tau}$ and $\hat{r}$.

β' = angle between $\hat{\tau}$ and $\hat{r}'$.

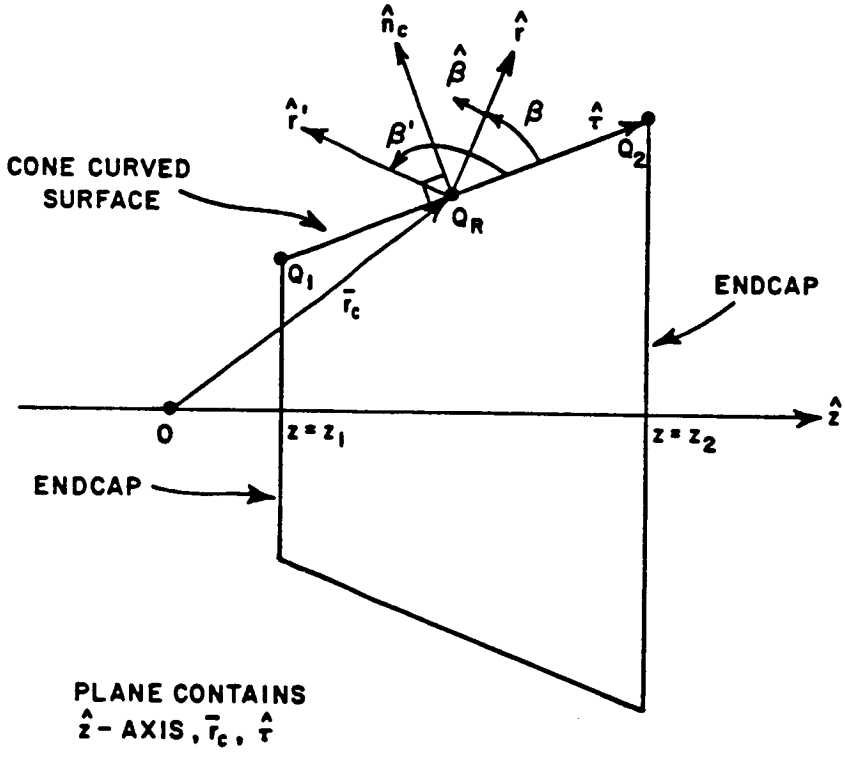

Figure 23: Cone frustum surface geometry

$$\hat{\beta} = \frac{(\hat{\tau} \times \hat{r}) \times \hat{\tau}}{|(\hat{\tau} \times \hat{r}) \times \hat{\tau}|} \tag{4.98}$$

$R^c_{1,2}$ = principal radii of curvature for the cone.

$$R^c_1 = a(z)\frac{(\varepsilon_c^2 \tan^2 \alpha_c + \varepsilon_c^2 \cos v + \sin^2 v)^{3/2}}{\varepsilon_c[\tan^2 \alpha_c(\cos^2 v + \varepsilon_c^2 \sin^2 v) + 1]} \tag{4.99}$$

$$R^c_2 = \infty\,. \tag{4.100}$$

4.4.5 GO Equivalent Line Currents for the Cone Frustum

The equivalent line currents for a cylinder are obtained by setting the infinite cylinder's GO reflected field equal to the field radiated by the infinite line currents. We then solve for the unknown currents. The equivalent line currents for a cylinder are

$$I^e = \hat{\beta} \cdot (\vec{E}^i(0) \cdot \overline{\overline{R}})\sqrt{\frac{8\pi}{k}}\frac{e^{-j\frac{\pi}{4}}}{\eta}\sqrt{\rho_1^r}e^{jk\vec{r}_s \cdot \hat{r}'} \tag{4.101}$$

$$I^m = \hat{\beta} \cdot (\vec{H}^i(0) \cdot \overline{\overline{R}})\sqrt{\frac{8\pi}{k}}\eta e^{-j\frac{\pi}{4}}\sqrt{\rho_1^r}e^{jk\vec{r}_s \cdot \hat{r}'}\,. \tag{4.102}$$

To determine the equivalent line currents for the cone, we replace the position vector $\vec{r}_s$ with $\vec{r}_c$ for the cone frustum, and in ρ_1^r we replace the radius of curvature a with R_1^c for the cone frustum. R_1^c may be viewed as being the equivalent cylinder curvature at the reflection point located by $\vec{r}_c$. The equivalent line currents for the cone frustum are

$$I^e = \hat{\beta} \cdot (\vec{E}^i(0) \cdot \overline{\overline{R}})\sqrt{\frac{8\pi}{k}}\frac{e^{-j\frac{\pi}{4}}}{\eta}\sqrt{\rho_1^r}e^{jk\vec{r}_c \cdot \hat{r}'} \tag{4.103}$$

$$I^m = \hat{\beta} \cdot (\vec{H}^i(0) \cdot \overline{\overline{R}})\sqrt{\frac{8\pi}{k}}\eta e^{-j\frac{\pi}{4}}\sqrt{\rho_1^r}e^{jk\vec{r}_c \cdot \hat{r}'} \tag{4.104}$$

where

$$\rho_1^r = \frac{R_1^c}{2} \frac{\hat{r} \cdot \hat{n}_c}{\sin^2 \beta} . \tag{4.105}$$

4.4.6 Location of Reflection Points on the Cone

It is necessary to determine the points of reflection on the surface of the cone frustum, so that we will know where to place the equivalent line currents. Let Q_r be a point of reflection on the surface of the cone. At Q_r, the law of reflection is satisfied by

$$-\hat{s}^i \cdot \hat{n} = \hat{s}^r \cdot \hat{n} \tag{4.106}$$

where $\hat{n} \cdot \hat{s}^i < 0$ (a closed surface), or

$$\hat{n} \cdot (\hat{s}^r + \hat{s}^i) = 0 . \tag{4.107}$$

The outward normal to the cone surface is given by

$$\hat{n} = \hat{n}_c = \frac{\hat{x}\varepsilon_c \cos v + \hat{y} \sin v - \hat{z}\varepsilon_c \tan \alpha_c}{\sqrt{\varepsilon_c^2 \cos^2 v + \sin^2 v + \varepsilon_c^2 \tan^2 \alpha_c}} . \tag{4.108}$$

Note that for a given cone, $\hat{n}$ is only a function of v. In the far zone, the directions $\hat{s}^r$ and $\hat{s}^i$ are constant over the surface of the cone. Therefore, for a given $\hat{s}^r$ and $\hat{s}^i$, the locus of reflection points is along a line of constant v on the cone's surface. This is a straight line along the side of the cone. The value of v is determined by the reflection point condition, such that

$$\varsigma_x \varepsilon_c \cos v + \varsigma_y \sin v - \varsigma_z \varepsilon_c \tan \alpha_c = 0 \tag{4.109}$$

where

$$\vec{\varsigma} = \hat{s}^i + \hat{s}^r = \hat{x}\varsigma_x + \hat{y}\varsigma_y + \hat{z}\varsigma_z . \tag{4.110}$$

4.4.7 Field Radiated by Equivalent Line Currents

The equivalent line currents will flow along a line of constant coordinate v where the reflection occurs. To find the radiated field, we first use the expression for the field radiated by an infinitesimal dipole with uniform current distribution I_0 and orientation $\hat{l}$ (see Figure 24) which is given by

$$d\vec{E} = \hat{\beta} j\eta \frac{kI_0 dl \sin\beta}{4\pi s} e^{-jks} . \tag{4.111}$$

The field radiated by a current distribution $I(l)\hat{l}$ is found by integration. For a straight line source, one obtains

$$\vec{E} = \hat{\beta} j\eta k \sin\beta \int_{l_1}^{l_2} I(l') \frac{e^{-jks}}{4\pi s} dl' \tag{4.112}$$

and

$$s \approx \begin{cases} r - \vec{r}_c \cdot \hat{r} & \text{in phase, and} \\ r & \text{in amplitude.} \end{cases} \tag{4.113}$$

Therefore the far-zone radiated field is

$$\vec{E} = \hat{\beta} j\eta k \sin\beta \frac{e^{-jkr}}{4\pi r} \int_{l_1}^{l_2} I(l') e^{jk\vec{r}_c \cdot \hat{r}} dl' . \tag{4.114}$$

The far-zone fields due to the equivalent line currents are

$$\vec{E}_e = \hat{\beta} j\eta k \sin\beta \frac{e^{-jkr}}{4\pi r} \int_{\tau_1}^{\tau_2} I^e(\tau') e^{jk\vec{r}_c \cdot \hat{r}} d\tau' \tag{4.115}$$

$$\vec{E}_m = (\hat{\beta} \times \hat{r}) jk \sin\beta \frac{e^{-jkr}}{4\pi r} \int_{\tau_1}^{\tau_2} I^m(\tau') e^{jk\vec{r}_c \cdot \hat{r}} d\tau' . \tag{4.116}$$

Now the problem is to evaluate the integral. We might be able to do it numerically, but then we do not gain much insight into how the solution behaves;

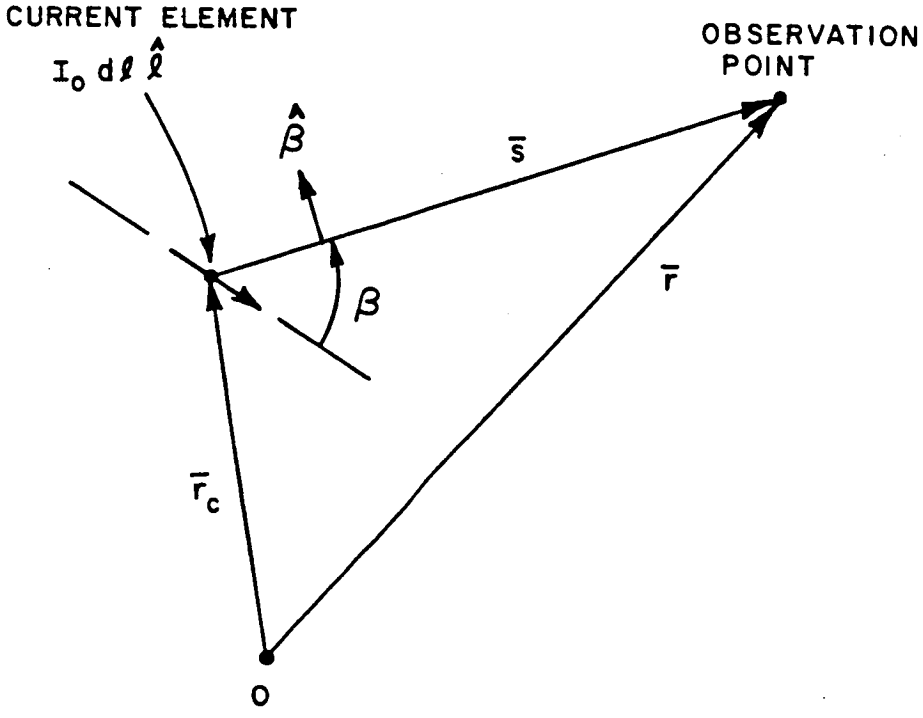

Figure 24: Geometry for radiating current element.

besides, it is inefficient in calculation. We would like to get it in closed form—and it turns out that we can.

With a closed form solution, the result is dependent on only the parameters at the endpoints of the integration. And we note that the endpoints will correspond to the same location as the two diffraction points forming the surface! This gives us another clue that it might be possible to combine the equivalent-line-current result with the diffraction-point method solution.

In the expressions for $\vec{E}^e$ and $\vec{E}^m$, the only parameters that are functions of the integration variable τ are the radius of curvature R_1^c and the position vector $\vec{r}_c$ (see Figure 25). The integral we want to solve is

$$I_1 = \int_{\tau_1}^{\tau_2} \sqrt{R_1^c(\tau')} e^{jk\vec{r}_c\cdot(\hat{r}+\hat{r}')} d\tau' \tag{4.117}$$

$$I_1 = g(v) \int_{\tau_1}^{\tau_2} \sqrt{a(\tau')} e^{jk\vec{r}_c\cdot(\hat{r}+\hat{r}')} d\tau' \tag{4.118}$$

where

$$g(v) = \sqrt{\frac{(\varepsilon_c^2 \tan^2\alpha_c + \varepsilon_c^2 \cos v + \sin^2 v)^{3/2}}{\varepsilon_c[\tan^2\alpha_c(\cos^2 v + \varepsilon_c^2 \sin^2 v) + 1]}}. \tag{4.119}$$

By performing a change in the integration variable from τ' to z',

$$d\tau' = \frac{dz'}{\hat{z}\cdot\hat{\tau}}$$

and we obtain

$$I_1 = \frac{g(v)}{\hat{z}\cdot\hat{\tau}} \int_{z_1}^{z_2} \sqrt{a(z')} e^{jk\vec{r}_c\cdot(\hat{r}+\hat{r}')} dz' \tag{4.120}$$

$$I_1 = \frac{g(v)}{\hat{z}\cdot\hat{\tau}} \int_{z_1}^{z_2} \sqrt{a(z')} e^{jk(af+\delta_z z')} dz' \tag{4.121}$$

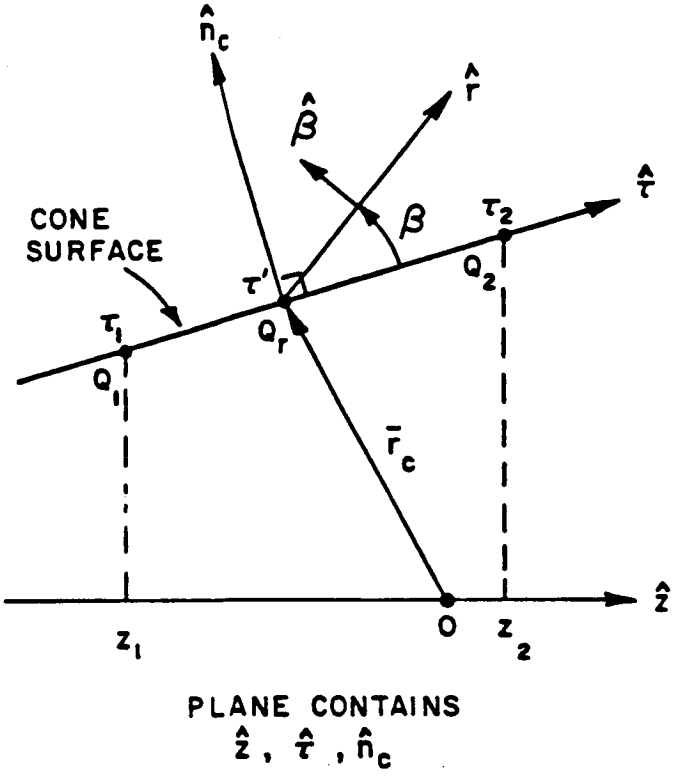

Figure 25: Surface geometry showing $\hat{r}$, $\hat{z}$, and $\vec{r}_c$.

where

$$\vec{\delta} = \hat{r} + \hat{r}' = \hat{x}\delta_x + \hat{y}\delta_y + \hat{z}\delta_z \tag{4.122}$$

$$f = \delta_x \cos v + \delta_y \varepsilon_c \sin v \,. \tag{4.123}$$

Now we perform another change of variables from z' to a, such that

$$z' = a\cot\alpha_c + (z_1 - a_1 \cot\alpha_c) \tag{4.124}$$

$$dz' = \cot\alpha_c da \tag{4.125}$$

$$I_1 = \frac{g(v)}{\hat{z}\cdot\hat{\tau}} \cot\alpha_c e^{jk\delta_z(z_1 - a_1\cot\alpha_c)} \int_{a_1}^{a_2} \sqrt{a} e^{jXa} da \tag{4.126}$$

where

$$X = k(f + \delta_z \cot\alpha_c) \,. \tag{4.127}$$

Let

$$I_2 = \int_{a_1}^{a_2} \sqrt{a} e^{jXa} da \,. \tag{4.128}$$

The integral I_2 can be evaluated in a couple of different ways. Both give a result that uses the confluent hypergeometric function **M** or **U** in which case

$$\begin{aligned} I_2 &= -\int_0^{a_1} \sqrt{a} e^{jXa} da + \int_0^{a_2} \sqrt{a} e^{jXa} da \\ &= -\frac{2}{3} a_1^{\frac{2}{3}} e^{jXa_1} \mathbf{M}(1, 2.5, -jXa_1) \\ &\quad + \frac{2}{3} a_2^{\frac{2}{3}} e^{jXa_2} \mathbf{M}(1, 2.5, -jXa_2) \,. \end{aligned} \tag{4.129}$$

By using the knowledge that

$$\int_0^{\infty} \sqrt{a} e^{jXa} da - \int_0^{-\infty} \sqrt{a} e^{jXa} da = 0 \tag{4.130}$$

and adding (4.130) to (4.129) gives

$$I_2 = \int_{a_1}^{\infty} \sqrt{a} e^{jXa} da - \int_{a_2}^{-\infty} \sqrt{a} e^{jXa} da$$

$$= a_1^{\frac{2}{3}} e^{jXa_1} \mathbf{U}(1, 2.5, -jXa_1) - a_2^{\frac{2}{3}} e^{jXa_2} \mathbf{U}(1, 2.5, -jXa_2) \,. \tag{4.131}$$

Information about the functions **M** and **U** is provided in Appendix A.

The far-zone radiated fields due to the equivalent line currents can now be written as

$$\vec{E}_e = \hat{\beta}[\hat{\beta} \cdot (\vec{E}^i(0) \cdot \overline{\overline{R}})] \{ \quad \} \tag{4.132}$$

$$\vec{E}_m = \hat{\beta} \times \hat{r}[\hat{\beta} \cdot (\vec{E}^i(0) \times \hat{r}') \cdot \overline{\overline{R}}] \{ \quad \} \tag{4.133}$$

where

$$\{ \quad \} = \sqrt{\frac{jk}{4\pi}(\hat{r} \cdot \hat{n}_c)} g(v) \frac{\cot \alpha_c}{\hat{z} \cdot \hat{r}} e^{jk\delta_z(z_1 - a_1 \cot \alpha_c)} \frac{e^{-jkr}}{r} I_2 \tag{4.134}$$

$$\vec{E}^i \cdot \overline{\overline{R}} = E^i_{\perp} R_s \hat{e}^r_{\perp} + E^i_{\parallel} R_h \hat{e}^r_{\parallel} \tag{4.135}$$

$$(\vec{E}^i \times \hat{r}') \cdot \overline{\overline{R}} = E^i_{\parallel} R_h \hat{e}^r_{\perp} - E^i_{\perp} R_s \hat{e}^r_{\parallel} \,. \tag{4.136}$$

The total field radiated by the equivalent line currents is the sum of fields due to both electric and magnetic equivalent currents. It can be separated into parallel and perpendicular polarized components such that

$$\vec{E}^r = \vec{E}_e + \vec{E}_m \tag{4.137}$$

$$\vec{E}^r = (\vec{E}^r \cdot \hat{e}^r_{\parallel}) \hat{e}^r_{\parallel} + (\vec{E}^r \cdot \hat{e}^r_{\perp}) \hat{e}^r_{\perp} \tag{4.138}$$

The following relations can be used in Eq. (4.132) and Eq. (4.133):

$$\hat{e}^r_{\parallel} \cdot (\hat{\beta} \times \hat{r}) = \hat{\beta} \cdot (\hat{r} \times \hat{e}^r_{\parallel}) \tag{4.139}$$

$$\hat{r} \times \hat{e}^r_{\parallel} = \hat{e}^r_{\perp} . \tag{4.140}$$

We can show that

$$\vec{E}^r \cdot \hat{e}^r_{\parallel} = E^i_{\parallel} R_h \{ \quad \} \tag{4.141}$$

$$\vec{E}^r \cdot \hat{e}^r_{\perp} = E^i_{\perp} R_s \{ \quad \} . \tag{4.142}$$

There is no cross polarization. The total field that is radiated by the GO equivalent line currents is

$$\vec{E}^r = \vec{E}^i(0) \cdot \overline{\overline{R}} \sqrt{\frac{jk}{4\pi}(\hat{r} \cdot \hat{n}_c)} g(v) \frac{\cot \alpha_c}{\hat{z} \cdot \hat{\tau}} e^{jk\delta_z(z_1 - a_1 \cot \alpha_c)} \frac{e^{-jkr}}{r} I_2 . \tag{4.143}$$

It can be verified that this expression gives the physical optics result of Equation (4.58) in the specular direction. We will call this expression the "equivalent-line-current solution" for the cone frustum.

The equivalent-line-current solution depends only on the conditions at the edges of the cone frustum. We can then manipulate the expression into a form that resembles a sum of diffracted fields from the two edges. After a great deal of work, it can be written in the following form:

$$\begin{aligned} \vec{E}^r \cdot \hat{e}^r_{\perp,\parallel} &= E^i_{\perp,\parallel}(Q_1) D^{PO-}_{s,h}(Q_1) \sqrt{\rho^r_1(Q_1)} \frac{e^{-jks_1}}{s_1} \\ &+ E^i_{\perp,\parallel}(Q_2) D^{PO+}_{s,h}(Q_2) \sqrt{\rho^r_1(Q_2)} \frac{e^{-jks_2}}{s_2} . \end{aligned} \tag{4.144}$$

The points (Q_1 and Q_2) correspond to the same location as the diffraction points associated with that surface. The variables (s_1 and s_2) are the distances from the points (Q_1 and Q_2) to the observation point. The expression contains terms where

the incident field at the edge is multiplied by a factor called the "physical-optics-type" diffraction coefficient for that edge and a local reflection spread factor. We call it a "physical-optics-type" diffraction coefficient because its form is similar to the physical optics diffraction coefficient for a half-plane. The PO-type diffraction coefficients are given by

$$D_{s,h}^{PO-} = -R_{s,h}\frac{e^{-j\frac{\pi}{4}}}{\sqrt{2\pi k}}\frac{\sin\beta}{\cos\beta+\cos\beta'}\mathbf{T}(+jXa_e) \tag{4.145}$$

$$D_{s,h}^{PO+} = +R_{s,h}\frac{e^{-j\frac{\pi}{4}}}{\sqrt{2\pi k}}\frac{\sin\beta}{\cos\beta+\cos\beta'}\mathbf{T}(-jXa_e) \tag{4.146}$$

where

$$X = k\cot\alpha_c(\hat{\tau}\cdot(\hat{r}+\hat{r}')) \tag{4.147}$$

and the function $\mathbf{T}$ is called a "transition function".

Transition Functions

The function $\mathbf{T}$, that we isolated from the equivalent-line- current solution, has different forms depending on how the integration in Equation (4.128) was performed. If it was evaluated as in Equation (4.129), we obtain the transition function,

$$\mathbf{T}(z) = \mathbf{T}_1(z) = \frac{2}{3}z\mathbf{M}(1,2.5,-z)\,. \tag{4.148}$$

Determining the integral as in Equation (4.131) results in

$$\mathbf{T}(z) = \mathbf{T}_2(z) = -z\mathbf{U}(1,2.5,-z) \tag{4.149}$$

where

$$\mathbf{U}(1,2.5,-z) = -\frac{2}{3}\mathbf{M}(1,2.5,-z) + \frac{\sqrt{\pi}}{2}(-z)^{-\frac{3}{2}}e^{-z}\,. \tag{4.150}$$

Physically, $\mathbf{T}_1$ may be viewed as a result due to a finite cone frustum, and $\mathbf{T}_2$ due to a semi-infinite cone frustum. Mathematically, both give the same result when both edges of the reflecting surface are considered.

The confluent hypergeometric functions, **M** and **U**, have series and large argument forms which can be calculated rather quickly on a digital computer (see Appendix A). By using the first few terms of the series and large argument forms, the small and large argument forms of the transition function are the following:

for $|z| \ll 1$,

$$\mathbf{T}_1(z) \approx e^{-z}\left(\frac{2z}{3}+\frac{2z^2}{5}+\frac{z^3}{7}\right) \tag{4.151}$$

$$\mathbf{T}_2(z) \approx e^{-z}\left(\frac{\sqrt{\pi}}{2\sqrt{-z}}+\frac{2z}{3}+\frac{2z^2}{5}+\frac{z^3}{7}\right) \tag{4.152}$$

for $|z| \gg 1$,

$$\mathbf{T}_1(z) \sim 1+\frac{\sqrt{\pi}}{2}e^{\pm j\frac{3}{2}\pi}\frac{e^{-z}}{\sqrt{z}}-\frac{1}{2z}-\frac{1}{4z^2} \tag{4.153}$$

$$\mathbf{T}_2(z) \sim 1-\frac{1}{2z}-\frac{1}{4z^2} \tag{4.154}$$

The magnitude and phase of $\mathbf{T}_1$ and $\mathbf{T}_2$ are shown in Figures 26 and 27 for values of the argument $z = jx$. The transition functions have their greatest effect in the specular region (where the value of the argument is small). The transition functions have little effect outside of the specular region. Both $\mathbf{T}_1$ and $\mathbf{T}_2$ approach unity for large values of the argument.

4.4.8 Modified Equivalent-Line-Current Solution

Now we will return to the question of how to correct the diffraction-point method solution in the specular region. In the equivalent-line- current solution, we obtained a physical optics type diffraction coefficient which is given by

$$D_{s,h}^{PO\mp} = \mp R_{s,h}\frac{e^{-j\frac{\pi}{4}}}{\sqrt{2\pi k}}\frac{\sin\beta}{\cos\beta+\cos\beta'}\mathbf{T}(\pm jXa_e)\,.$$

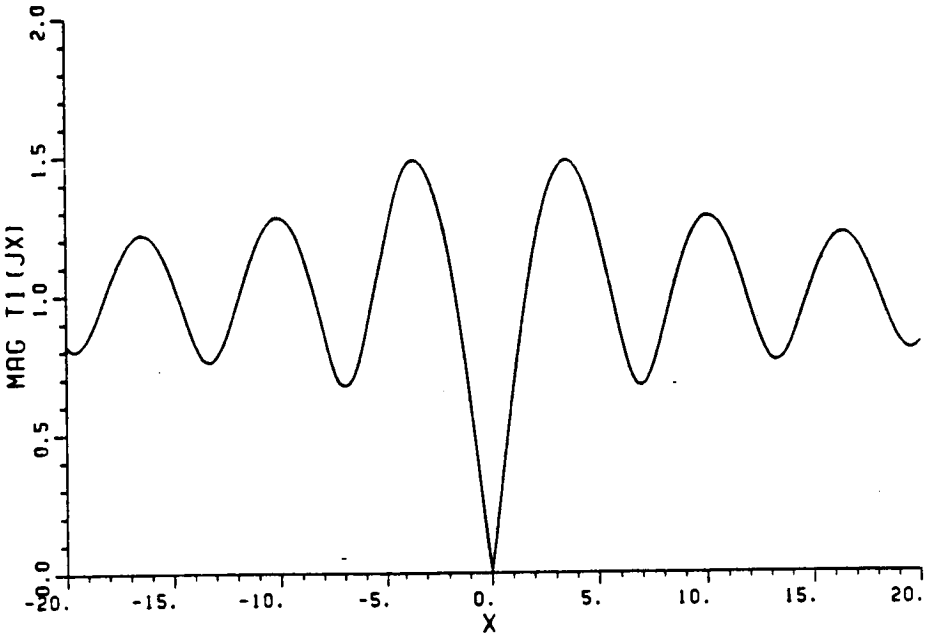

(a)

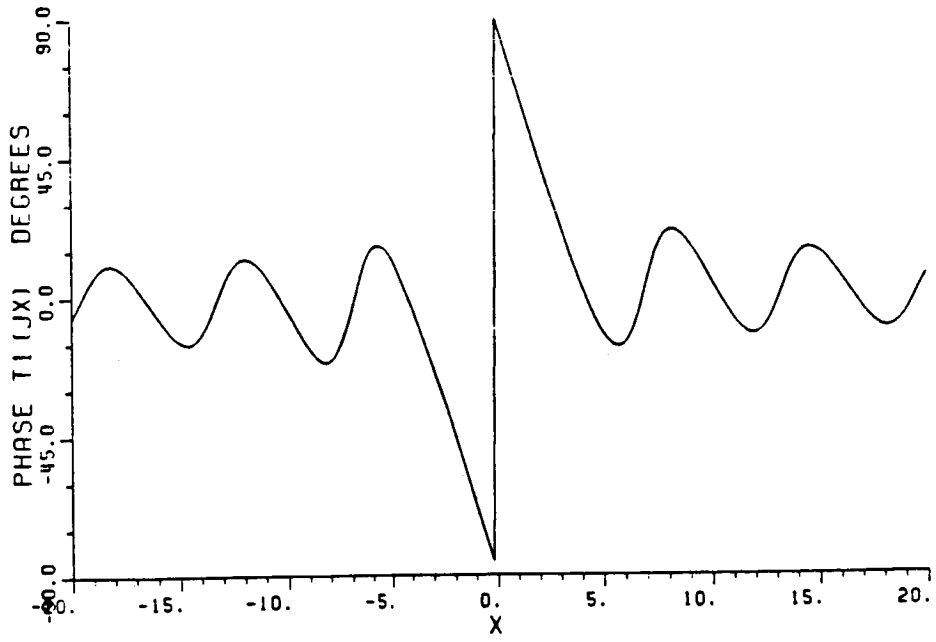

(b)

Figure 26: Transition function $\mathbf{T_1}$ (a) magnitude, and (b) phase.

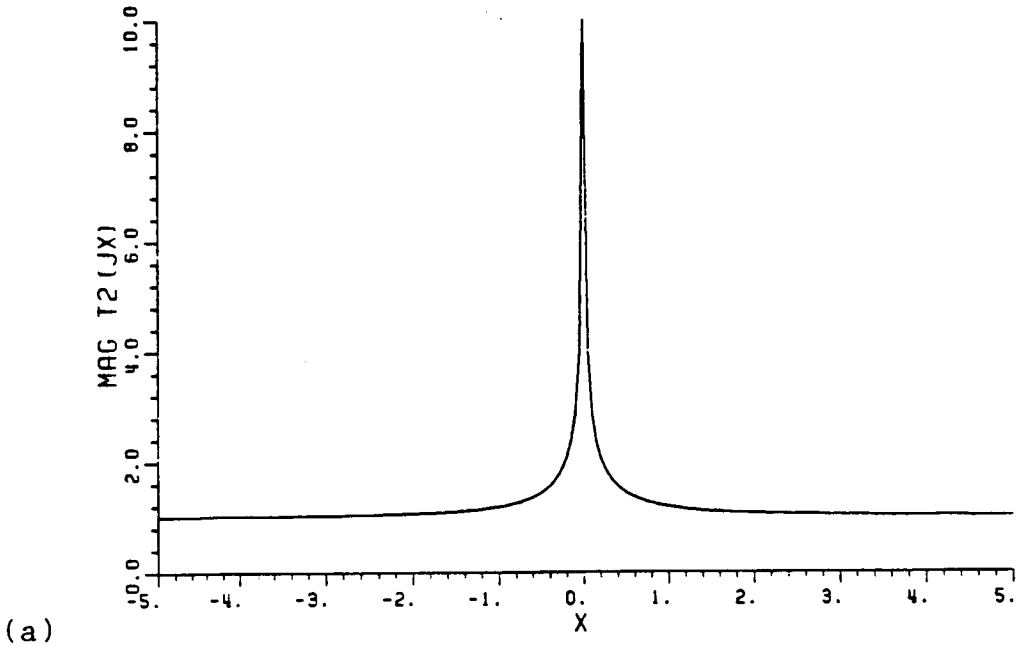

(a)

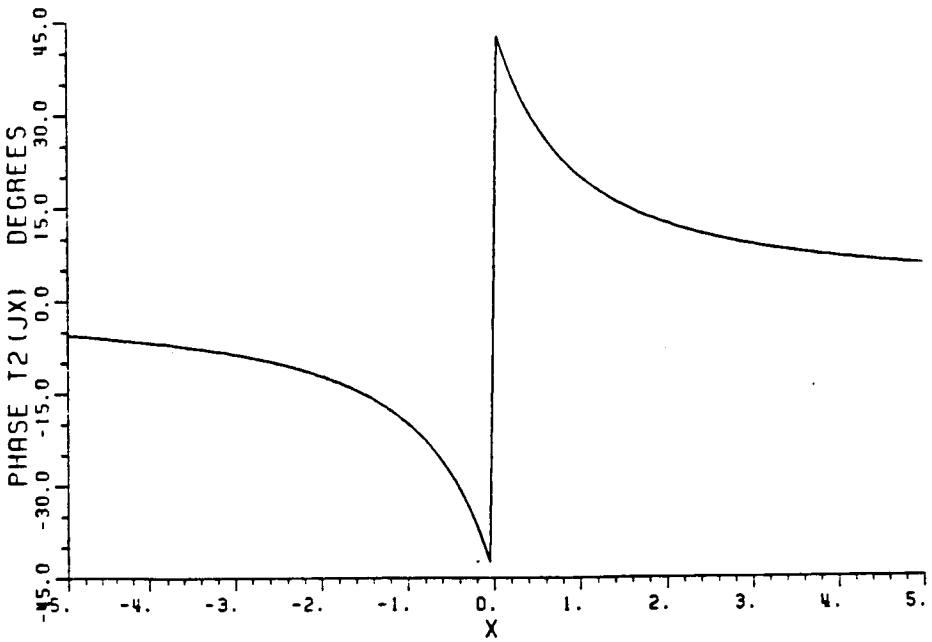

(b)

Figure 27: Transition function $\mathbf{T_2}$ (a) magnitude, and (b) phase.

It resembles the PO diffraction coefficient of a half-plane multiplied by the function **T**. We mentioned earlier that Chiang's asymptotic evaluation of the PO solution for the open cylinder yielded the cylinder's equivalent-line-current solution. Therefore, for the cone frustum, we shall assume that cone frustum's equivalent-line-current solution is the asymptotic PO solution of an open cone frustum.

Let us now proceed with the following line of reasoning towards a "modified" equivalent-line-current solution that may be used to correct the diffraction-point method solution. If the exact currents on the cone frustum were known, we could determine the exact scattered fields. But we do not know the exact currents, so we must rely on the approximations provided by the methods of physical optics and GTD. We know that physical optics provides an accurate representation of the scattered fields in the specular region, but it does not work well outside the specular region due to errors in the edge currents. GTD, on the other hand, provides accurate edge currents, but it fails in the specular region (for the cone frustum) due to the lack of information about the reflecting surface. Somehow there must be a way to combine the desirable characteristics of both PO and GTD to provide an overall accurate representation of the scattered field. This is similar to the philosophy of the physical theory of diffraction (PTD) where a correction, called the fringe current, is added to the PO solution.

Let us further investigate the PO-type diffraction coefficient in the equivalent-line-current solution. We note that the information on the surface curvature is contained within the transition function **T**. The transition function is active only in the specular region. Outside the specular region, we have the PO diffraction coefficient of a half-plane—which is known to be inacurrate.

Let us confine our observation to the plane perpendicular to the edge (see Figure 28). The angle β is converted to ψ which is measured from the curved

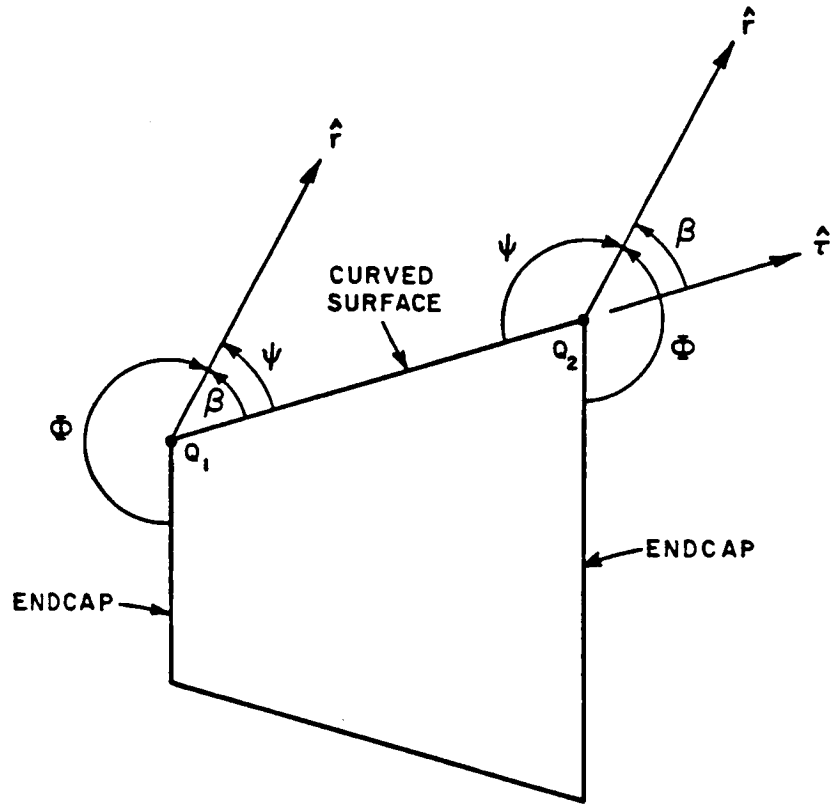

Figure 28: Edge geometry showing the angles ψ, β, and Φ.

surface. Outside the specular region, one finds that

$$\mathbf{T}(\text{outside specular region}) \rightarrow 1 \tag{4.155}$$

$$D_{s,h}^{PO\mp} \approx R_{s,h} \frac{e^{-j\frac{\pi}{4}}}{\sqrt{2\pi k}} \frac{\sin\psi}{\cos\psi + \cos\psi'} \,. \tag{4.156}$$

Let's look at the following factor:

$$G(\psi,\psi') = \frac{-\sin\psi}{\cos\psi + \cos\psi'} \,. \tag{4.157}$$

By using the appropriate trigonometric identities, this factor can be rewritten in the form

$$\begin{aligned} G(\psi,\psi') \;=\; & \frac{1}{4}\left\{ -\cot\left(\frac{\pi-(\psi-\psi')}{4}\right) + \cot\left(\frac{\pi+(\psi-\psi')}{4}\right) \right. \\ & \left. -\cot\left(\frac{\pi-(\psi+\psi')}{4}\right) + \cot\left(\frac{\pi+(\psi+\psi')}{4}\right) \right\} \,. \end{aligned} \tag{4.158}$$

This expression contains terms which indicate a sum of "difference currents" on a flat plate, which is what one obtains using physical optics. Note the negative signs associated with two of the cotangent terms. If the fringe current (the correction) is added to the PO result, we obtain the GTD result. This can be accomplished by replacing the negative cotangent terms with plus signs. Therefore the modified expression is

$$\begin{aligned} G(\psi,\psi') \;=\; & \frac{1}{4}\left\{ \cot\left(\frac{\pi-(\psi-\psi')}{4}\right) + \cot\left(\frac{\pi+(\psi-\psi')}{4}\right) \right. \\ & \left. +\cot\left(\frac{\pi-(\psi+\psi')}{4}\right) + \cot\left(\frac{\pi+(\psi+\psi')}{4}\right) \right\} \,. \end{aligned} \tag{4.159}$$

If the edge (wedge angle parameter $n = 2$) is opened up to form a wedge, the cotangent terms are again modified such that

$$\begin{aligned} G(\psi,\psi') \;=\; & \frac{1}{2n}\left\{ \cot\left(\frac{\pi-(\psi-\psi')}{2n}\right) + \cot\left(\frac{\pi+(\psi-\psi')}{2n}\right) \right. \\ & \left. +\cot\left(\frac{\pi-(\psi+\psi')}{2n}\right) + \cot\left(\frac{\pi+(\psi+\psi')}{2n}\right) \right\} \,. \end{aligned} \tag{4.160}$$

Note that this does not affect the result in the specular region, since it is relatively insensitive to the wedge angle there. If only the outer curved surface information is retained, one obtains

$$G(\psi,\psi') = \frac{1}{2n}\left\{\cot\left(\frac{\pi-(\psi-\psi')}{2n}\right)+\cot\left(\frac{\pi-(\psi+\psi')}{2n}\right)\right\}. \tag{4.161}$$

The dominant term is the reflection boundary term, so

$$G(\psi,\psi') \approx \frac{1}{2n}\cot\left(\frac{\pi-(\psi+\psi')}{2n}\right). \tag{4.162}$$

The PO-type diffraction coefficient after these modifications is

$$D_{s,h}^{ro\mp} = R_{s,h}\frac{-e^{-j\frac{\pi}{4}}}{\sqrt{2\pi k}}\frac{1}{2n}\cot\left(\frac{\pi-(\psi+\psi')}{2n}\right)\mathbf{T}(\pm jXa_e). \tag{4.163}$$

Converting the angle ψ, which is measured from the curved surface, to the angle Φ, which is measured from the endcap face, gives

$$D_{s,h}^{rn\mp} = R_{s,h}\frac{-e^{-j\frac{\pi}{4}}}{\sqrt{2\pi k}}\frac{1}{2n}\cot\left(\frac{\pi+(\Phi+\Phi')}{2n}\right)\mathbf{T}(\pm jXa_e). \tag{4.164}$$

The expression is made three-dimensional again by inserting the factor $\sin\beta_0$. The modified PO-type diffraction coefficient is

$$D_{s,h}^{rn\mp} = R_{s,h}\frac{-e^{-j\frac{\pi}{4}}}{2n\sqrt{2\pi k}\sin\beta_0}\cot\left(\frac{\pi+(\Phi+\Phi')}{2n}\right)\mathbf{T}(\pm jXa_e). \tag{4.165}$$

Now we will make another change to the equivalent-line-current solution. The reflection caustic distance, ρ_1^r, is only valid at the specular angle. We will replace this with the caustic distance for the diffracted ray, ρ^d, which will give the correct spreading of the rays. (At the specular angle, $\rho_1^r = \rho^d$.)

To summarize, we make the following substitutions in the equivalent-line-current expression:

$$\frac{\sin\beta}{\cos\beta+\cos\beta'} \Longrightarrow \mp\frac{-1}{2n\sin\beta_0}\cot\left(\frac{\pi+(\Phi+\Phi')}{2n}\right) \tag{4.166}$$

and

$$\rho_1^r \Longrightarrow \rho^d \,. \tag{4.167}$$

This converts the PO-type result to a UTD-type result. The modified equivalent-line-current expression is

$$\begin{aligned} \vec{E}^r \cdot \hat{e}^r_{\perp,\parallel} &= E^i_{\perp,\parallel}(Q_1) D^{rn-}_{s,h}(Q_1) \sqrt{\rho^d(Q_1)} \frac{e^{-jks_1}}{s_1} \\ &+ E^i_{\perp,\parallel}(Q_2) D^{rn+}_{s,h}(Q_2) \sqrt{\rho^d(Q_2)} \frac{e^{-jks_2}}{s_2} \end{aligned} \tag{4.168}$$

where

$$D^{rn-}_{s,h} = R_{s,h} \frac{-e^{-j\frac{\pi}{4}}}{2n\sqrt{2\pi k}\sin\beta_0} \cot\left(\frac{\pi + (\Phi + \Phi')}{2n}\right) \mathbf{T}(+jXa_e) \tag{4.169}$$

$$D^{rn+}_{s,h} = R_{s,h} \frac{-e^{-j\frac{\pi}{4}}}{2n\sqrt{2\pi k}\sin\beta_0} \cot\left(\frac{\pi + (\Phi + \Phi')}{2n}\right) \mathbf{T}(-jXa_e) \tag{4.170}$$

and

$$\begin{aligned} X &= k\cot\alpha_c[\tan^2\alpha_c(\cos^2 v + \varepsilon_c^2 \sin v) + 1]^{\frac{1}{2}} \\ &\cdot \sin\beta_0 \cos\left(\frac{\Phi + \Phi'}{2}\right)\left[2\cos\left(\frac{2n\pi - (\Phi + \Phi')}{2}\right)\right] . \end{aligned} \tag{4.171}$$

Note that Equation (4.169) without the transition function is the far-field n-face RB term of the edge diffraction coefficient given in Equation (2.13).

Figure 29 shows the curved surface RB portion of the diffraction-point method solution, and the equivalent-line-current solution. The equivalent-line-current solution provides a good result in the specular region which includes the main beam and first sidelobe. Figure 30 compares the field radiated by the equivalent line currents with the field radiated by the modified equivalent line currents. Note the good agreement in the main beam and first sidelobe.

The modified equivalent-line-current result using different transition functions is shown in Figure 31. Note that for observation points above the surface, where

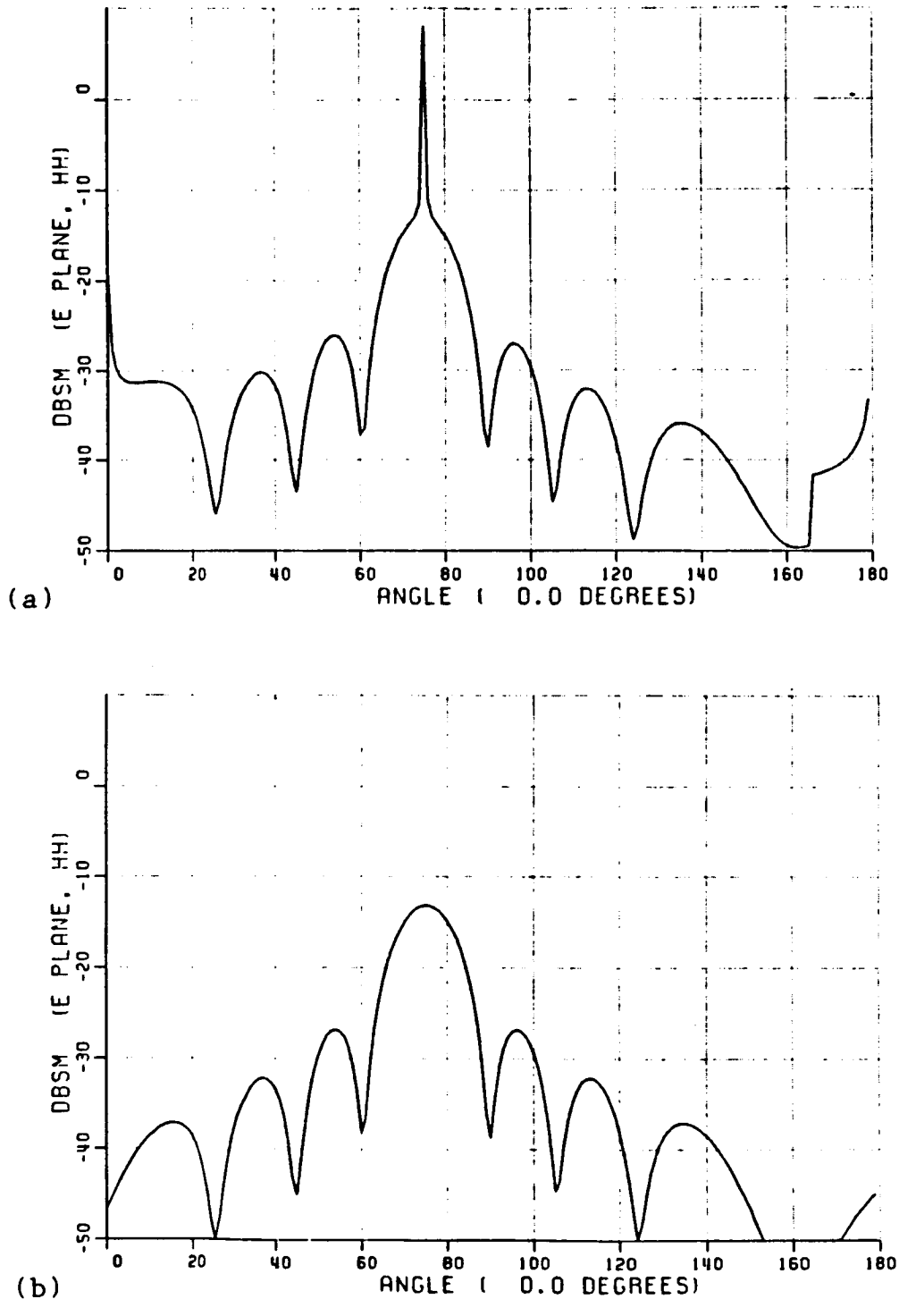

Figure 29: Backscatter pattern for a 15° cone frustum using (a) RB portion of the diffraction-point method solution, and (b) equivalent-line-current solution.

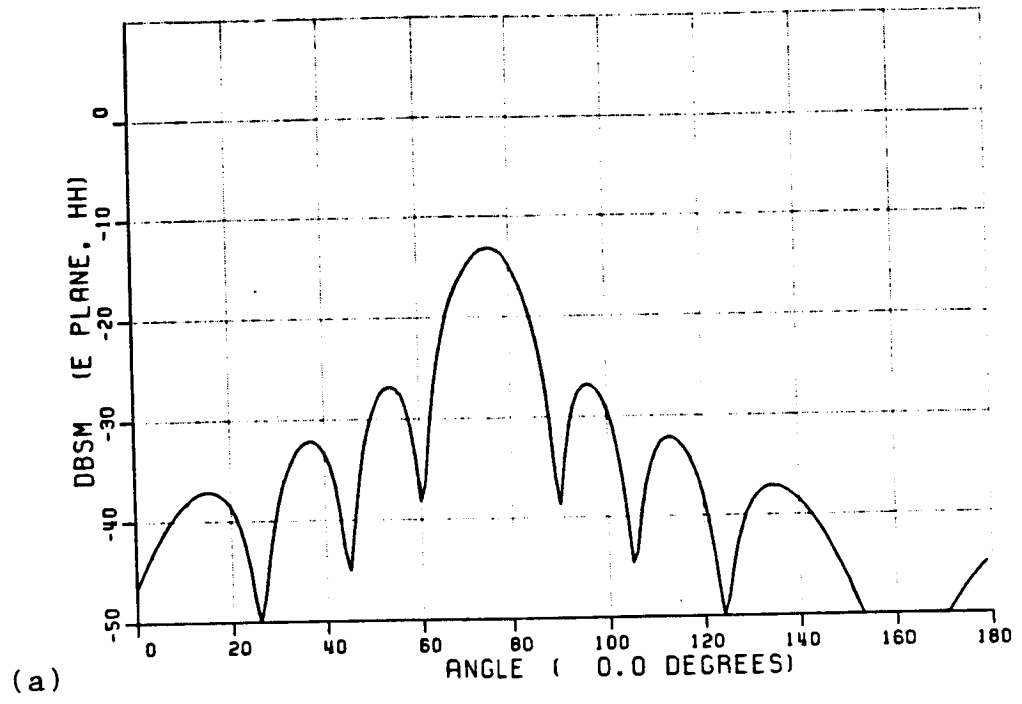

(a)

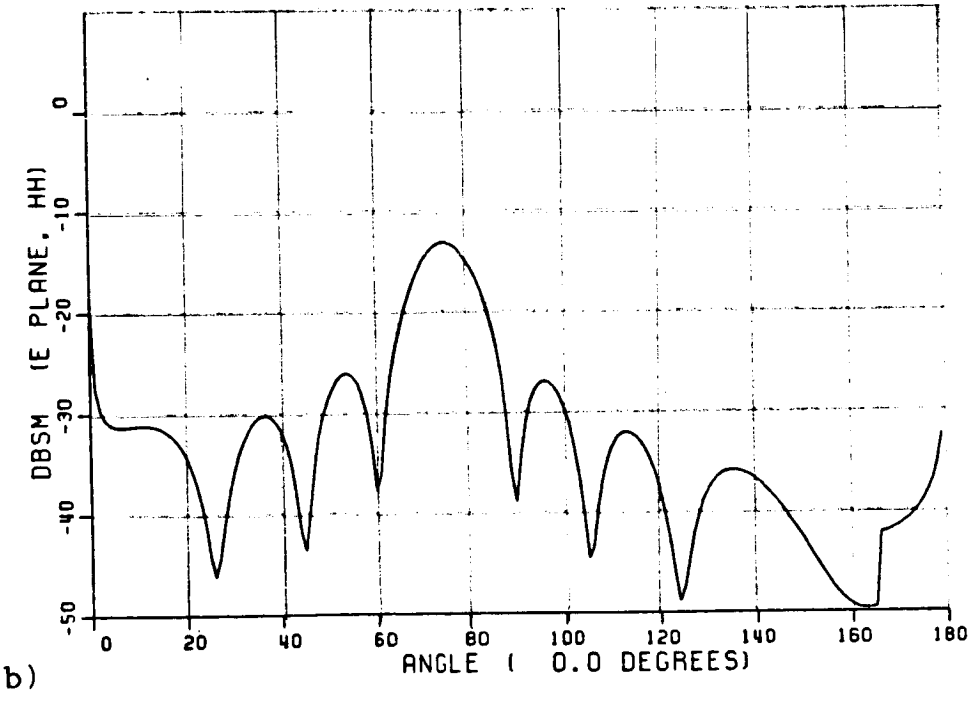

(b)

Figure 30: Backscatter pattern for a 15° cone frustum using (a) equivalent-line-current solution, and (b) modified equivalent-line-current solution.

C-2

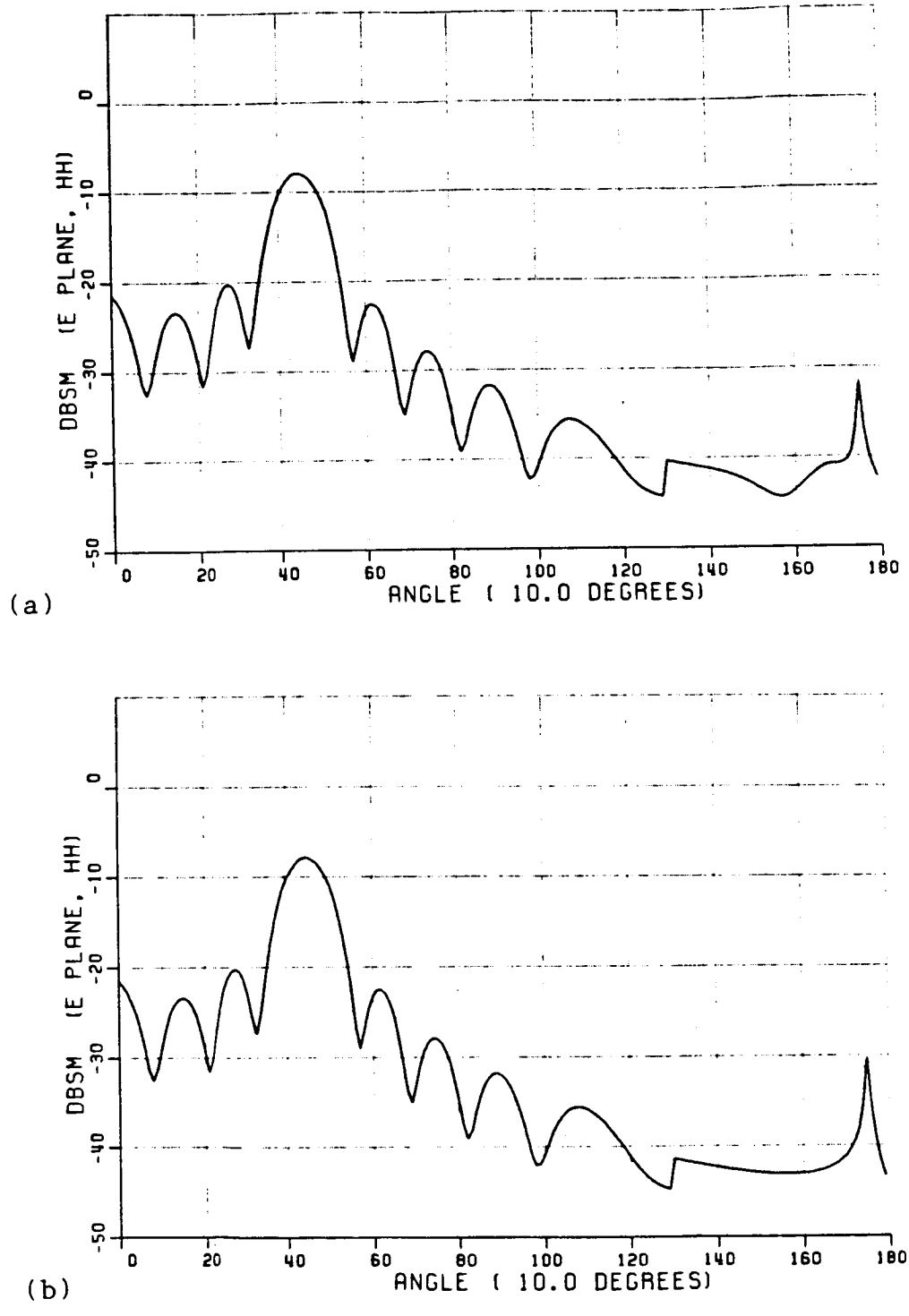

Figure 31: Bistatic 10° scatter pattern for a 40° cone frustum using (a) modified equivalent-line-current solution with $\mathbf{T}_1$, and (b) modified equivalent-line-current solution with $\mathbf{T}_2$.

both edges are present, the pattern is identical. However, below the surface (angles greater than 130 degrees), where only one edge contributes to the field, the pattern is different. This difference is due to the different natures of the transition functions used (see Figures 26 and 27). The transition function $\mathbf{T}_1$ oscillates and dampens slowly to 1 outside the specular region, while the function $\mathbf{T}_2$ goes to 1 rather quickly. In the modified equivalent-line-current solution, when both points on the edge contribute to the field, the same result is obtained, but when only one point is present the differences become apparent.

Which transition function should we use? For a finite cone frustum, we can use either $\mathbf{T}_1$ or $\mathbf{T}_2$. The small differences in the scattered field below the surface can be neglected, except at low frequencies where $\mathbf{T}_2$ should be used (since the value of the function argument remains small). The transition region of $\mathbf{T}_2$ is much narrower than $\mathbf{T}_1$. Also for a semi-infinite cone frustum, $\mathbf{T}_2$ should be used, since without the other edge, we would see a oscillatory nature if $\mathbf{T}_1$ was used. Overall, theoretically speaking, $\mathbf{T}_2$ produces a better result—it provides a more "UTD-type" solution. However, from a practical standpoint, $\mathbf{T}_1$ is better for calculations on the computer, since we do not have to deal with an infinity when the argument becomes zero.

4.4.9 The Diffraction-Point Method Solution with Equivalent-Line-Current Correction

By replacing the curved-surface reflection boundary term of the original GTD diffraction coefficient with Equation (4.169) from the modified equivalent-line-current solution, we obtain a new diffraction coefficient. The new diffraction coefficient is

$$\overline{\overline{D}}^{\mp} = -\hat{\beta}_0' \hat{\beta}_0 D_s^{\mp} - \hat{\Phi}' \hat{\Phi} D_h^{\mp}$$

where

$$D_{s,h}^{\mp} = \frac{-e^{-j\frac{\pi}{4}}}{2n\sqrt{2\pi k}\sin\beta_0}\left\{\cot\left(\frac{\pi+(\Phi-\Phi')}{2n}\right)+\cot\left(\frac{\pi-(\Phi-\Phi')}{2n}\right)+\right.$$

$$\left.+R_{s,h}\left[\cot\left(\frac{\pi+(\Phi+\Phi')}{2n}\right)\mathbf{T}(\pm jXa_e)+\cot\left(\frac{\pi-(\Phi+\Phi')}{2n}\right)\right]\right\} \tag{4.172}$$

$$R_{s,h} = \mp 1\,. \tag{4.173}$$

And the transition function is either

$$\mathbf{T}(z) = \mathbf{T}_1(z) = \frac{2}{3}z\mathbf{M}(1,2.5,-z) \tag{4.174}$$

or

$$\mathbf{T}(z) = \mathbf{T}_2(z) = -z\mathbf{U}(1,2.5,-z) \tag{4.175}$$

where

$$\mathbf{T}(\text{outside specular region}) \rightarrow 1\,. \tag{4.176}$$

The diffraction-point method solution with the equivalent-line-current correction for the curved-surface specular region is

$$\vec{E}^s \approx \vec{E}^d_{total} = \vec{E}^d_1 + \vec{E}^d_2 + \vec{E}^d_3 + \vec{E}^d_4 \tag{4.177}$$

where

$$\vec{E}^d_1 = \vec{E}^i(Q_1)\cdot\overline{\overline{D}}^{+}(Q_1)\sqrt{\rho^d(Q_1)}e^{jkr\vec{1}\cdot\hat{r}}\frac{e^{-jkr}}{r} \tag{4.178}$$

$$\vec{E}^d_2 = \vec{E}^i(Q_2)\cdot\overline{\overline{D}}^{-}(Q_2)\sqrt{\rho^d(Q_2)}e^{jkr\vec{2}\cdot\hat{r}}\frac{e^{-jkr}}{r} \tag{4.179}$$

$$\vec{E}^d_3 = \vec{E}^i(Q_3)\cdot\overline{\overline{D}}^{+}(Q_3)\sqrt{\rho^d(Q_3)}e^{jkr\vec{3}\cdot\hat{r}}\frac{e^{-jkr}}{r} \tag{4.180}$$

$$\vec{E}^d_4 = \vec{E}^i(Q_4)\cdot\overline{\overline{D}}^{-}(Q_4)\sqrt{\rho^d(Q_4)}e^{jkr\vec{4}\cdot\hat{r}}\frac{e^{-jkr}}{r}\,. \tag{4.181}$$

Note how the original diffraction-point method form of the expression is preserved by the use of the transition function in the diffraction coefficient.

Figures 32, 33, 34, and 35 demonstrate for various cone angles how the transition function can correct the original diffraction-point method solution in the specular region. Note that it is a uniform solution. The diffraction-point method solution remains unaffected outside the specular region. Additional information on the calculated patterns is contained in the following section. One item that is worth noting is the relative CPU times required to generate the patterns. The corrected diffraction-point method solution takes longer to calculate, but it is roughly of the same order of magnitude. For Figure 35, 0.04 minutes versus 0.07 minutes on a VAX 11/780 computer with a floating point accelerator.

4.5 Background Information on Calculated Patterns.

This section contains information on the patterns for the scattered field calculated in this chapter. The patterns were generated using a VAX 11/780 computer. All patterns are for a circular cone frustum in the principal plane for the horizontal (hard) polarization case only (see Section 3.4.1). Only one polarization is studied, since the plots in this section are for demonstration purposes only. Actual comparisons with measurments and the moment method calculations will be shown in Chapters 6 and 7.

The vertical axis of the plot is the radar cross section in decibels above a square meter. The horizonal axis is the angle θ (azimuth) for the receiver position in the principal plane (see Figure 10). Points were calculated every one degree. The following table lists information about the cone frustum dimensions, frequency, bistatic angle, and CPU times for each plot. The symbols used in the Table 4.1

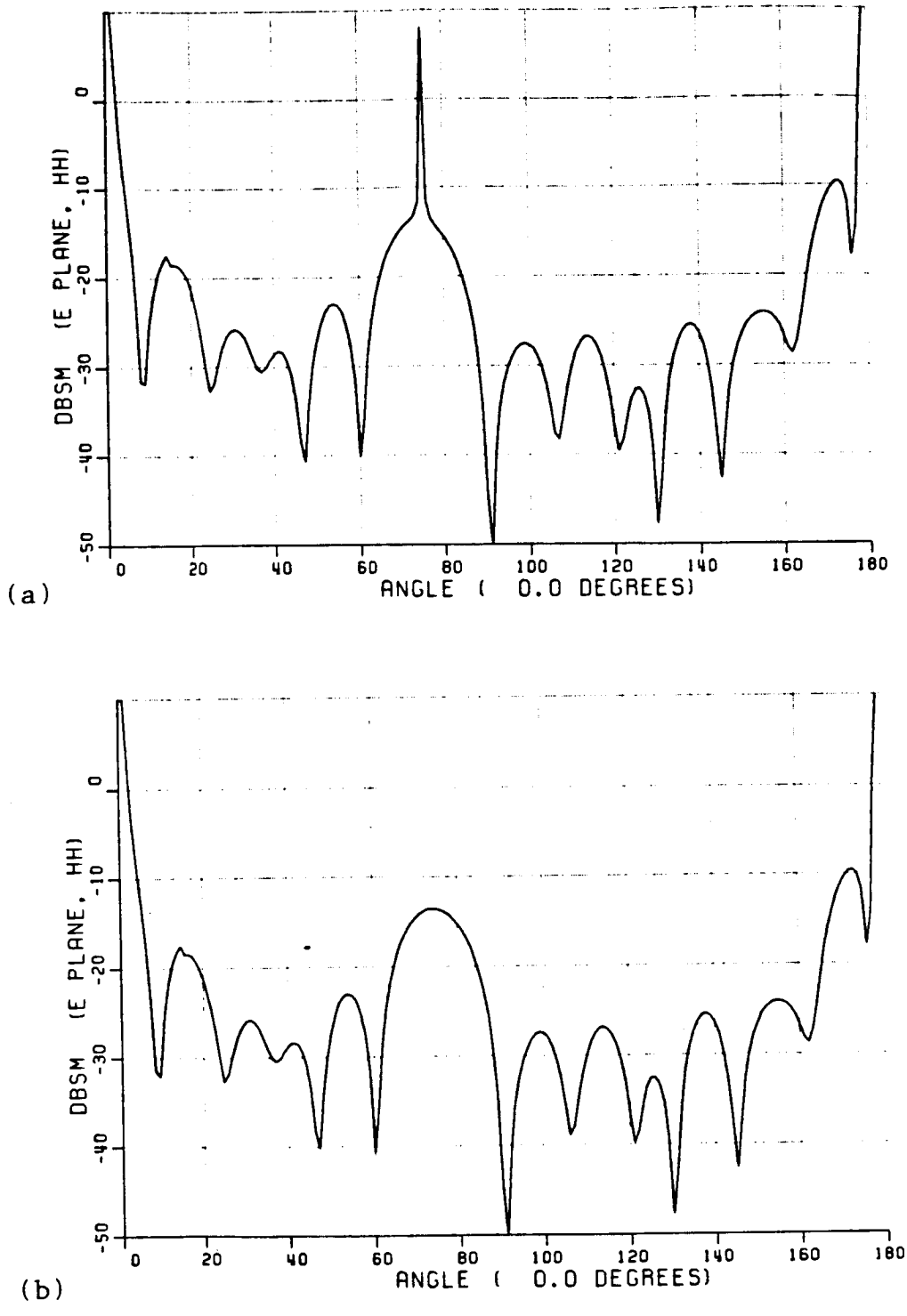

Figure 32: Backscatter from a 15° cone frustum using (a) the diffraction-point method, and (b) the diffraction-point method with equivalent-line-current correction.

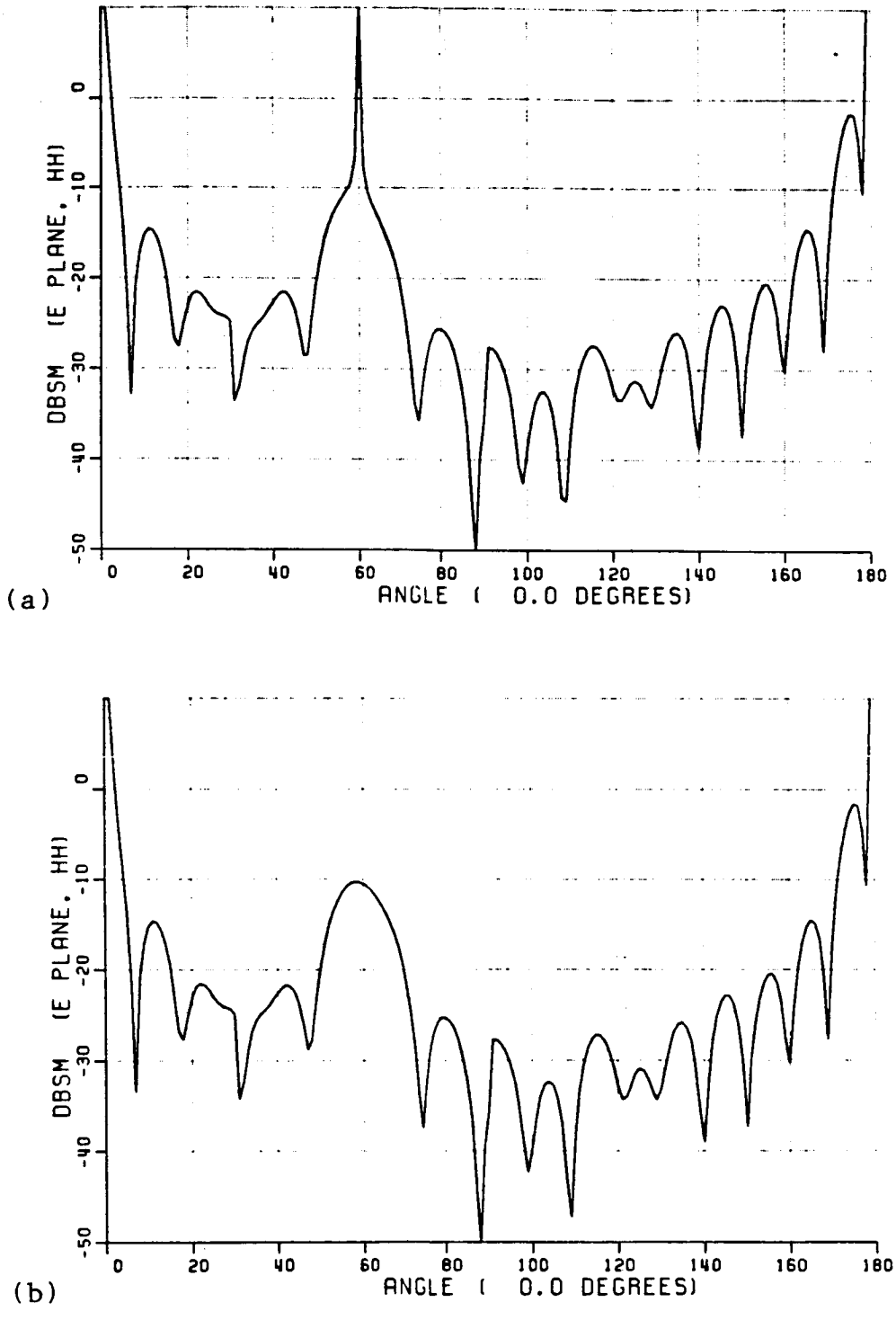

Figure 33: Backscatter from a 30° cone frustum using (a) the diffraction-point method, and (b) the diffraction-point method with equivalent-line-current correction.

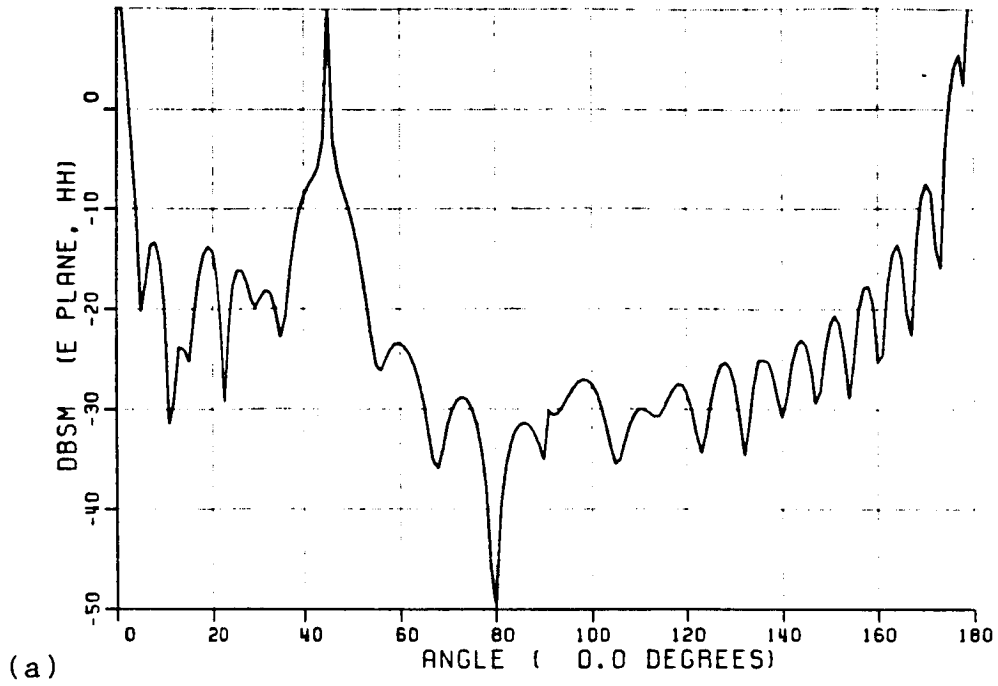

(a)

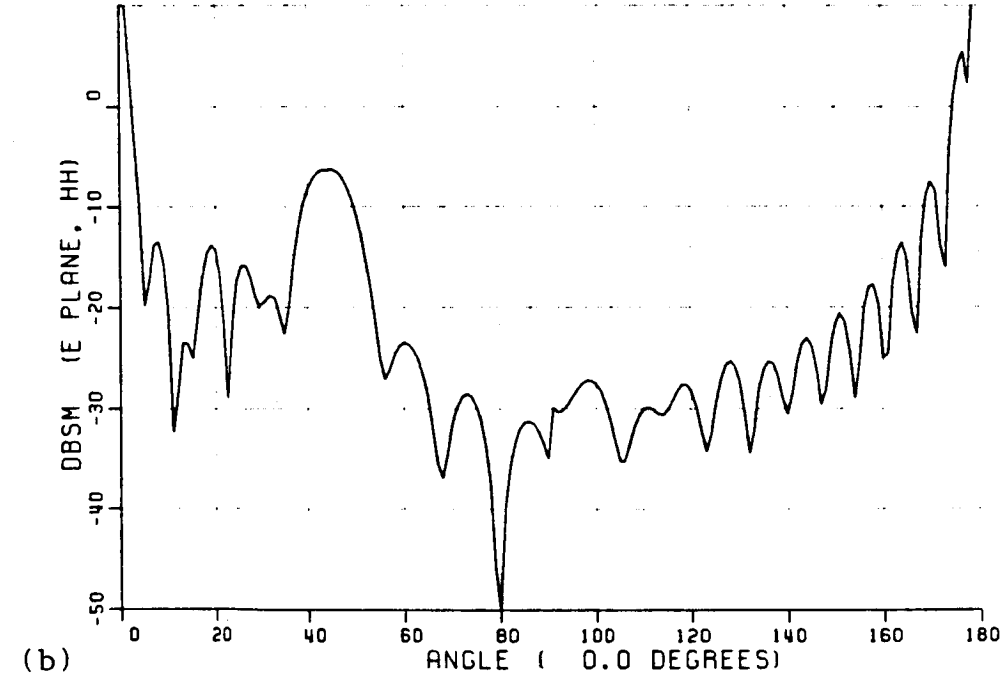

(b)

Figure 34: Backscatter from a 45° cone frustum using (a) the diffraction-point method, and (b) the diffraction-point method with equivalent-line-current correction.

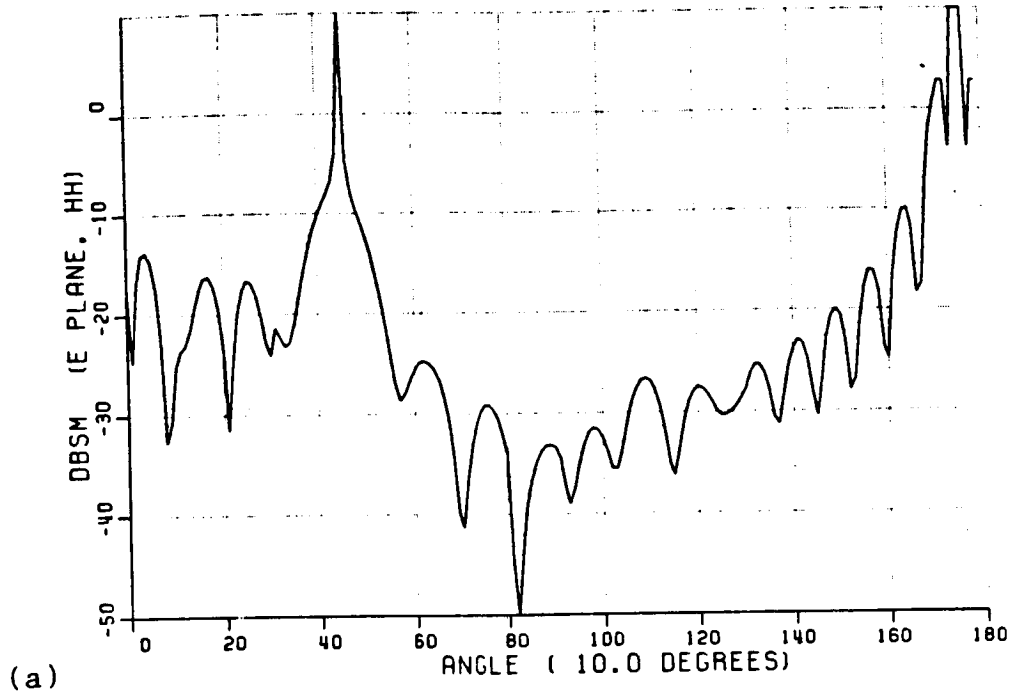

(a)

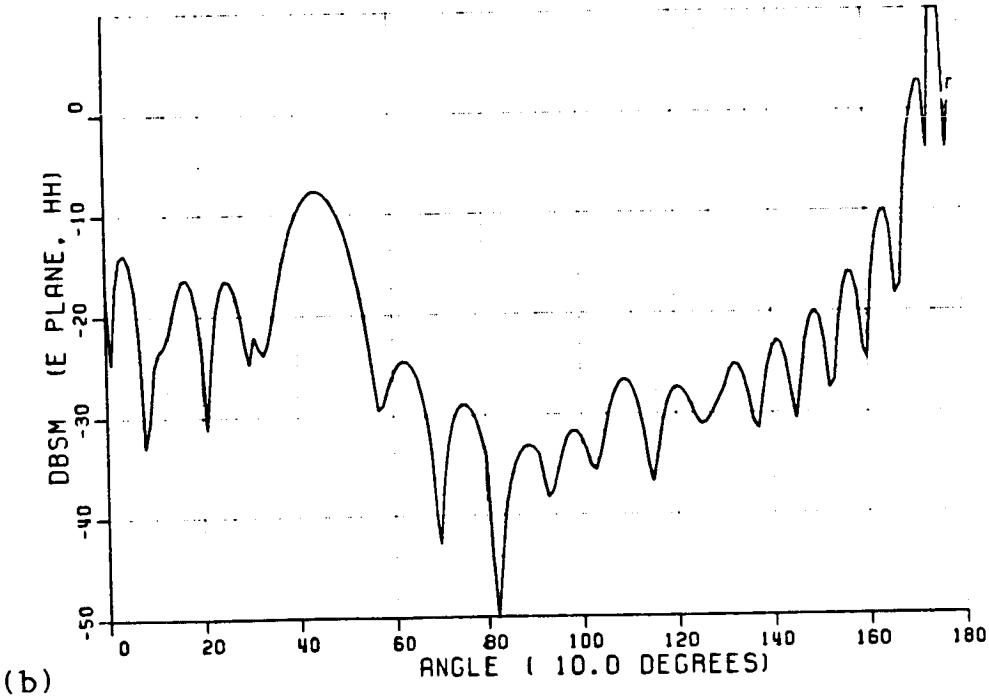

(b)

Figure 35: Bistatic 10° scatter from a 40° cone frustum using (a) the diffraction-point method, and (b) the diffraction-point method with equivalent-line-current correction.

refer to the following:

$$
\begin{aligned}
f &= \text{frequency (GHz)} \\
h &= \text{cone frustum height (inches)} \\
a_1, a_2 &= \text{cone frustum radii (inches)} \\
\alpha_c &= \text{cone angle (degress)} \\
\beta_s &= \text{bistatic angle (degrees)} \\
T_{cpu} &= \text{CPU time required (minutes)}
\end{aligned}
$$

Table 4.1: Table of dimensions, angles, and CPU times for calculated patterns shown in Chapter 4.

Figure	f	h	a_1	a_2	α_c	β_s	T_{cpu}
17(a)	6.05	3.75	1.00	4.15	40	10	0.04
17(b)	6.05	3.75	1.00	4.15	40	10	0.05
29(a)	6.05	3.75	1.00	2.00	15	0	0.04
29(b)	6.05	3.75	1.00	2.00	15	0	0.07
30(a)	6.05	3.75	1.00	2.00	15	0	0.07
30(b)	6.05	3.75	1.00	2.00	15	0	0.07
31(a)	6.05	3.75	1.00	4.15	40	10	0.06
31(b)	6.05	3.75	1.00	4.15	40	10	0.06
32(a)	6.05	3.75	1.00	2.00	15	0	0.04
32(b)	6.05	3.75	1.00	2.00	15	0	0.07
33(a)	6.05	3.75	1.00	3.17	30	0	0.04
33(b)	6.05	3.75	1.00	3.17	30	0	0.08
34(a)	6.05	3.75	1.00	4.75	45	0	0.04
34(b)	6.05	3.75	1.00	4.75	45	0	0.07
35(a)	6.05	3.75	1.00	4.15	40	10	0.04
35(b)	6.05	3.75	1.00	4.15	40	10	0.07

CHAPTER V

Rim Caustic Corrections

5.1 Introduction.

In the last chapter, we developed a uniform correction to the diffraction-point method solution for the frustum's curved-surface specular region. One can easily appreciate the use of a transition function to preserve the original form of the diffraction-point method solution. Numerical integrations are avoided, and the transition functions have large argument forms which greatly reduce calculation times.

In this chapter we will continue in the same tradition—to develop a uniform correction using transition functions for the rim-caustic regions. Fortunately, a great deal of the work on this problem has already been done. Ryan and Peters [7] had developed a solution in the rim-caustic regions based on the fields radiated by equivalent edge currents on the rim. Since this result goes to the diffraction-point solution outside the caustic region, it is a uniform solution. Recently Chiang [1] extended the work of Ryan and Peters by using equivalent currents that use the "stripping concept" [15,8] in addition to using small-argument approximations in the radiation integral. Chiang's solution provides an accurate result in the rim-caustic regions that are associated with a specular or forward-scatter direction of the endcaps. This solution is called the "Bessel-Struve function extension". It, also, is a uniform solution.

Uniform solutions for rim caustics are available. However, in the literature, the solutions are not often expressed in the transition function form that we desire. Also the partial illumination and partial observation of a rim, as in the case of the cone frustum, is not considered. These details will be investigated in this chapter. First we will look at the equivalent-edge-current solution of Ryan and Peters.

5.2 Ryan/Peters Equivalent-Edge-Current Solution

The formulation of the equivalent edge currents is similar to the concept used in the last chapter. It will not be discussed here, since much is available in the present literature. Some suggested references are [14] and [7]. The equivalent edge currents used by Ryan and Peters are

$$\underline{I}^e = \frac{2jG^e}{\eta k \sin\beta_0}(\hat{e}\cdot\vec{E}^i(0))e^{jk\vec{r}_e\cdot\hat{r}'} \tag{5.182}$$

$$\underline{I}^m = \frac{2jG^e}{k \sin\beta_0}\eta(\hat{e}\cdot\vec{H}^i(0))e^{jk\vec{r}_e\cdot\hat{r}'} \tag{5.183}$$

where

$$G^e(\Phi,\Phi') = -\frac{1}{2n}(A-B) \tag{5.184}$$

$$G^m(\Phi,\Phi') = -\frac{1}{2n}(A+B) \tag{5.185}$$

and

$$A(\Phi,\Phi') = \cot\left(\frac{\pi+(\Phi-\Phi')}{2n}\right)+\cot\left(\frac{\pi-(\Phi-\Phi')}{2n}\right) \tag{5.186}$$

$$B(\Phi,\Phi') = \cot\left(\frac{\pi+(\Phi+\Phi')}{2n}\right)+\cot\left(\frac{\pi-(\Phi+\Phi')}{2n}\right). \tag{5.187}$$

The equivalent electric current is $\underline{I}^e$ and the equivalent magnetic current is $\underline{I}^m$ (see Figure 36). These currents are distributed on the illuminated edges of the

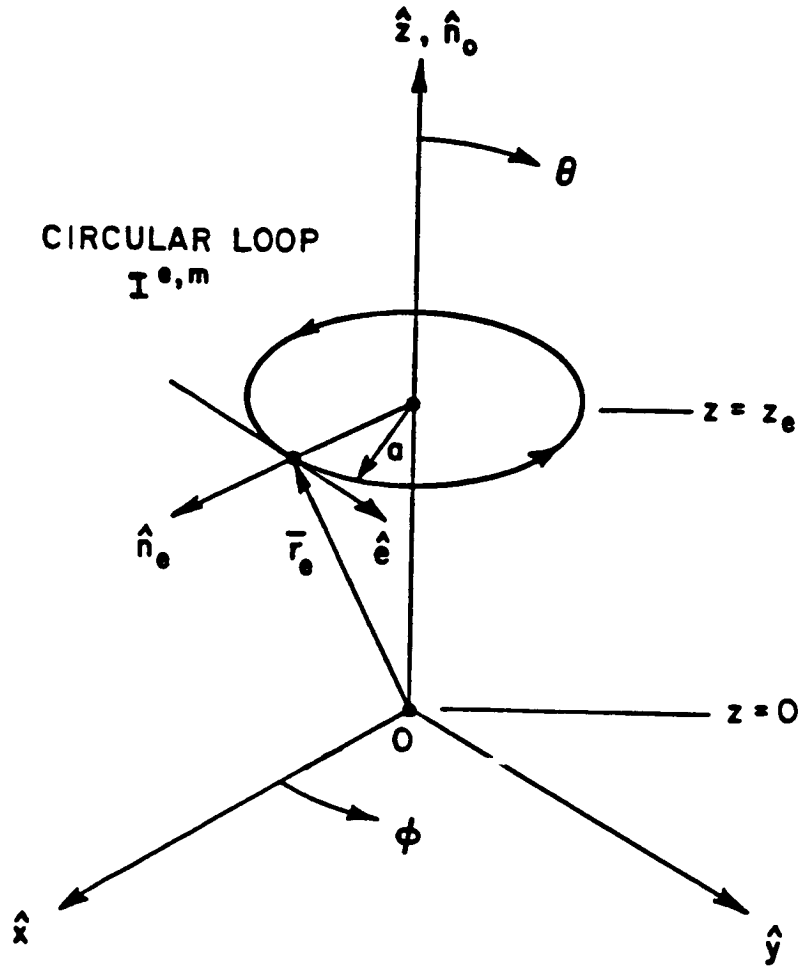

Figure 36: Rim geometry.

cone frustum and the radiated fields are evaluated. For simplicity, we will restict ourselves to a circular cone frustum (of radius a) and observation in the principal plane. The far-zone radiated fields due to the electric and magnetic equivalent-edge-current loops are

$$E_\theta^e = \frac{a\cos\theta}{2\pi}\frac{e^{-jkr}}{r}\int_0^{2\pi}\frac{G^e}{\sin\beta_0}(\hat{e}\cdot\vec{E}^i(0))\sin(\phi-\phi_e)e^{jk\vec{r}_e\cdot(\hat{r}+\hat{r}')}d\phi_e \quad (5.188)$$

$$E_\theta^m = \frac{a\eta}{2\pi}\frac{e^{-jkr}}{r}\int_0^{2\pi}\frac{G^m}{\sin\beta_0}(\hat{e}\cdot\vec{H}^i(0))\cos(\phi-\phi_e)e^{jk\vec{r}_e\cdot(\hat{r}+\hat{r}')}d\phi_e \quad (5.189)$$

$$E_\phi^e = \frac{a}{2\pi}\frac{e^{-jkr}}{r}\int_0^{2\pi}\frac{G^e}{\sin\beta_0}(\hat{e}\cdot\vec{E}^i(0))\cos(\phi-\phi_e)e^{jk\vec{r}_e\cdot(\hat{r}+\hat{r}')}d\phi_e \quad (5.190)$$

$$E_\phi^m = -\frac{a\eta\cos\theta}{2\pi}\frac{e^{-jkr}}{r}\int_0^{2\pi}\frac{G^m}{\sin\beta_0}(\hat{e}\cdot\vec{H}^i(0))\sin(\phi-\phi_e)e^{jk\vec{r}_e\cdot(\hat{r}+\hat{r}')}d\phi_e\,. \quad (5.191)$$

The diffracted field is the sum of the fields radiated from both electric and magnetic equivalent currents, such that

$$\vec{E}_{rim}^d = \hat{\theta}E_\theta + \hat{\phi}E_\phi \quad (5.192)$$

$$E_\phi = E_\phi^e + E_\phi^m \quad (5.193)$$

$$E_\theta = E_\theta^e + E_\theta^m\,. \quad (5.194)$$

To simplify the the integration in (5.188)–(5.191), Ryan and Peters used the approximation that the diffraction coefficients remained relatively constant with respect to the variable of integration, so that

$$\frac{G^{e,m}}{\sin\beta_0} \approx \text{constant in } \phi_e. \quad (5.195)$$

Let

$$\psi_e = ka\hat{n}_e(\phi_e)\cdot(\hat{r}+\hat{r}') \quad (5.196)$$

$$= ka[\sin\theta'\cos(\phi' - \phi_e) + \sin\theta\cos(\phi - \phi_e)] \quad (5.197)$$

$$\gamma_e = kz_e\hat{z}\cdot(\hat{r} + \hat{r}')\,. \quad (5.198)$$

Using the previously mentioned approximation and the fact that

$$\int_0^{2\pi} \sin\phi_e \cos\phi_e e^{j\psi_e} d\phi_e = 0 \quad (5.199)$$

the expressions for the radiated fields become

$$E_\phi = \frac{a}{2\pi}\frac{e^{j\gamma_e}}{\sin\beta_0}\frac{e^{-jkr}}{r} \quad E_\phi^i\left\{-G^e\int_0^{2\pi}\cos^2\phi_e e^{j\psi_e}d\phi_e + G^m\cos\theta\cos\theta'\int_0^{2\pi}\sin^2\phi_e e^{j\psi_e}d\phi_e\right\} \quad (5.200)$$

$$E_\theta = \frac{a}{2\pi}\frac{e^{j\gamma_e}}{\sin\beta_0}\frac{e^{-jkr}}{r} \quad E_\theta^i\left\{G^e\cos\theta\cos\theta'\int_0^{2\pi}\sin^2\phi_e e^{j\psi_e}d\phi_e + G^m\int_0^{2\pi}\cos^2\phi_e e^{j\psi_e}d\phi_e\right\} \quad (5.201)$$

where

$$\psi_e = U\cos\phi_e\,. \quad (5.202)$$

Let the following integrals be defined by:

$$F_1(U) = \int_0^{2\pi}\cos^2\phi_e e^{j\psi_e}d\phi_e \quad (5.203)$$

$$f_1(U) = \int_{-\frac{\pi}{2}}^{\frac{\pi}{2}}\cos^2\phi_e e^{j\psi_e}d\phi_e \quad (5.204)$$

$$f_1^*(U) = \int_{\frac{\pi}{2}}^{\frac{3\pi}{2}}\cos^2\phi_e e^{j\psi_e}d\phi_e \quad (5.205)$$

$$F_2(U) = \cos\theta\cos\theta'\int_0^{2\pi}\sin^2\phi_e e^{j\psi_e}d\phi_e \quad (5.206)$$

$$f_2(U) = \cos\theta\cos\theta' \int_{-\frac{\pi}{2}}^{\frac{\pi}{2}} \sin^2\phi_e e^{j\psi_e} d\phi_e \tag{5.207}$$

$$f_2^*(U) = \cos\theta\cos\theta' \int_{\frac{\pi}{2}}^{\frac{3\pi}{2}} \sin^2\phi_e e^{j\psi_e} d\phi_e \tag{5.208}$$

These integrals can be evaluated in closed form as follows:

$$f_1(U) = \pi\left[\left(J_0(U) - \frac{J_1(U)}{U}\right) + j\left(\mathbf{H}_0(U) - \frac{\mathbf{H}_1(U)}{U}\right)\right] \tag{5.209}$$

$$f_1^*(U) = \pi\left[\left(J_0(U) - \frac{J_1(U)}{U}\right) - j\left(\mathbf{H}_0(U) - \frac{\mathbf{H}_1(U)}{U}\right)\right] \tag{5.210}$$

$$f_2(U) = \cos\theta\cos\theta'\pi\left(\frac{J_1(U)}{U} + j\frac{\mathbf{H}_1(U)}{U}\right) \tag{5.211}$$

$$f_2^*(U) = \cos\theta\cos\theta'\pi\left(\frac{J_1(U)}{U} - j\frac{\mathbf{H}_1(U)}{U}\right) . \tag{5.212}$$

The expressions for the radiated fields are

$$E_\phi = \frac{a}{2\pi\sin\beta_0}\frac{e^{j\gamma_e}}{r}\frac{e^{-jkr}}{r}E_\phi^i\{-(A-B)F_1 + (A+B)F_2\} \tag{5.213}$$

$$E_\theta = \frac{a}{2\pi\sin\beta_0}\frac{e^{j\gamma_e}}{r}\frac{e^{-jkr}}{r}E_\theta^i\{(A-B)F_2 + (A+B)F_1\} . \tag{5.214}$$

The above can be rearranged into

$$E_\phi = -\frac{a}{2\pi \sin\beta_0}\frac{e^{j\gamma_e}}{}\frac{e^{-jkr}}{r}E_\phi^i\{A(F_1-F_2)-B(F_1+F_2)\} \quad (5.215)$$

$$E_\theta = \frac{a}{2\pi \sin\beta_0}\frac{e^{j\gamma_e}}{}\frac{e^{-jkr}}{r}E_\theta^i\{A(F_1+F_2)+B(F_1-F_2)\}\ . \quad (5.216)$$

Breaking the integrals apart into

$$F_1(U) = f_1(U)+f_1^*(U) \quad (5.217)$$

$$F_2(U) = f_2(U)+f_2^*(U) \quad (5.218)$$

and further manipulation gives

$$\begin{aligned} E_\phi = & -\frac{a}{2\pi \sin\beta_0}\frac{e^{j\gamma_e}}{}\frac{e^{-jkr}}{r}E_\phi^i\{A(f_1-f_2)-B(f_1+f_2) \\ & +A(f_1^*-f_2^*)-B(f_1^*+f_2^*)\} \end{aligned} \quad (5.219)$$

$$\begin{aligned} E_\theta = & \frac{a}{2\pi \sin\beta_0}\frac{e^{j\gamma_e}}{}\frac{e^{-jkr}}{r}E_\theta^i\{A(f_1+f_2)+B(f_1-f_2) \\ & +A(f_1^*+f_2^*)+B(f_1^*-f_2^*)\}\ . \end{aligned} \quad (5.220)$$

Now let us associate a half-rim integral with the points at $\phi_e = 0, \pi$ which are the stationary points for large ψ_e. (These are the diffraction points on the rim for the principal plane. See Section 3.4.2.) In the above equation, the field contributions from the half-rim associated with $\phi_e = 0$ are

$$E_{1\phi} = -\frac{a}{2\pi \sin\beta_0}\frac{e^{j\gamma_e}}{}\frac{e^{-jkr}}{r}E_\phi^i\{A(f_1-f_2)-B(f_1+f_2)\} \quad (5.221)$$

$$E_{1\theta} = \frac{a}{2\pi}\frac{e^{j\gamma_e}}{\sin\beta_0}\frac{e^{-jkr}}{r}E_\theta^i\{A(f_1+f_2)+B(f_1-f_2)\} \tag{5.222}$$

$$\vec{E}_1^d = \hat{\phi}E_{1\phi}+\hat{\theta}E_{1\theta}\,. \tag{5.223}$$

Comparing this with the expression for the edge-diffracted field from a point on the rim,

$$\vec{E}_e^d = \vec{E}^i(Q_e)\cdot\overline{\overline{D}}(Q_e)\sqrt{\rho^d(Q_e)}e^{jkr\vec{e}\cdot\hat{r}}\frac{e^{-jkr}}{r} \tag{5.224}$$

we obtain the following new diffraction coefficients:

$$\overline{\overline{D}}(Q_e) = -\hat{\beta}_0{}'\hat{\beta}_0 D_s(Q_e) - \hat{\Phi}'\hat{\Phi}D_h(Q_e)$$

$$D_s(Q_e) = \frac{-e^{-j\frac{\pi}{4}}}{2n\sqrt{2\pi k}\sin\beta_0}(A\mathbf{T}_{e1}(U)-B\mathbf{T}_{e2}(U)) \tag{5.225}$$

$$D_h(Q_e) = \frac{-e^{-j\frac{\pi}{4}}}{2n\sqrt{2\pi k}\sin\beta_0}(A\mathbf{T}_{e2}(U)+B\mathbf{T}_{e1}(U)) \tag{5.226}$$

where

$$\mathbf{T}_{e1}(U) = \frac{1}{\pi}(f_1(U)-f_2(U))\sqrt{\frac{\pi U}{2}}e^{-j(U-\frac{\pi}{4})} \tag{5.227}$$

$$\mathbf{T}_{e2}(U) = \frac{1}{\pi}(f_1(U)+f_2(U))\sqrt{\frac{\pi U}{2}}e^{-j(U-\frac{\pi}{4})} \tag{5.228}$$

and

$$U(Q_e) = ka_e\hat{n}_e\cdot(\hat{r}+\hat{r}')\,. \tag{5.229}$$

The functions $\mathbf{T}_{e1}$ and $\mathbf{T}_{e2}$ are the transition functions through the rim caustic region based on the Ryan/Peters equivalent-edge-current solution. The transition functions have small and large argument forms which were obtained using the

series and asymptotic forms of the Bessel and Struve functions, such that

for $|U| \ll 1$

$$\begin{aligned}\mathbf{T}_{e1}(U) &\approx \sqrt{\frac{\pi U}{2}} e^{-j(U-\frac{\pi}{4})} \cdot \\ &\cdot \left\{ \frac{1}{2} \left[1 - \frac{3U^2}{8} + \frac{U^4}{32} - \cos\theta \cos\theta' \left(1 - \frac{U^2}{8} \right) \right] \right. \\ &\left. + j \frac{2U}{3\pi} \left[2 \left(1 - \frac{2U^2}{15} \right) - \cos\theta \cos\theta' \left(1 - \frac{U^2}{15} \right) \right] \right\} \quad (5.230)\end{aligned}$$

$$\begin{aligned}\mathbf{T}_{e2}(U) &\approx \sqrt{\frac{\pi U}{2}} e^{-j(U-\frac{\pi}{4})} \cdot \\ &\cdot \left\{ \frac{1}{2} \left[1 - \frac{3U^2}{8} + \frac{U^4}{32} + \cos\theta \cos\theta' \left(1 - \frac{U^2}{8} \right) \right] \right. \\ &\left. + j \frac{2U}{3\pi} \left[2 \left(1 - \frac{2U^2}{15} \right) + \cos\theta \cos\theta' \left(1 - \frac{U^2}{15} \right) \right] \right\} \quad (5.231)\end{aligned}$$

for $|U| \gg 1$

$$\begin{aligned}\mathbf{T}_{e1}(U) &\sim 1 - \frac{j9}{8U} + \frac{39}{128U^2} - \frac{j45}{1024U^3} \\ &- \cos\theta \cos\theta' \left(-\frac{j}{U} + \frac{3}{8U^2} - \frac{j15}{128U^3} \right) \\ &- \sqrt{\frac{2}{\pi U}} e^{-j(U-\frac{\pi}{4})} \left[\cos\theta \cos\theta' \left(1 + \frac{1}{U^2} \right) + \frac{2}{U^2} \right] \quad (5.232)\end{aligned}$$

$$\begin{aligned}\mathbf{T}_{e2}(U) &\sim 1 - \frac{j9}{8U} + \frac{39}{128U^2} - \frac{j45}{1024U^3} \\ &+ \cos\theta \cos\theta' \left(-\frac{j}{U} + \frac{3}{8U^2} - \frac{j15}{128U^3} \right) \\ &+ \sqrt{\frac{2}{\pi U}} e^{-j(U-\frac{\pi}{4})} \left[\cos\theta \cos\theta' \left(1 + \frac{1}{U^2} \right) - \frac{2}{U^2} \right] \quad (5.233)\end{aligned}$$

The total field radiated by the equivalent edge currents on the rim may be written in the diffraction-point form.

$$\vec{E}^d_{rim} = \vec{E}^d_1 + \vec{E}^d_3 \tag{5.234}$$

where

$$\vec{E}^d_1 = \vec{E}^i(Q_1) \cdot \overline{\overline{D}}(Q_1) \sqrt{\rho^d(Q_1)} e^{jkr\vec{1}\cdot\hat{r}} \frac{e^{-jkr}}{r} \tag{5.235}$$

$$\vec{E}^d_3 = \vec{E}^i(Q_3) \cdot \overline{\overline{D}}(Q_3) \sqrt{\rho^d(Q_3)} e^{jkr\vec{3}\cdot\hat{r}} \frac{e^{-jkr}}{r} . \tag{5.236}$$

Note that Q_1 and Q_3 are the two diffraction points on the rim.

5.3 Bessel-Struve Function Extension

One problem associated with the Ryan/Peters result is that the approximation (5.195) becomes invalid for a rim caustic associated with an endcap's specular or forward-scatter direction. The diffraction coefficients can become infinite in the specular or forward-scatter direction.

It was also discovered that by evaluating the integrals in (5.188)–(5.191) numerically, the result is twice the expected result in the specular rim-caustic regions. The explaination for this is that the reflecting surface is evaluated twice when the integral is performed around the rim from 0 to 2π. To overcome this difficulty, a modified edge vector $\hat{e}^*$ is used. It is defined by

$$\hat{e}^* = \hat{p}(\hat{e} \cdot \hat{p}) \tag{5.237}$$

where

$$\hat{p} = \frac{(\hat{r}' + \hat{r}) \times \hat{n}_o}{|(\hat{r}' + \hat{r}) \times \hat{n}_o|} \tag{5.238}$$

$$\hat{n}_o = \text{normal to the endcap} \tag{5.239}$$

$$\hat{r}' = \text{direction of source, and} \tag{5.240}$$

$$\hat{r} = \text{direction of receiver.} \tag{5.241}$$

By using the modified edge vector, only the perpendicular components (to the plane of incidence) of the equivalent edge currents are considered. This is called the "stripping concept". The equivalent edge currents with this modification are given by

$$I_s^e = \frac{2jG^e}{\eta k \sin\beta_0 \sin\beta_0'}(\hat{e}^* \cdot \vec{E}^i(0))e^{jk\vec{r}_e\cdot\hat{r}'} \tag{5.242}$$

$$I_s^m = \frac{2jG^m}{k \sin\beta_0 \sin\beta_0'}\eta(\hat{e}^* \cdot \vec{H}^i(0))e^{jk\vec{r}_e\cdot\hat{r}'} . \tag{5.243}$$

The modified equivalent-edge-current solution is obtain in the same way as before. To simplify the evaluation of the integral, Chiang used the following small-argument approximations:

$$\theta \approx \theta' - \epsilon \text{ , in the specular region, or} \tag{5.244}$$

$$\theta \approx \pi - \theta' - \epsilon \text{ , in the forward scatter region.} \tag{5.245}$$

This resulted in

$$\frac{G^{e,m}}{\sin\beta_0 \sin\beta_0'} \approx \frac{1}{\epsilon \cos\phi_e} \tag{5.246}$$

and the integral

$$F_0(U) = \int_0^{2\pi} \cos\phi_e e^{jU\cos\phi_e} d\phi_e \tag{5.247}$$

which can be evaluated by using

$$f_0(U) = \int_{-\frac{\pi}{2}}^{\frac{\pi}{2}} \cos\phi_e e^{jU\cos\phi_e} d\phi_e \tag{5.248}$$

$$= \pi\left[\frac{2}{\pi} - \mathbf{H}_1(U) + jJ_1(U)\right] \tag{5.249}$$

$$f_0^*(U) = \int_{\frac{\pi}{2}}^{\frac{3\pi}{2}} \cos\phi_e e^{jU\cos\phi_e} d\phi_e \tag{5.250}$$

$$= \pi\left[-\frac{2}{\pi} + \mathbf{H}_1(U) + jJ_1(U)\right] . \tag{5.251}$$

The radiated fields using this approximation, give the physical optics (projected area) result in both the specular and forward scatter directions. Associating a half-rim with a diffraction point, the expression of the edge diffracted field becomes

$$\vec{E}_e^d = \vec{E}^i \cdot \overline{\overline{D}} \frac{e^{j\frac{\pi}{4}}\sqrt{2\pi k}\sin\beta_0 a}{2} \frac{f_0(U)}{\pi} e^{jk\gamma_e} \frac{e^{-jkr}}{r} . \tag{5.252}$$

Chaing's solution is a uniform solution. It can be written in the diffraction-point form by using a transition function in the diffraction coefficient, such that

$$\vec{E}_{rim}^d = \vec{E}_1^d + \vec{E}_3^d \tag{5.253}$$

where

$$\vec{E}_1^d = \vec{E}^i(Q_1) \cdot \overline{\overline{D}}(Q_1)\sqrt{\rho^d(Q_1)} e^{jk\vec{r}_1\cdot\hat{r}} \frac{e^{-jkr}}{r} \tag{5.254}$$

$$\vec{E}_3^d = \vec{E}^i(Q_3) \cdot \overline{\overline{D}}(Q_3)\sqrt{\rho^d(Q_3)} e^{jk\vec{r}_3\cdot\hat{r}} \frac{e^{-jkr}}{r} . \tag{5.255}$$

Again, Q_1 and Q_3 are the two diffraction points on the rim. The diffraction coefficient is

$$\overline{\overline{D}}(Q_e) = -\hat{\beta}_0{}'\hat{\beta}_0 D_s(Q_e) - \hat{\Phi}'\hat{\Phi} D_h(Q_e)$$

$$D_{s,h} = \frac{-e^{-j\frac{\pi}{4}}}{2n\sqrt{2\pi k}\sin\beta_0}(A(\Phi,\Phi') - B(\Phi,\Phi'))\mathbf{T}_e \tag{5.256}$$

where

$$\mathbf{T}_e(U) = \frac{1}{\pi}f_0(U)\sqrt{\frac{\pi U}{2}}e^{-j(U-\frac{\pi}{4})} \tag{5.257}$$

$$U(Q_e) = ka_e\hat{n}_e\cdot(\hat{r}+\hat{r}') \tag{5.258}$$

The transition function is $\mathbf{T}_e(U)$. The following are the small and large argument forms:

for $|U| \ll 1$

$$\mathbf{T}_e(U) \approx \sqrt{\frac{\pi U}{2}}e^{-j(U-\frac{\pi}{4})}\cdot \cdot\left\{\frac{2}{\pi} - \frac{2U^2}{3\pi}\left(1-\frac{U^2}{15}\right) + j\frac{U}{2}\left(1-\frac{U^2}{8}\right)\right\} \tag{5.259}$$

for $|U| \gg 1$

$$\mathbf{T}_e(U) \sim 1 + \frac{j3}{8U} - \sqrt{\frac{2}{\pi U}}\frac{1}{U}e^{-j(U-\frac{\pi}{4})} + \frac{15}{128U^2} - \frac{j105}{1024U^3} \tag{5.260}$$

The magnitude and phase of the the transition function $\mathbf{T}_e$ as a function of the argument U is shown in Figure 37.

5.4 Rim Shadowing

The previous equivalent edge current solutions assumed no shadowing or blockage of the rim from observation by the structure. In the actual situation,

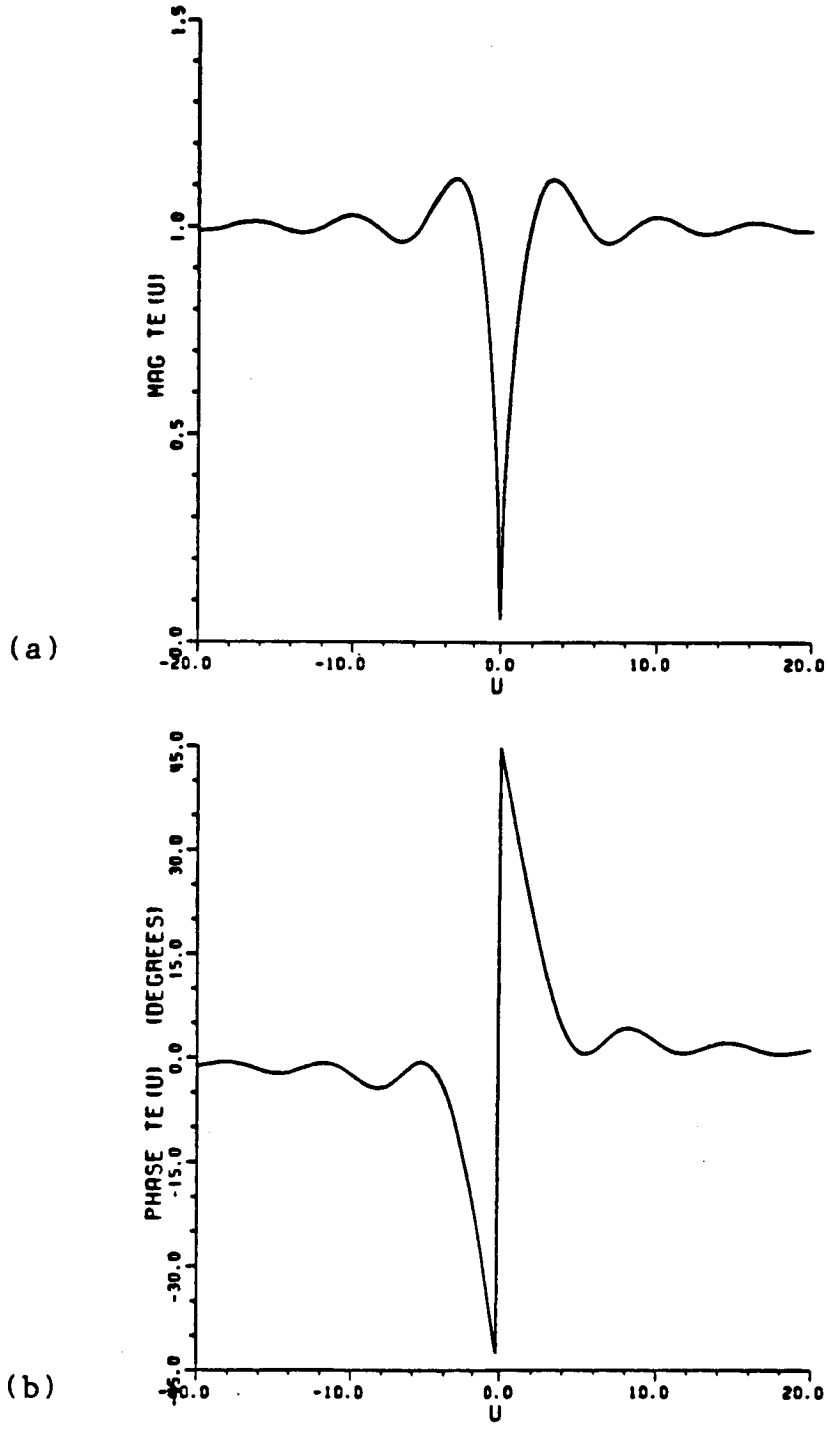

Figure 37: Transition function $\mathbf{T}_e$ (a) magnitude, and (b) phase.

however, we must consider partial rims—rims which are partially illuminated or visible. In order to know the size of these partial rims, we must first determine where the shadows are located.

The expressions for the surface normal and the direction of the source are known. For a circular cone frustum with $a_2 > a_1$, these are given by

$$\hat{n}_c = \hat{x}\cos\alpha_c\cos\phi_s + \hat{y}\cos\alpha_c\sin\phi_s + \hat{z}\sin\alpha_c \tag{5.261}$$

$$\hat{r}' = \hat{x}\sin\theta'\cos\phi' + \hat{y}\sin\theta'\sin\phi' + \hat{z}\cos\theta' . \tag{5.262}$$

At the boundary between the illuminated and shadowed portions of the cone frustum (the terminator), one obtains

$$\hat{n}_c \cdot \hat{r}' = 0 \tag{5.263}$$

or

$$A\cos\phi_s + B\sin\phi_s + C = 0 \tag{5.264}$$

where

$$A = \cos\alpha_c\sin\theta'\cos\phi' \tag{5.265}$$

$$B = \cos\alpha_c\sin\theta'\sin\phi' \tag{5.266}$$

$$C = \sin\alpha_c\cos\theta' . \tag{5.267}$$

The unknown that we want to find is ϕ_s. Let us make the following substitution for $\cos\phi_s$ and $\sin\phi_s$:

$$x = e^{j\phi_s} \tag{5.268}$$

$$\cos\phi_s = \frac{e^{j\phi_s} + e^{-j\phi_s}}{2} \tag{5.269}$$

$$= \frac{x + \frac{1}{x}}{2} \tag{5.270}$$

$$\sin\phi_s = \frac{e^{j\phi_s} - e^{-j\phi_s}}{2j} \tag{5.271}$$

$$= \frac{x - \frac{1}{x}}{2j}\,. \tag{5.272}$$

Equation (5.264) becomes

$$(B + jA)x^2 + j2Cx + (-B + jA) = 0\,. \tag{5.273}$$

We can then solve for x by using the quadratic formula. Solving for x yields

$$Re\{x\} = -\frac{\sin\alpha_c \cos\phi' \cos\theta' \mp \sin\phi' \sqrt{\cos^2\alpha_c - \cos^2\theta'}}{\cos\alpha_c \sin\theta'} \tag{5.274}$$

$$Im\{x\} = -\frac{\sin\alpha_c \sin\phi' \cos\theta' \mp \cos\phi' \sqrt{\cos^2\alpha_c - \cos^2\theta'}}{\cos\alpha_c \sin\theta'}\,. \tag{5.275}$$

The values of ϕ_s that correspond to the boundary between shadowed and illuminated portions on the cone frustum are

$$\phi_{s1,s2} = \tan^{-1}\left(\frac{Im\{x\}}{Re\{x\}}\right) \tag{5.276}$$

$$= \tan^{-1}\left(\frac{\sin\alpha_c \sin\phi' \cos\theta' \mp \cos\phi' \sqrt{\cos^2\alpha_c - \cos^2\theta'}}{\sin\alpha_c \cos\phi' \cos\theta' \mp \sin\phi' \sqrt{\cos^2\alpha_c - \cos^2\theta'}}\right)\,. \tag{5.277}$$

The above equation applies only for the case where $\cos^2\alpha_c > \cos^2\theta'$; otherwise, the rim would be completely illuminated or all in the shadow.

In order to know how the shadowed rim appears, we need to know the region where the source is located (see Figures 12 and 38). The results of this section

apply equally well to finding the portion of the rim that is blocked from view by the cone structure.

5.5 Partial Rim Corrections

In the equivalent-edge-current solutions, we associated a half-rim with each edge diffraction point. As a result, there are half-rim integrals in the transition functions of the diffraction coefficients. If the shadowing of the rim is considered, we will have partial half-rim integrals. In this section we will provide corrections to the half-rim integrals by subtracting the portion that is shadowed or not visible. Let

$$f_{c0}(U) = \int_{-\frac{\pi}{2}}^{\frac{\pi}{2}} \cos\phi_e e^{j\psi_e} d\phi_e - C_A(U) \tag{5.278}$$

$$f_{c1}(U) = \int_{-\frac{\pi}{2}}^{\frac{\pi}{2}} \cos^2\phi_e e^{j\psi_e} d\phi_e - C_B(U) \tag{5.279}$$

$$f_{c2}(U) = \cos\theta\cos\theta' \int_{-\frac{\pi}{2}}^{\frac{\pi}{2}} \sin^2\phi_e e^{j\psi_e} d\phi_e - C_C(U)\,. \tag{5.280}$$

The correction terms are given by C_A, C_B, and C_C (see Figure 39). If the center of the half-rim is missing the correction terms are

$$C_A(U) = \int_{\phi_1}^{\phi_2} \cos\phi_e e^{j\psi_e} d\phi_e \tag{5.281}$$

$$C_B(U) = \int_{\phi_1}^{\phi_2} \cos^2\phi_e e^{j\psi_e} d\phi_e \tag{5.282}$$

$$C_C(U) = \cos\theta\cos\theta' \int_{\phi_1}^{\phi_2} \sin^2\phi_e e^{j\psi_e} d\phi_e \tag{5.283}$$

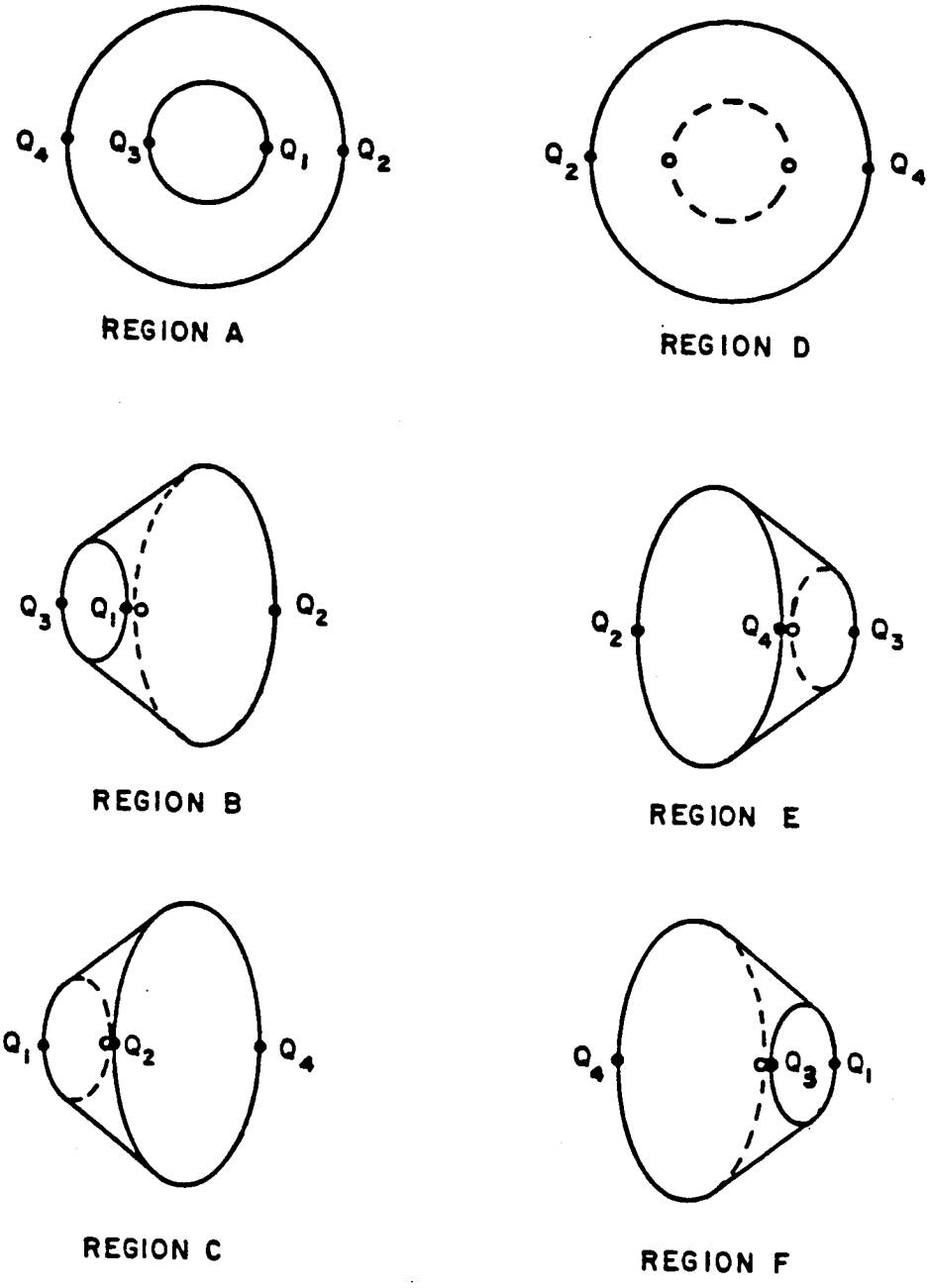

Figure 38: Views of the cone frustum in various regions.

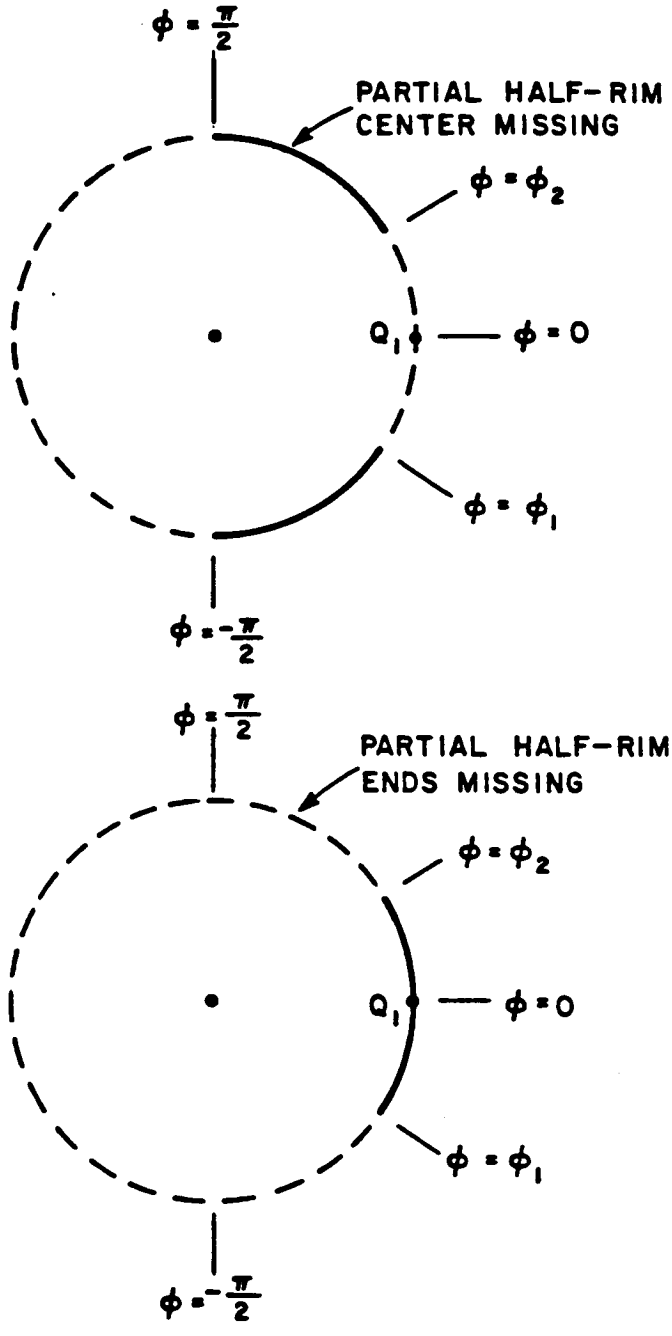

Figure 39: Two types of partial half-rims.

where $-\frac{\pi}{2} < \phi_1 < 0$, $0 < \phi_2 < \frac{\pi}{2}$, and $|\phi_1| = |\phi_2|$. If the ends of the half-rim are missing the correction terms are

$$C_A(U) = 2\int_{-\frac{\pi}{2}}^{\phi_1} \cos\phi_e e^{j\psi_e} d\phi_e \tag{5.284}$$

$$C_B(U) = 2\int_{-\frac{\pi}{2}}^{\phi_1} \cos^2\phi_e e^{j\psi_e} d\phi_e \tag{5.285}$$

$$C_C(U) = 2\cos\theta\cos\theta' \int_{-\frac{\pi}{2}}^{\phi_1} \sin^2\phi_e e^{j\psi_e} d\phi_e \,. \tag{5.286}$$

These integrals may be evaluated for small values of $|U|$ by the following series form obtained by expanding the exponential. It converges rapidly due to the $k!$ in the denominator of each term. This is sufficient, since for $|U|$ greater than about 8, we are out of the transition region, and the correction would not be necessary.

$$\int \cos\phi_e e^{j\psi_e} d\phi_e = \sum_{k=0}^{\infty} j^k \frac{U^k}{k!} \int \cos^{k+1}\phi_e d\phi_e \tag{5.287}$$

$$\int \cos^2\phi_e e^{j\psi_e} d\phi_e = \sum_{k=0}^{\infty} j^k \frac{U^k}{k!} \int \cos^{k+2}\phi_e d\phi_e \tag{5.288}$$

$$\int \sin^2\phi_e e^{j\psi_e} d\phi_e = \sum_{k=0}^{\infty} j^k \frac{U^k}{k!} \int \cos^{k}\phi_e d\phi_e - C_B(U) \tag{5.289}$$

and

$$\int \cos^n\phi_e d\phi_e = \frac{1}{n}\cos^{n-1}\phi_e \sin\phi_e + \frac{n-1}{n}\int \cos^{n-2}\phi_e d\phi_e \,. \tag{5.290}$$

The number of terms required in the series increases as $|U|$ increases.

Tables 5.1 and 5.2 show the diffraction points associated with a partial half-rim, the type of partial half-rim, and operations to determine the limits of integration $\phi_{1,2}$ for various regions of observation and illumination. The symbols used

in the table refer to the following:

$$R^i = \text{illumination region}$$

$$R^r = \text{observation region}$$

$$L_{Q1} = \begin{cases} 1 & Q_1 \text{ considered} \\ 0 & Q_1 \text{ not considered} \end{cases}$$

$$L_{Q2} = \begin{cases} 1 & Q_2 \text{ considered} \\ 0 & Q_2 \text{ not considered} \end{cases}$$

$$L_{Q3} = \begin{cases} 1 & Q_3 \text{ considered} \\ 0 & Q_3 \text{ not considered} \end{cases}$$

$$L_{Q4} = \begin{cases} 1 & Q_4 \text{ considered} \\ 0 & Q_4 \text{ not considered} \end{cases}$$

$$L_{cen} = \begin{cases} 1 & \text{partial half-rim with center missing} \\ 0 & \text{complete half-rim} \end{cases}$$

$$L_{end} = \begin{cases} 1 & \text{partial half-rim with ends missing} \\ 0 & \text{complete half-rim} \end{cases}$$

$$> = \begin{cases} 1 & \phi_{s1,s2} \text{ with greater } |\phi_{s2} - \phi s1| \text{ are } \phi_{1,2} \\ 0 & — \end{cases}$$

$$< = \begin{cases} 1 & \phi_{s1,s2} \text{ with smaller } |\phi_{s2} - \phi s1| \text{ are } \phi_{1,2} \\ 0 & — \end{cases}$$

$$\Delta^i = \begin{cases} 1 & \phi_{s1,s2} \text{ of source region are } \phi_{1,2} \\ 0 & — \end{cases}$$

$$\Delta^r = \begin{cases} 1 & \phi_{s1,s2} \text{ of observation region are } \phi_{1,2} \\ 0 & — \end{cases}$$

The following is a step-by-step procedure to find the correction terms:

1. Determine the regions of the source and receiver (see Figure 12).

2. Consult Tables 5.1 and 5.2. Check if a partial half-rim is present, and the diffraction point associated with each partial half-rim. If no partial half-rim is present or if $|U| > 8$, then no correction is necessary.

3. If a partial half-rim is present, find the values of $\phi_{s1,s2}$ given by Equation (5.277) for both the source and receiver.

4. Consult Tables 5.1 and 5.2 and perform the indicated operation and obtain the limits of integration $\phi_{1,2}$.

5. Depending on type of partial half-rim (whether the ends or the center of the half-rim is missing), evaluate the appropriate integrals and obtain the correction terms.

5.6 The Diffraction-Point Method Solution with Corrections for Rim-Caustic Regions

The corrections for the rim-caustic regions are provided by the transition functions in the diffraction coefficient. The transition function used depends on the rim-caustic region considered. For rim-caustic regions associated with the specular

Table 5.1: Table for evaluation of partial half-rim.

Region		Point				Partial Rim		Operation			
R^i	R^r	L_{Q1}	L_{Q2}	L_{Q3}	L_{Q4}	L_{cen}	L_{end}	$>$	$<$	Δ^i	Δ^r
A	A	0	0	0	0	0	0	0	0	0	0
A	B	0	0	0	1	1	0	0	0	0	1
A	C	1	0	0	0	0	1	0	0	0	1
A	D	0	0	0	0	0	0	0	0	0	0
A	E	0	0	1	0	0	1	0	0	0	1
A	F	0	1	0	0	1	0	0	0	0	1
B	A	0	0	0	1	1	0	0	0	1	0
B	B	0	0	0	1	1	0	1	0	0	0
B	C	1	0	0	0	0	1	0	0	0	1
B	C	0	0	0	1	1	0	0	0	1	0
B	D	0	0	0	1	1	0	0	0	1	0
B	E	0	0	1	0	0	1	0	0	0	1
B	E	0	0	0	1	1	0	0	0	1	0
B	F	0	1	0	1	1	0	0	1	0	0
C	A	1	0	0	0	0	1	0	0	1	0
C	B	1	0	0	0	0	1	0	0	1	0
C	B	0	0	0	1	1	0	0	0	0	1
C	C	1	0	0	0	0	1	0	1	0	0
C	D	0	0	0	0	0	0	0	0	0	0
C	E	0	0	0	0	0	0	0	0	0	0
C	F	1	0	0	0	0	1	0	0	1	0
C	F	0	1	0	0	1	0	0	0	0	1

Table 5.2: Table for evaluation of partial half-rim.

Region		Point				Partial Rim		Operation			
R^i	R^r	L_{Q1}	L_{Q2}	L_{Q3}	L_{Q4}	L_{cen}	L_{end}	>	<	Δ^i	Δ^r
D	A	0	0	0	0	0	0	0	0	0	0
D	B	0	0	0	1	1	0	0	0	0	1
D	C	0	0	0	0	0	0	0	0	0	0
D	D	0	0	0	0	0	0	0	0	0	0
D	E	0	0	0	0	0	0	0	0	0	0
D	F	0	1	0	0	1	0	0	0	0	1
E	A	0	0	1	0	0	1	0	0	1	0
E	B	0	0	1	0	0	1	0	0	1	0
E	B	0	0	0	1	1	0	0	0	0	1
E	C	0	0	0	0	0	0	0	0	0	0
E	D	0	0	0	0	0	0	0	0	0	0
E	E	0	0	1	0	0	1	0	1	0	0
E	F	0	0	1	0	0	1	0	0	1	0
E	F	0	1	0	0	1	0	0	0	0	1
F	A	0	1	0	0	1	0	0	0	1	0
F	B	0	1	0	1	1	0	0	1	0	0
F	C	1	0	0	0	0	1	0	0	0	1
F	C	0	1	0	0	1	0	0	0	1	0
F	D	0	1	0	0	1	0	0	0	1	0
F	E	0	0	1	0	0	1	0	0	0	1
F	E	0	1	0	0	1	0	0	0	1	0
F	F	0	1	0	0	1	0	1	0	0	0

or forward-scatter direction of the endcap, we use the function $\mathbf{T}_e$. For the other regions, the functions $\mathbf{T}_{e1}$ and $\mathbf{T}_{e2}$ are used. The new diffraction coefficient with corrections for the rim-caustic region is

$$\overline{\overline{D}}(Q_e) = -\hat{\beta}_0{}'\hat{\beta}_0 D_s(Q_e) - \hat{\Phi}'\hat{\Phi} D_h(Q_e)$$

$$D_s(Q_e) = \frac{-e^{-j\frac{\pi}{4}}}{2n\sqrt{2\pi k}\sin\beta_0}(A\mathbf{T}_{e1}(U) - B\mathbf{T}_{e2}(U)) \quad (5.291)$$

$$D_h(Q_e) = \frac{-e^{-j\frac{\pi}{4}}}{2n\sqrt{2\pi k}\sin\beta_0}(A\mathbf{T}_{e2}(U) + B\mathbf{T}_{e1}(U)) \quad (5.292)$$

where

$$A(\Phi,\Phi') = \cot\left(\frac{\pi+(\Phi-\Phi')}{2n}\right) + \cot\left(\frac{\pi-(\Phi-\Phi')}{2n}\right) \quad (5.293)$$

$$B(\Phi,\Phi') = \cot\left(\frac{\pi+(\Phi+\Phi')}{2n}\right) + \cot\left(\frac{\pi-(\Phi+\Phi')}{2n}\right). \quad (5.294)$$

The transition functions are

$$\mathbf{T}_{e1}(U) = \frac{1}{\pi}(f_{c1}(U) - f_{c2}(U))\sqrt{\frac{\pi U}{2}}e^{-j(U-\frac{\pi}{4})} \quad (5.295)$$

$$\mathbf{T}_{e2}(U) = \frac{1}{\pi}(f_{c1}(U) + f_{c2}(U))\sqrt{\frac{\pi U}{2}}e^{-j(U-\frac{\pi}{4})} \quad (5.296)$$

$$U(Q_e) = ka_e\hat{n}_e\cdot(\hat{r}+\hat{r}') \quad (5.297)$$

if $(\hat{n}_o\cdot\hat{r}') > 0$ or $(\hat{n}_o\cdot\hat{r}) > 0$ then

$$\mathbf{T}_{e1}(U) = \mathbf{T}_{e2}(U) = \mathbf{T}_e(U) \quad (5.298)$$

$$\mathbf{T}_e(U) = \frac{1}{\pi}f_{c0}(U)\sqrt{\frac{\pi U}{2}}e^{-j(U-\frac{\pi}{4})} \quad (5.299)$$

where

$$f_{c0}(U) = \pi\left[\frac{\pi}{2} - \mathbf{H}_1(U) + jJ_1(U)\right] - C_A(U) \quad (5.300)$$

$$f_{c1}(U) = \pi\left[\left(J_0(U) - \frac{J_1(U)}{U}\right) + j\left(\mathbf{H}_0(U) - \frac{\mathbf{H}_1(U)}{U}\right)\right] - C_B(U) \tag{5.301}$$

$$f_{c2}(U) = (\hat{n}_o \cdot \hat{r}')(\hat{n}_o \cdot \hat{r})\pi\left(\frac{J_1(U)}{U} + j\frac{\mathbf{H}_1(U)}{U}\right) - C_C(U) \tag{5.302}$$

and $C_A(U)$, $C_B(U)$, and $C_C(U)$ are the correction factors for a partial half-rim. Outside the rim-caustic regions the transition functions are unity.

The diffraction-point method solution with the rim-caustic correction, except for the new diffraction coefficient, has the original form which is given by

$$\vec{E}^s \approx \vec{E}^d_{total} = \vec{E}^d_1 + \vec{E}^d_2 + \vec{E}^d_3 + \vec{E}^d_4 \tag{5.303}$$

where

$$\vec{E}^d_1 = \vec{E}^i(Q_1) \cdot \overline{\overline{D}}(Q_1)\sqrt{\rho^d(Q_1)}e^{jkr\vec{1}\cdot\hat{r}}\frac{e^{-jkr}}{r} \tag{5.304}$$

$$\vec{E}^d_2 = \vec{E}^i(Q_2) \cdot \overline{\overline{D}}(Q_2)\sqrt{\rho^d(Q_2)}e^{jkr\vec{2}\cdot\hat{r}}\frac{e^{-jkr}}{r} \tag{5.305}$$

$$\vec{E}^d_3 = \vec{E}^i(Q_3) \cdot \overline{\overline{D}}(Q_3)\sqrt{\rho^d(Q_3)}e^{jkr\vec{3}\cdot\hat{r}}\frac{e^{-jkr}}{r} \tag{5.306}$$

$$\vec{E}^d_4 = \vec{E}^i(Q_4) \cdot \overline{\overline{D}}(Q_4)\sqrt{\rho^d(Q_4)}e^{jkr\vec{4}\cdot\hat{r}}\frac{e^{-jkr}}{r}. \tag{5.307}$$

Figure 40 shows how the calculated pattern, using the diffraction-point method with rim-caustic corrections, compares with the original diffraction-point method solution.

The curved-side specular-region correction of the previous chapter can be introduced into this solution by multiplying the appropriate reflection-boundary term of the diffraction coefficient by the transition function (**T**). This is shown in the following diffraction coefficient with both the rim-caustic and curved-surface

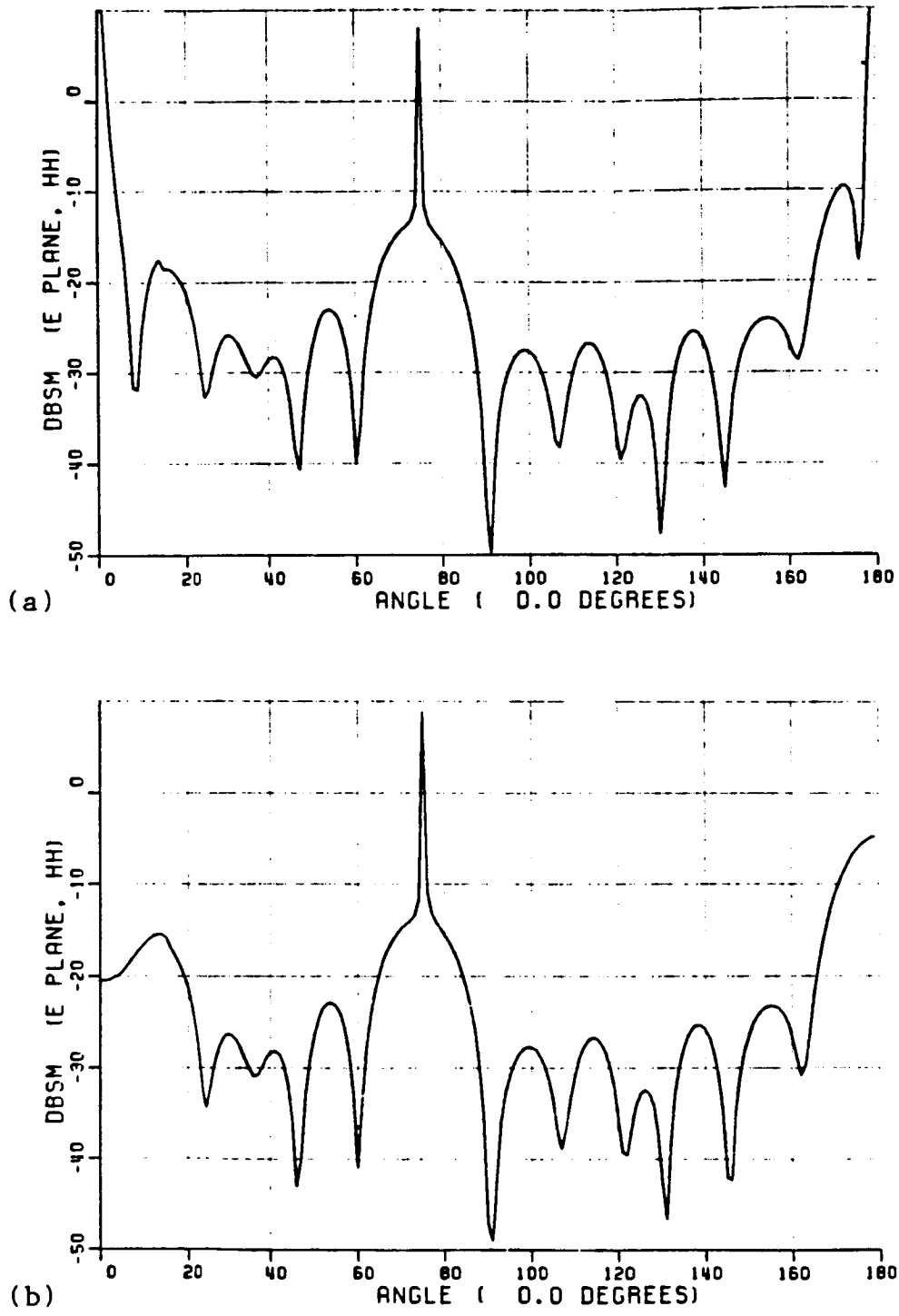

Figure 40: Backscatter from a 15° cone frustum using (a) the diffraction-point method, and (b) the diffraction-point method with rim caustic correction.

specular-region corrections:

$$\overline{\overline{D}}^{\mp}(Q_e) = -\hat{\beta}_0{}'\hat{\beta}_0 D_s^{\mp}(Q_e) - \hat{\Phi}'\hat{\Phi} D_h^{\mp}(Q_e)$$

$$D_s^{\mp}(Q_e) = \frac{-e^{-j\frac{\pi}{4}}}{2n\sqrt{2\pi k}\sin\beta_0}(A\mathbf{T}_{e1}(U) - B^{\mp}\mathbf{T}_{e2}(U)) \tag{5.308}$$

$$D_h^{\mp}(Q_e) = \frac{-e^{-j\frac{\pi}{4}}}{2n\sqrt{2\pi k}\sin\beta_0}(A\mathbf{T}_{e2}(U) + B^{\mp}\mathbf{T}_{e1}(U)) \tag{5.309}$$

where

$$A(\Phi,\Phi') = \cot\left(\frac{\pi+(\Phi-\Phi')}{2n}\right) + \cot\left(\frac{\pi-(\Phi-\Phi')}{2n}\right) \tag{5.310}$$

$$B^{\mp}(\Phi,\Phi') = \cot\left(\frac{\pi+(\Phi+\Phi')}{2n}\right)\mathbf{T}(\pm jXa_e) + \cot\left(\frac{\pi-(\Phi+\Phi')}{2n}\right) \tag{5.311}$$

The corrected diffraction-point method solution is

$$\vec{E}^s \approx \vec{E}^d_{total} = \vec{E}^d_1 + \vec{E}^d_2 + \vec{E}^d_3 + \vec{E}^d_4 \tag{5.312}$$

where

$$\vec{E}^d_1 = \vec{E}^i(Q_1)\cdot\overline{\overline{D}}^{+}(Q_1)\sqrt{\rho^d(Q_1)}e^{jkr\vec{r}_1\cdot\hat{r}}\frac{e^{-jkr}}{r} \tag{5.313}$$

$$\vec{E}^d_2 = \vec{E}^i(Q_2)\cdot\overline{\overline{D}}^{-}(Q_2)\sqrt{\rho^d(Q_2)}e^{jkr\vec{r}_2\cdot\hat{r}}\frac{e^{-jkr}}{r} \tag{5.314}$$

$$\vec{E}^d_3 = \vec{E}^i(Q_3)\cdot\overline{\overline{D}}^{+}(Q_3)\sqrt{\rho^d(Q_3)}e^{jkr\vec{r}_3\cdot\hat{r}}\frac{e^{-jkr}}{r} \tag{5.315}$$

$$\vec{E}^d_4 = \vec{E}^i(Q_4)\cdot\overline{\overline{D}}^{-}(Q_4)\sqrt{\rho^d(Q_4)}e^{jkr\vec{r}_4\cdot\hat{r}}\frac{e^{-jkr}}{r}. \tag{5.316}$$

The "corrected diffraction-point method solution" is the first-order UTD edge-diffraction solution with uniform corrections for the rim-caustic regions and for the curved-surface specular region. In Chapter 6, we will show how the corrected diffraction-point method solution compares with experimental backscatter measurements. And in Chapter 7, we will compare it against the moment method solution.

CHAPTER VI

Comparisons with Experimental Measurements

In order to verify our theoretical results and to provide confidence in our computer-generated patterns, a comparison with experimental measurements will be made. The measurements were performed in the Ohio State University ElectroScience Laboratory compact radar range.

Figure 41 shows the circular cone frustum that was used. It is constructed out of rolled brass sheet for the surface and brass plates for the endcaps which were soldered together. All seams were covered with metal tape. During the measurement, the cone frustum is held by a styrofoam column on top of a low RCS pedestal. The contributions from the mounting and background can be subtracted out of the measurements.

Two types of measurements were performed on the cone frustum. One is a backscatter measurement at a fixed frequency as the frustum is rotated 360 degreees—this generates a scattering pattern in the plane of rotation. The second type of measurement generates an impulse response. Backscatter measurements for a fixed aspect angle are taken, as the frequency is swept over a broad range. Performing an inverse Fourier transform on the data produces a band-limited version of the impulse response.

The principal plane backscatter measurements are shown in Figures 42 and 43 which are compared with the calculated UTD results. The measurements were

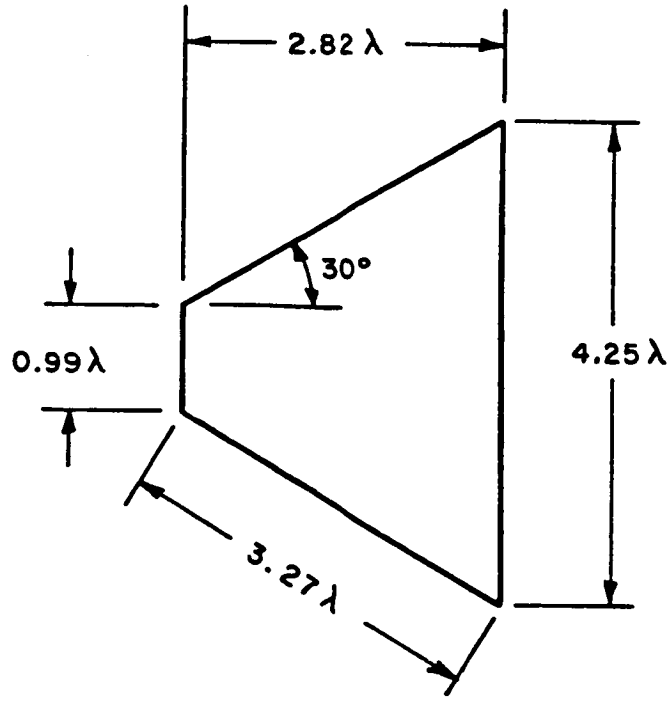

Figure 41: Cone frustum used for measurements, $f = 4.00$ GHz.

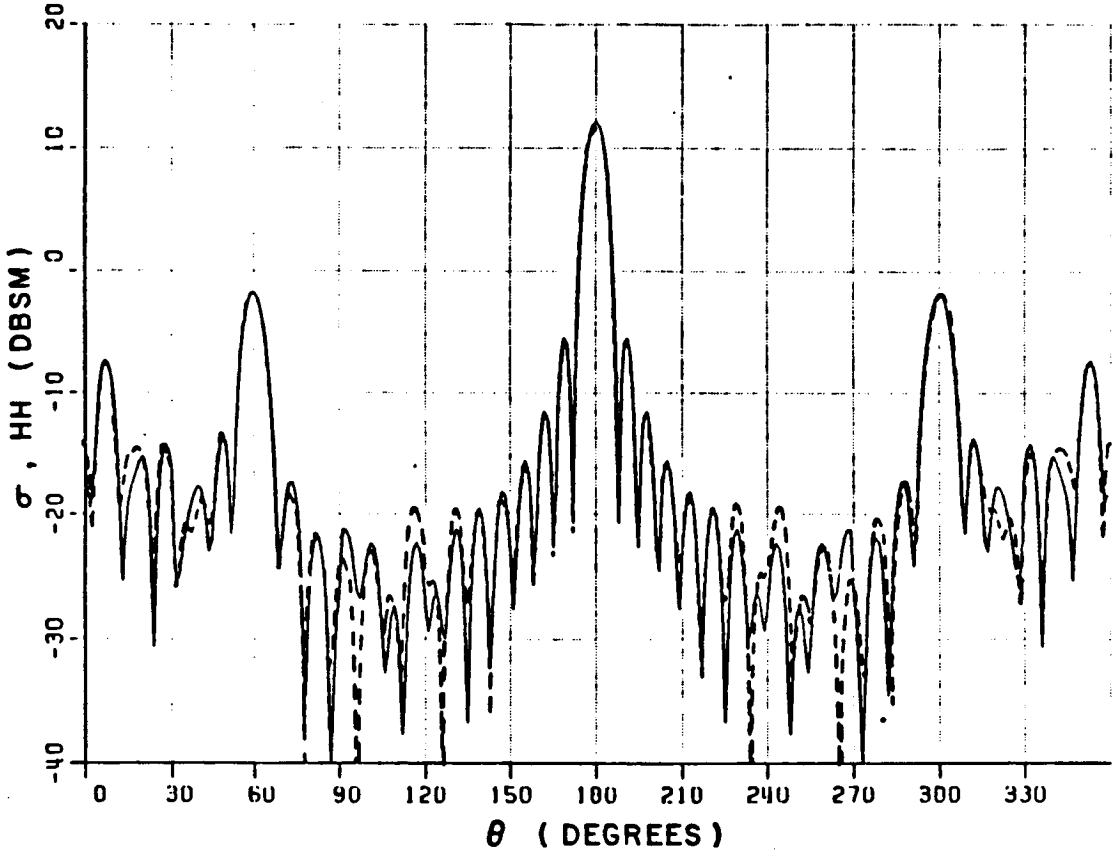

Figure 42: Cone frustum backscatter pattern for horizontal polarization at 4.00 GHz obtained using UTD (solid line) and measurement (dashed line).

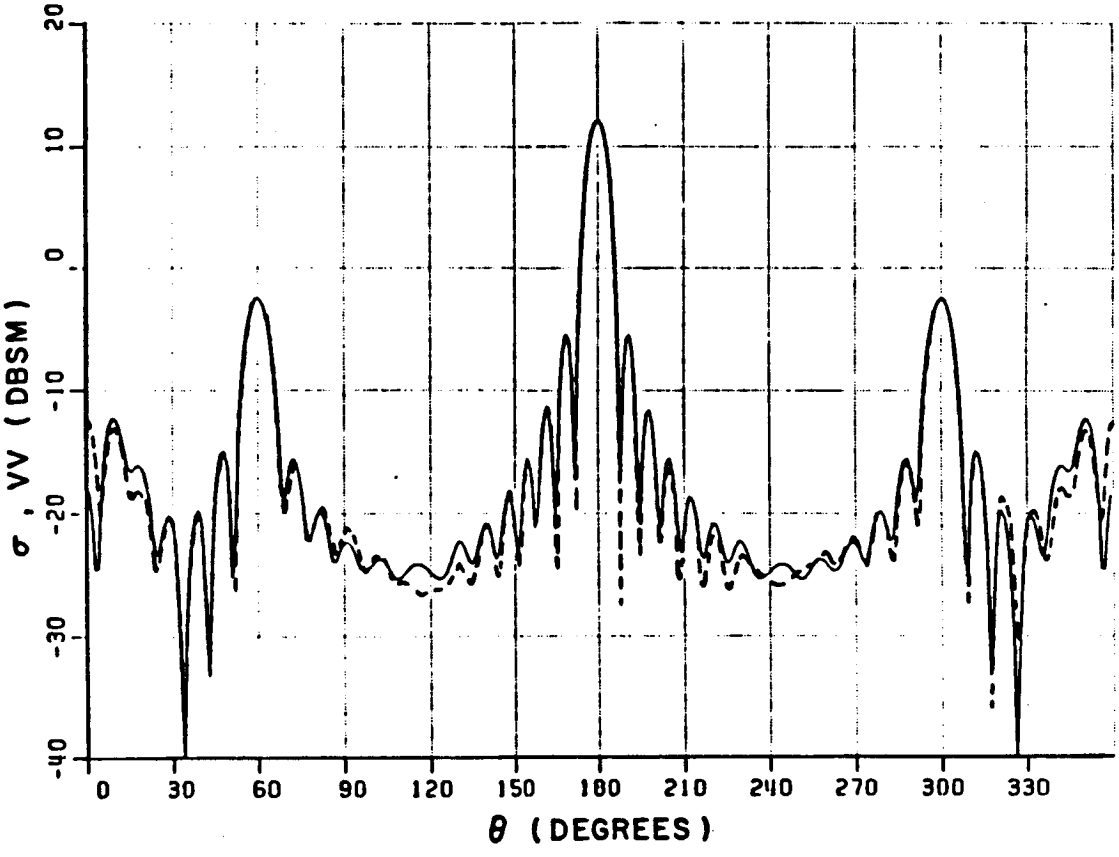

Figure 43: Cone frustum backscatter pattern for vertical polarization at 4.00 GHz obtained using UTD (solid line) and measurement (dashed line).

performed at a frequency of 4 GHz for both horizontal and vertical polariztions. Symmetry in the measured pattern gives a good indication of its reliability. There is excellent correlation at most of the significant peaks (within 1 dB), and the differences can be explained.

Higher-order diffractions are probably the best explaination for the differences between the measured and calculated patterns. The effects of double edge diffraction are usually strongest at the surface boundaries and for the horizontal (hard) polarization case. (The vertical polarized wave tends to get shorted out along the conducting surface.) Looking at the pattern for horizontal polarization, we note the discontinuities and the differences in the calculated result at 90 and 270 degrees. This indicates that multiple diffractions across the endcaps are significant in this region. The discrepancies at 15 and 345 degrees are also probably due to a higher order diffraction along the curved surface.

Higher-order terms in the UTD solution may also resolve the difference at 0 degrees axial incidence. We notice that there is about a 5 dB difference. At 0 degrees, we are facing the frustum nose-on, and it is a very frequency sensitive region due to the interference between the diffracted fields of back and front rims. Let us see what happens when the frequency of the calculated pattern is shifted slightly from 4.00 GHz to 4.05 GHz (see Figures 44 and 45). An increase of 5 dB occurs at 0 degrees with very little change in the pattern elsewhere. The reason for such a dramatic change will be clearer when we look at the backscatter frequency scan plot.

Figure 46 shows the calculated UTD frequency scan plot for 0 degrees axial incidence. (Polarization does not matter due to the symmetry.) The oscillation observed in the plot is due to the interaction between the contributions from the front endcap and the back rim. As the frequency decreases, the variation in the

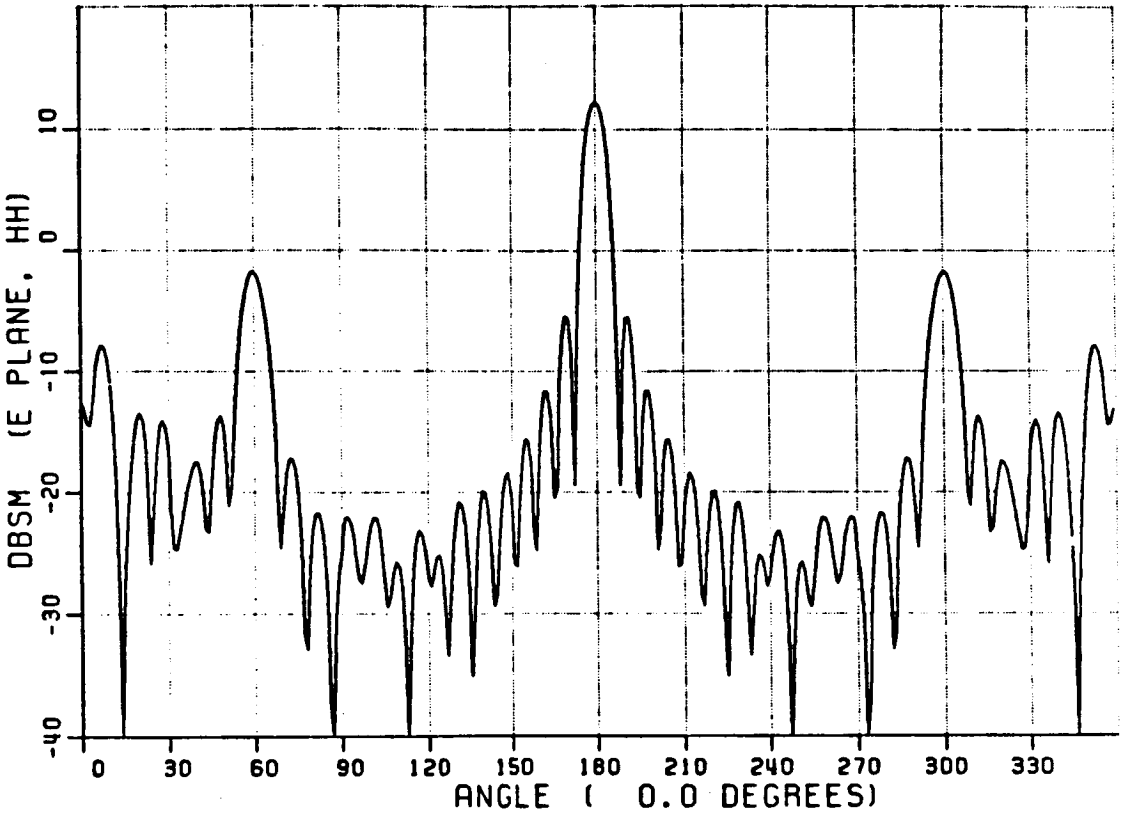

Figure 44: Cone frustum backscatter pattern for horizontal polarization at 4.05 GHz obtained using UTD.

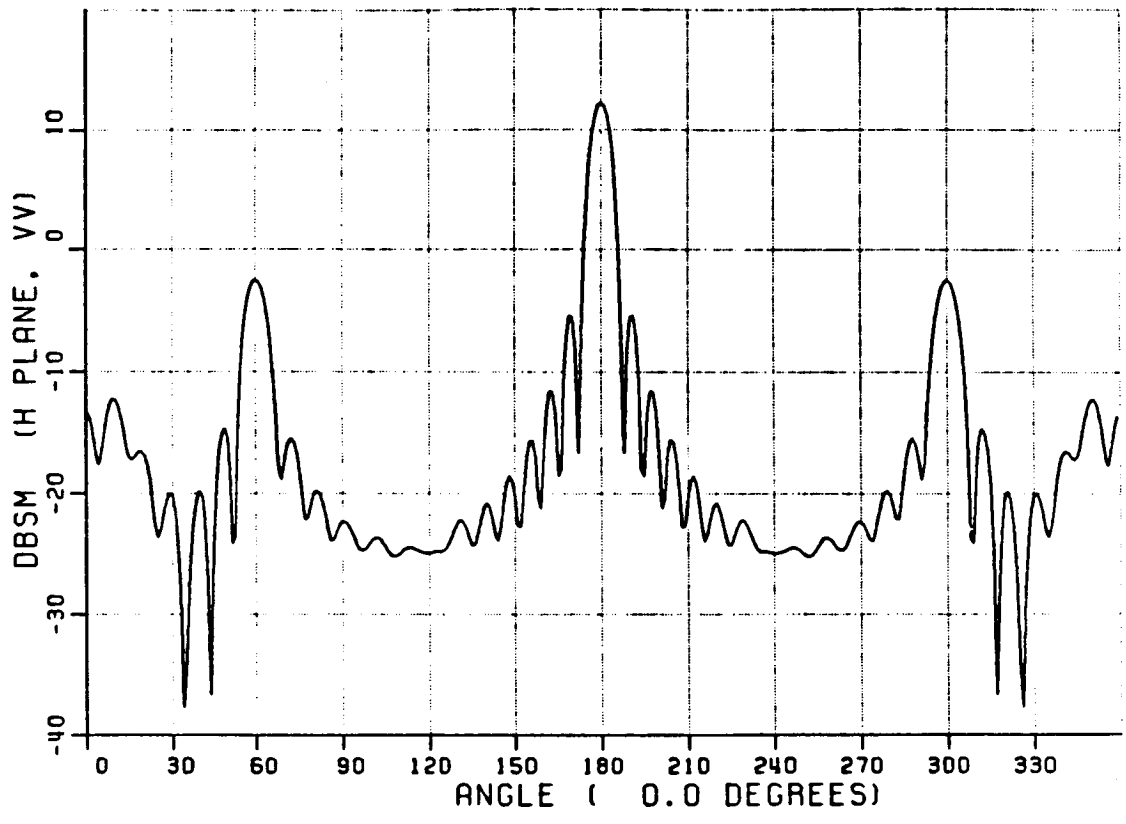

Figure 45: Cone frustum backscatter pattern for vertical polarization at 4.05 GHz obtained using UTD.

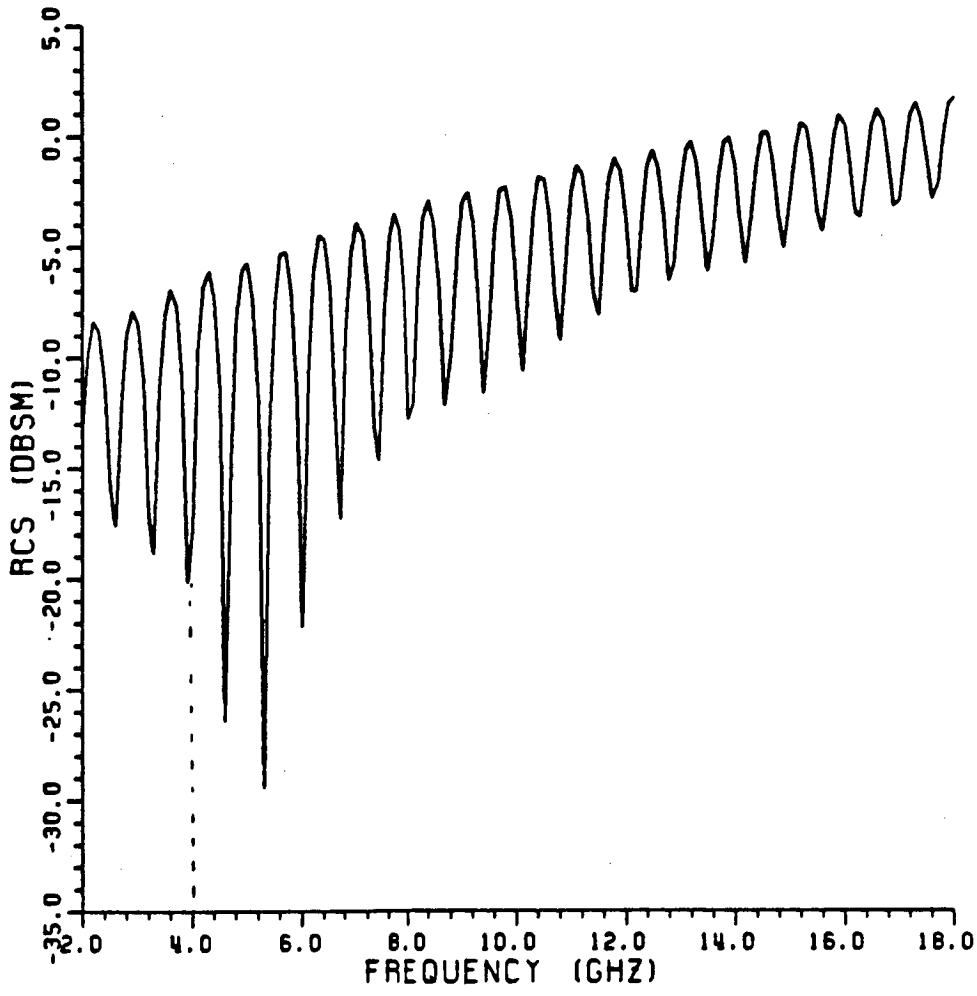

Figure 46: Calculated backscatter plot using UTD for a scan in frequency from 2 to 18 GHz at 0° axial incidence.

magnitude becomes greater due to the increasing diffracted field from the back rim over the specular reflection from the front endcap. Note that near 4 GHz we have a sharp null. This explains why we have a large change in magnitude with only a slight change in frequency. Higher-order terms, which become more significant at lower frequncies, might be responsible for slight phase differences that would shift the actual backscatter frequency scan plot.

Next, let us look at the backscatter impulse responses at 0 degrees, or axial incidence. The frequency was varied from 6 to 18 GHz. The calculated and measured plots are shown in Figures 47 and 48. An inverse Fourier transform is performed and the resulting band-limited impulse reponses are shown in Figure 49. The phase references of measured and calculated patterns are not the same—which results in a shift in time. The impulse response from the measured data shows a dominant contribution from the from endcap followed by a contribution from the back endcap rim. This is followed by a lesser contribution which is a double diffraction across the back endcap. The calculated plot compares well, except of course, there are no double diffractions.

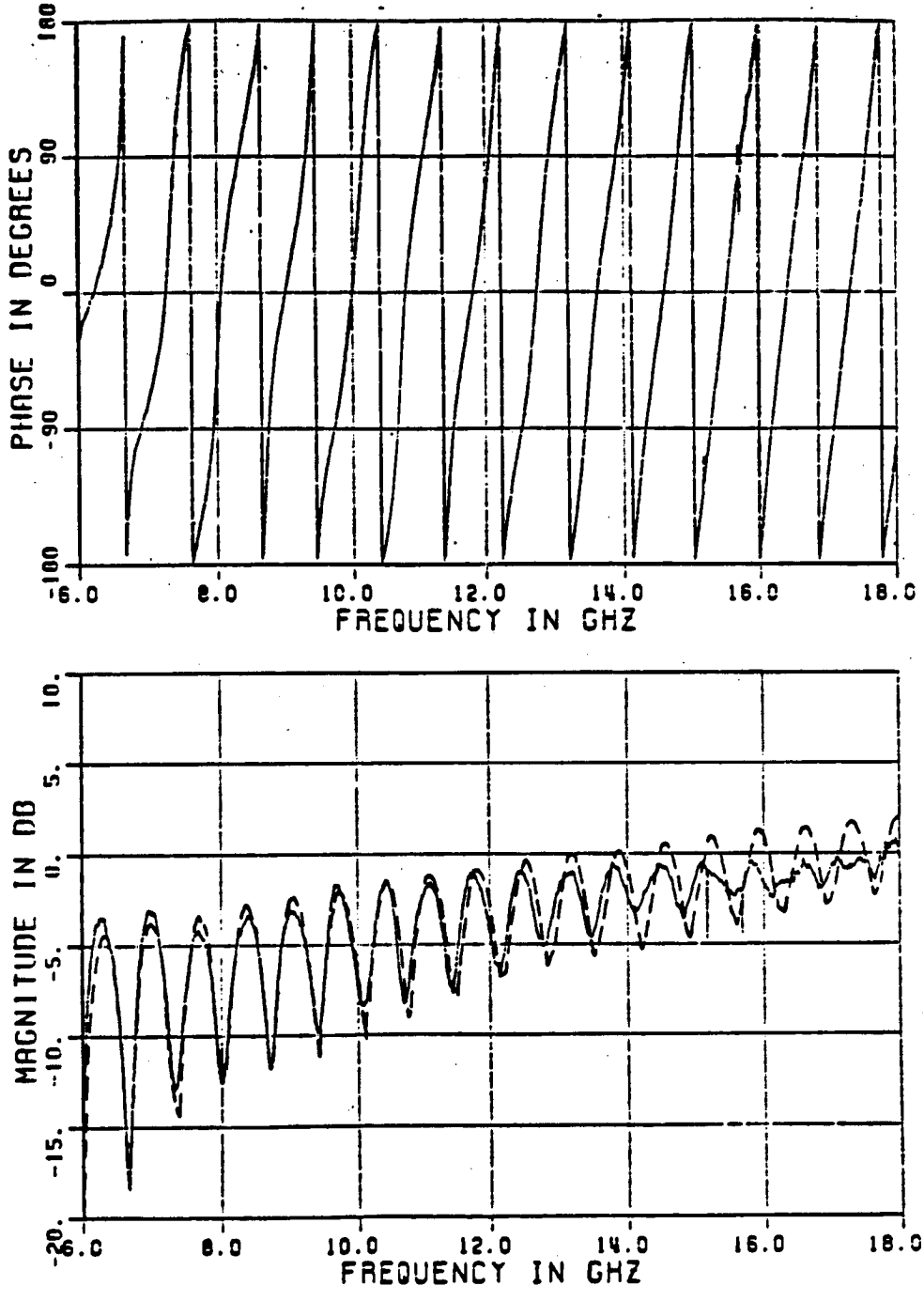

Figure 47: Measured backscatter plot (UTD dashed line) for a scan in frequency from 6 to 18 GHz at 0° axial incidence.

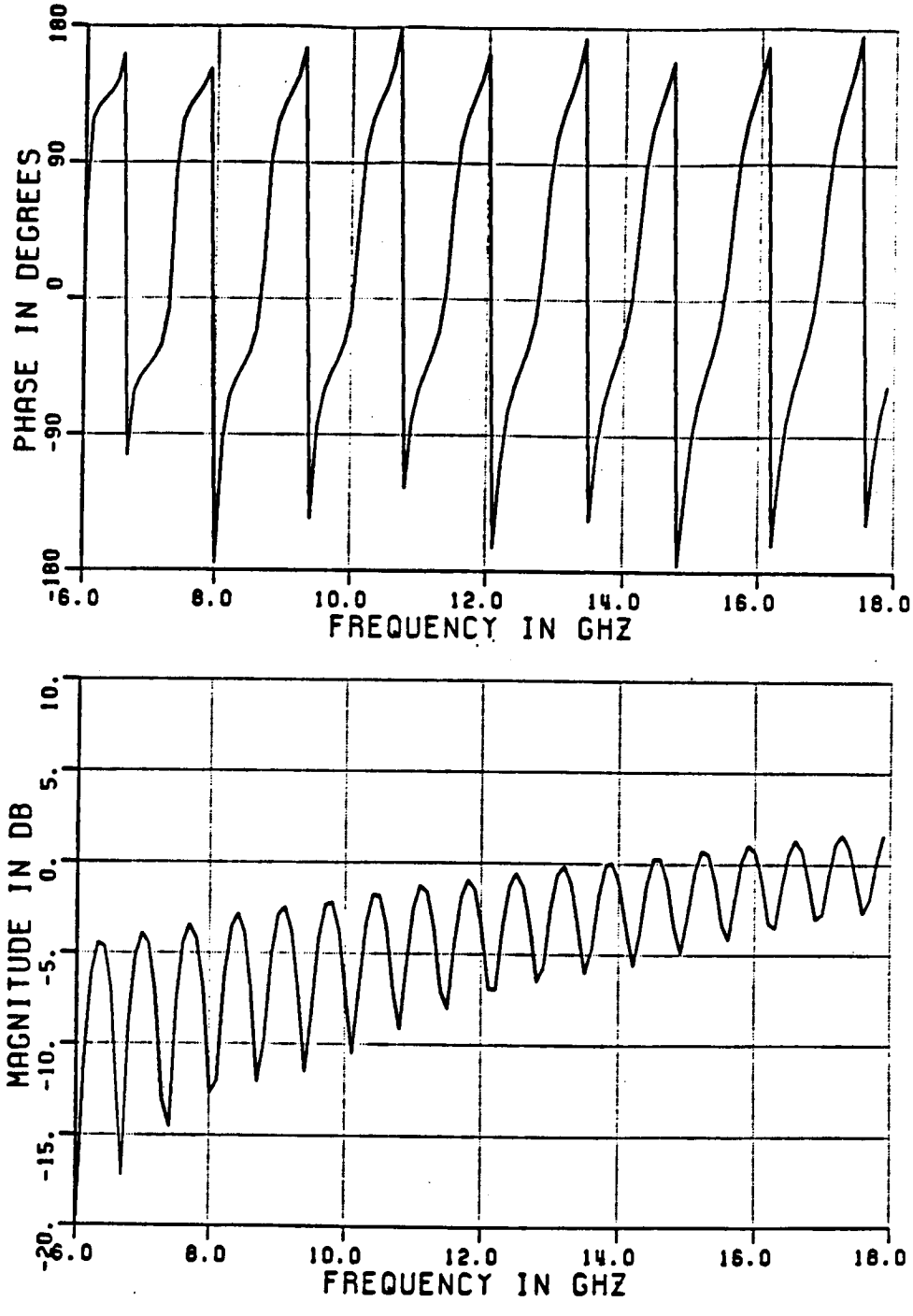

Figure 48: Calculated backscatter plot using UTD for a scan in frequency from 6 to 18 GHz at 0° axial incidence.

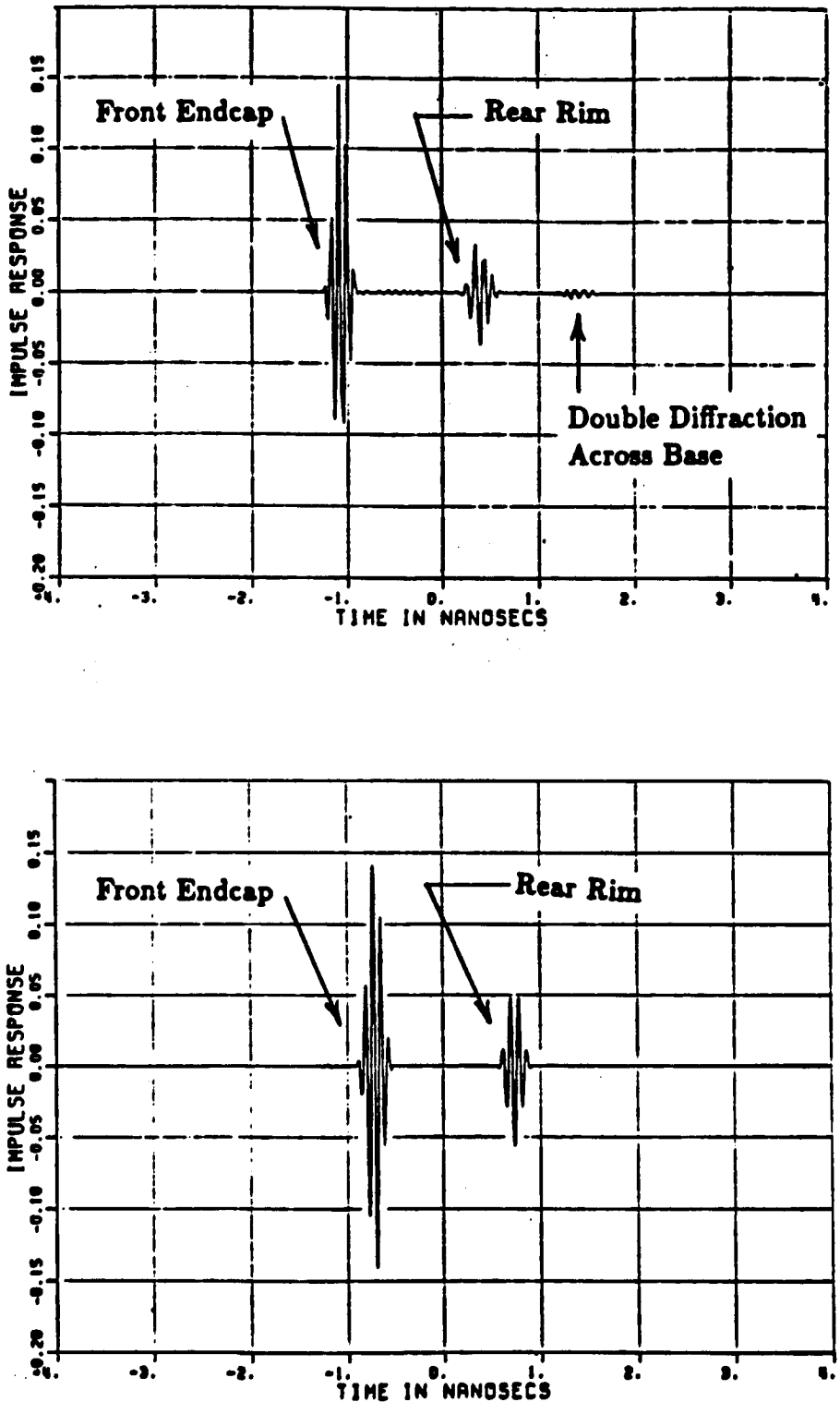

Figure 49: Impulse response using measured (top) and calculated UTD (bottom) backscatter data from 6 to 18 GHz for 0° axial incidence.

CHAPTER VII

Comparisons with the Moment Method Solution

In the last chapter comparisons were made with backscatter measurements. The good agreement gives us greater confidence that the theory and computer code are working as it should. However, the theory has not yet been tested for bistatic angles.

In this chapter, the calculated UTD results will be compared with results obtained by using the moment method. (We have a great deal of confidence in the moment method solution which is regarded as an "exact" solution for these calculations.) We make our comparisons with the moment method solution because accurate bistatic measurements are often difficult to obtain. This is especially true for large bistatic angles where there might be significant coupling of the incident field into the receiver.

For the cone frustum, the moment method solution presented in reference [16] will be used. It can determine the plane-wave scattering for any rotationally symmetric conducting body. Using this solution, C.W. Chuang [17] has developed a computer code that can generate bistatic scattering patterns for fixed angles of incidence.

The fixed incidence angles of $\theta' = 0$, 15, and 30 degrees are chosen for the cone frustum. Larger angles are possible, but due to the longer computer run times required, they are avoided. The frustum dimensions will be the same as that

used for the measurements (see Figure 41). Again, due to the amount of computer time, larger dimensions were not chosen.

Now let's look at the calculated bistatic principal plane patterns. Figures 50 through 55 show the comparison between the results obtained using UTD and the moment method solutions for both horizontal and vertical polarizations.

For most of the patterns, agreement is within 3 dB or better. In the specular and forward-scatter regions, the match is within 1 dB or better. However, near backscatter for the 0 degree axial incidence pattern, we have a significant difference. This is a rim-caustic region which involves both front and back rims. We note that this the same region where we had previous differences with the measurements. As discussed in the last chapter, higher-order diffractions may need to be considered to resolve this difference.

Higher-order diffractions probably account for the other differences between the UTD and MM patterns. Double diffractions are significant along the surfaces boundaries at 30, 150, 90, 210, 270, and 330 degrees due to interactions across the endcaps and between front and back rims. The creeping-wave and creeping-wave interactions with the edges are probably significant contributors in the forward-scatter direction. But it is dangerous to speculate without further investigation. Overall, the agreement is reasonable for engineering purposes. At higher frequencies, the accuracy of the first-order UTD solution will get better, due to the greater attenuation of surface waves that cause higher-order effects.

Finally, one might wonder why we need a UTD solution when a more accurate moment method solution is available. The relative calculation times might be worth noting: the UTD result took 0.3 minutes of CPU time to generate the pattern; the moment method result took 3 hours (on a VAX 11/780). The faster calculation time seems to be a reasonable trade-off for accuracy.

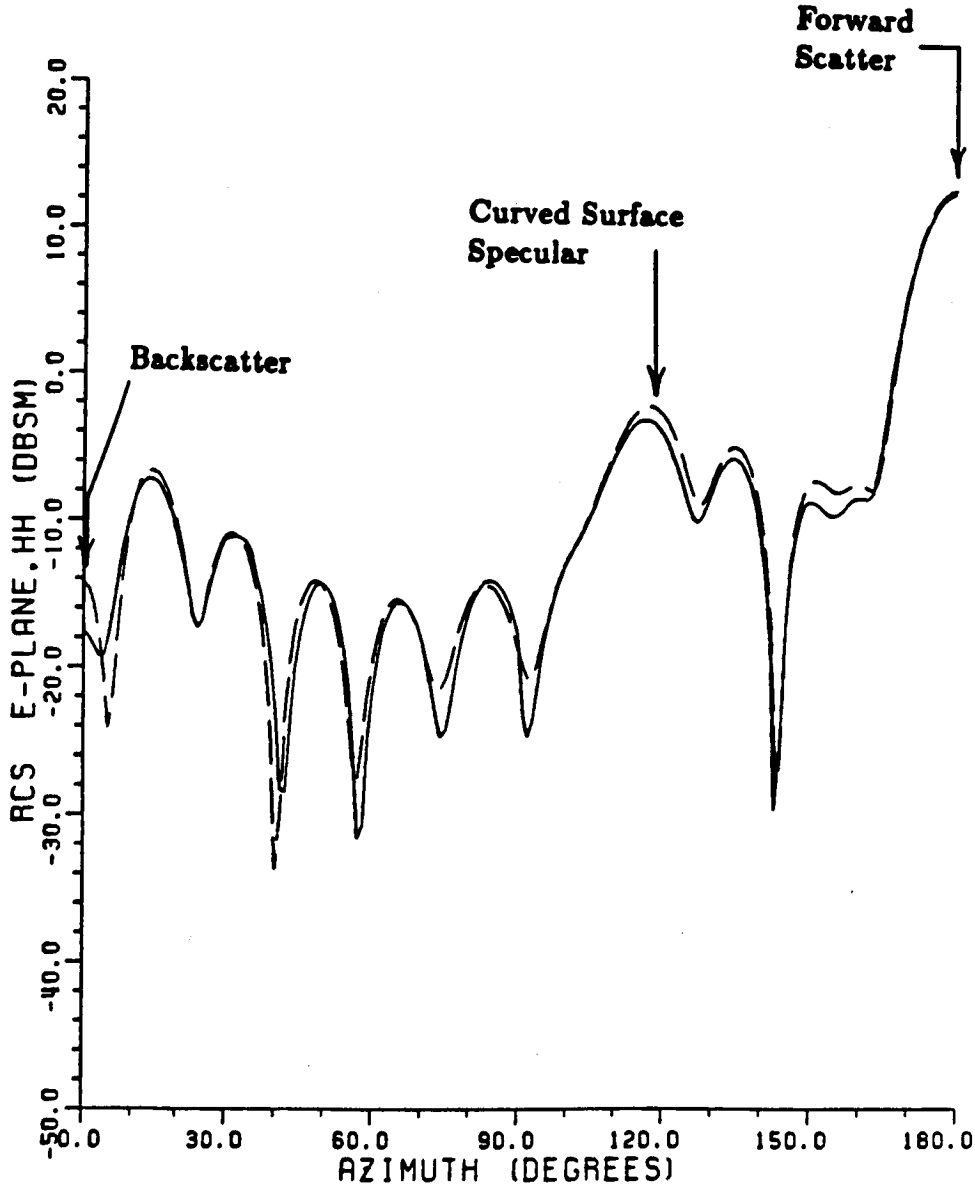

Figure 50: Bistatic principal plane pattern for fixed incidence at $\theta = 0$ degrees and horizontal polarization, obtained using the moment method (dashed line) and UTD (solid line).

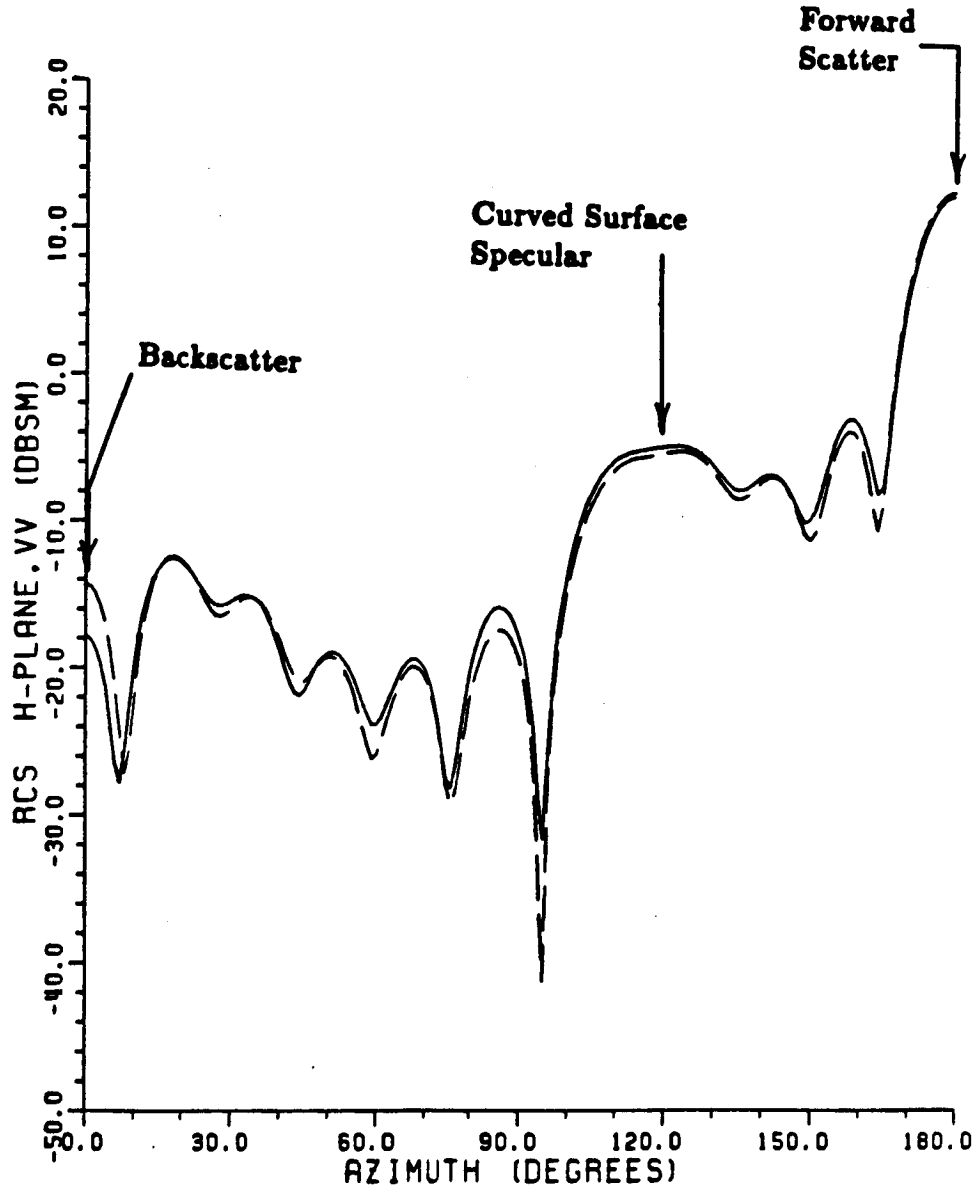

Figure 51: Bistatic principal plane pattern for fixed incidence at $\theta = 0$ degrees and vertical polarization, obtained using the moment method (dashed line) and UTD (solid line).

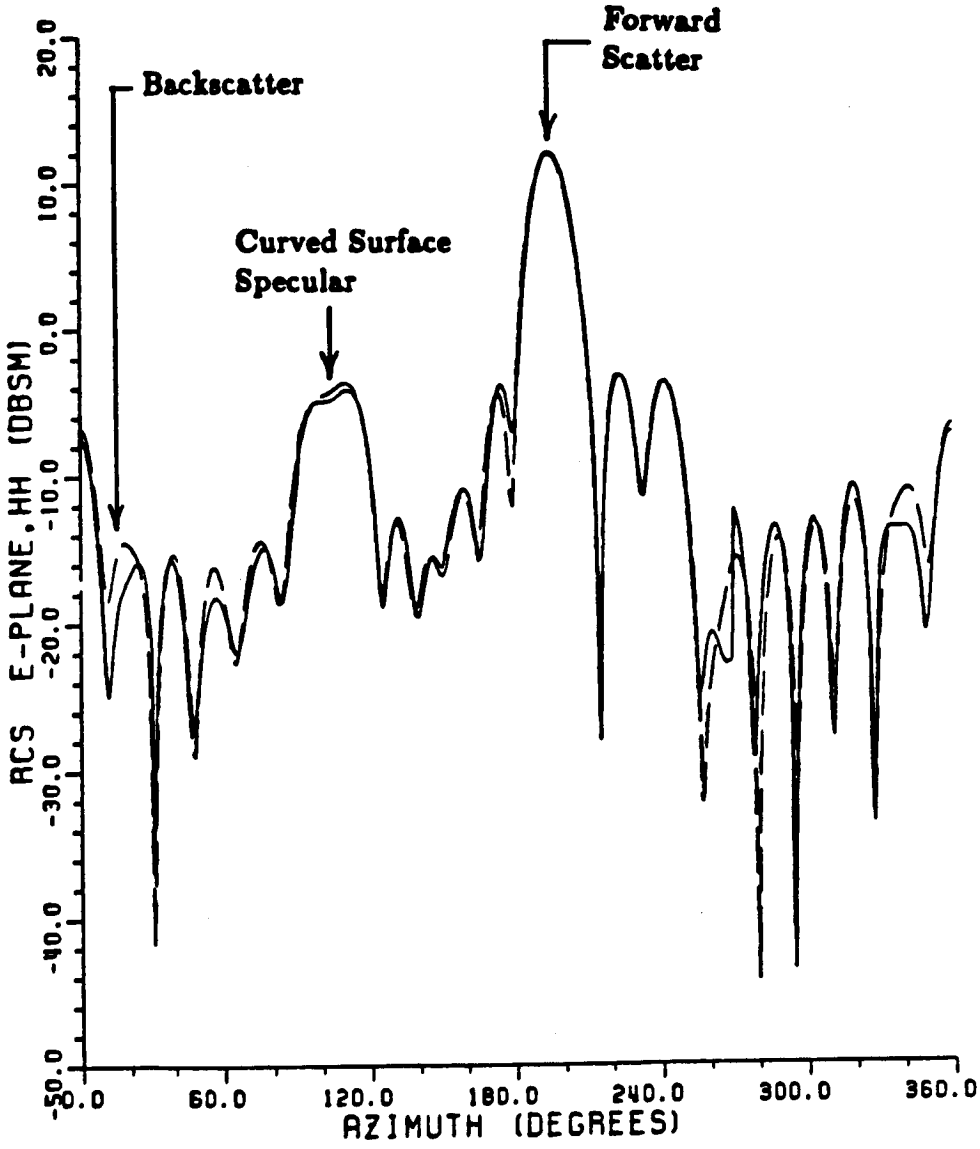

Figure 52: Bistatic principal plane pattern for fixed incidence at $\theta = 15$ degrees and horizontal polarization, obtained using the moment method (dashed line) and UTD (solid line).

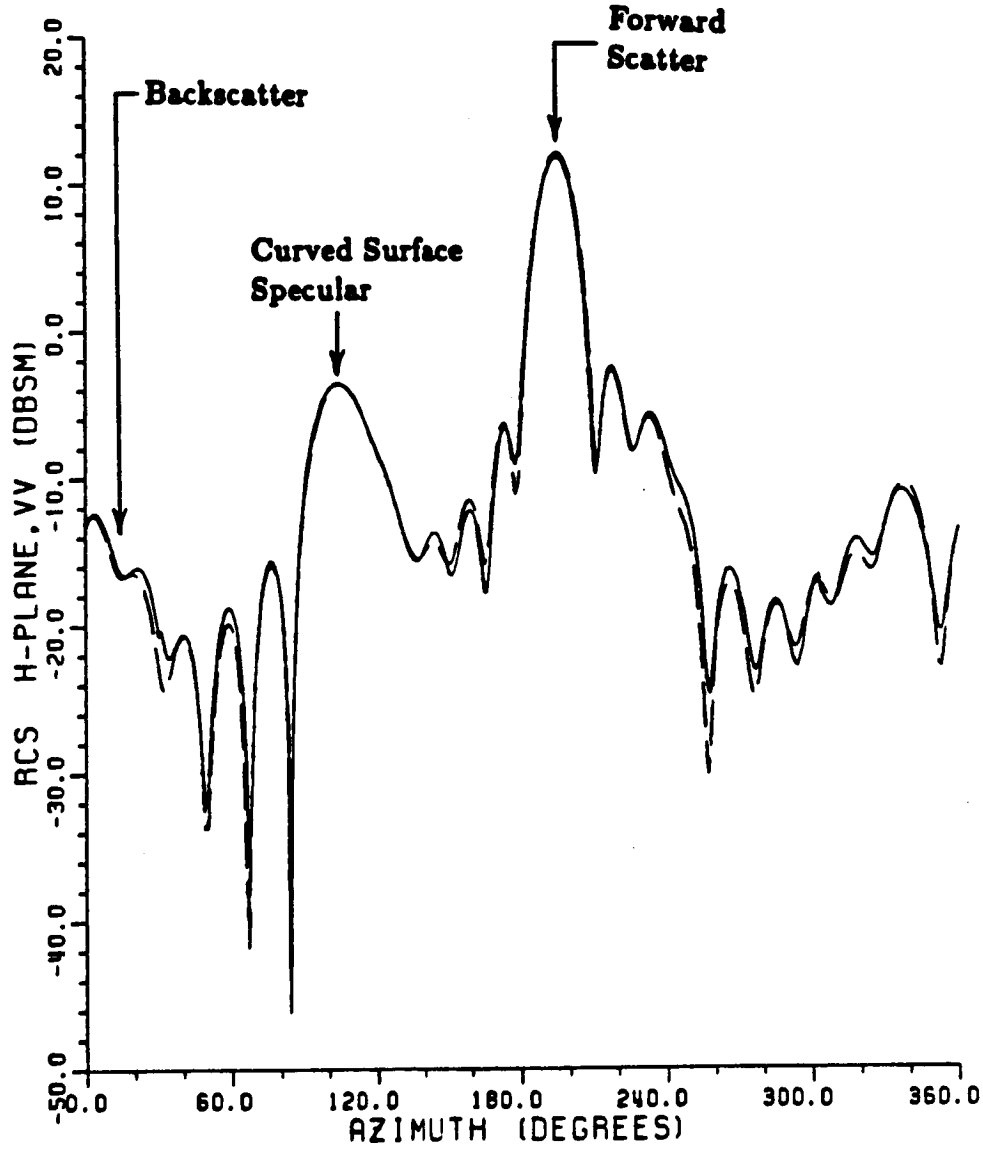

Figure 53: Bistatic principal plane pattern for fixed incidence at $\theta = 15$ degrees and vertical polarization, obtained using the moment method (dashed line) and UTD (solid line).

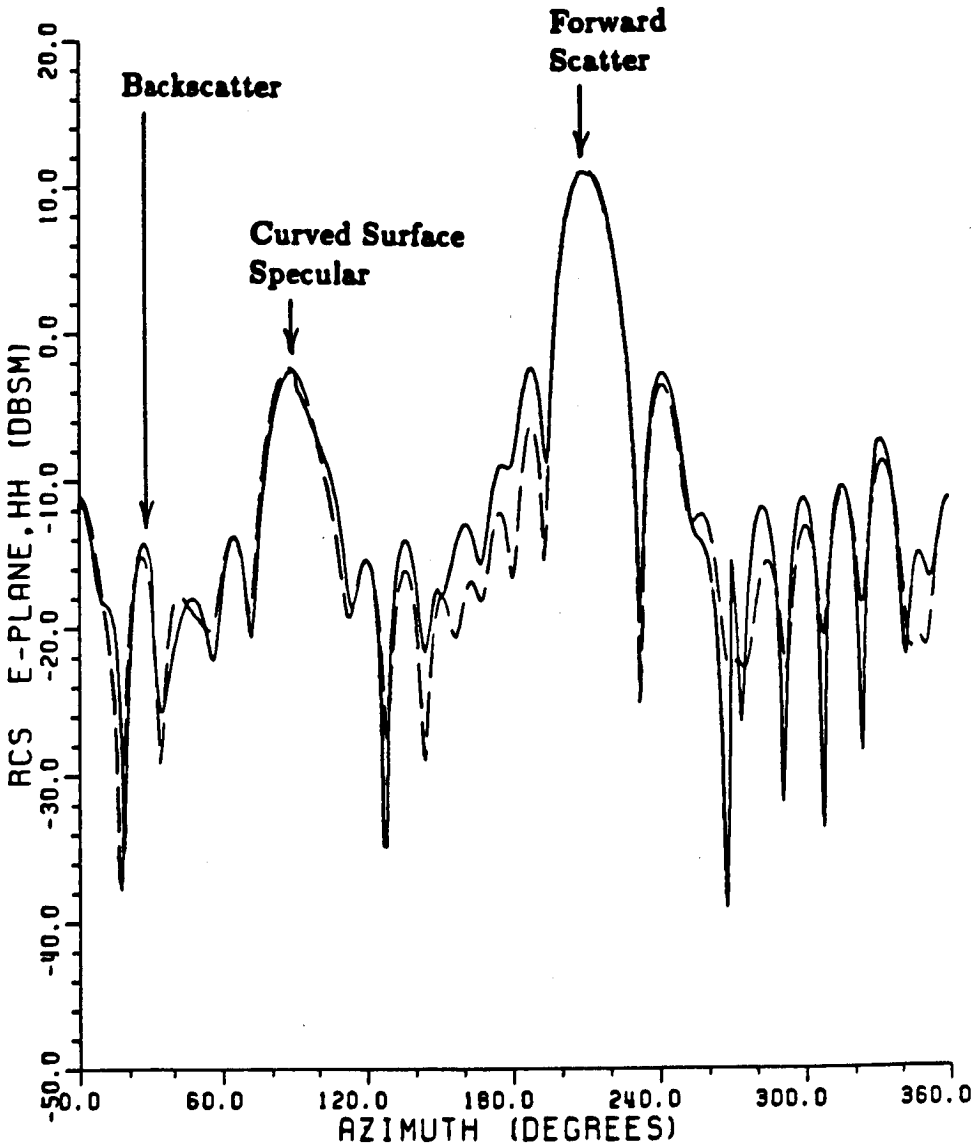

Figure 54: Bistatic principal plane pattern for fixed incidence at $\theta = 30$ degrees and horizontal polarization, obtained using the moment method (dashed line) and UTD (solid line).

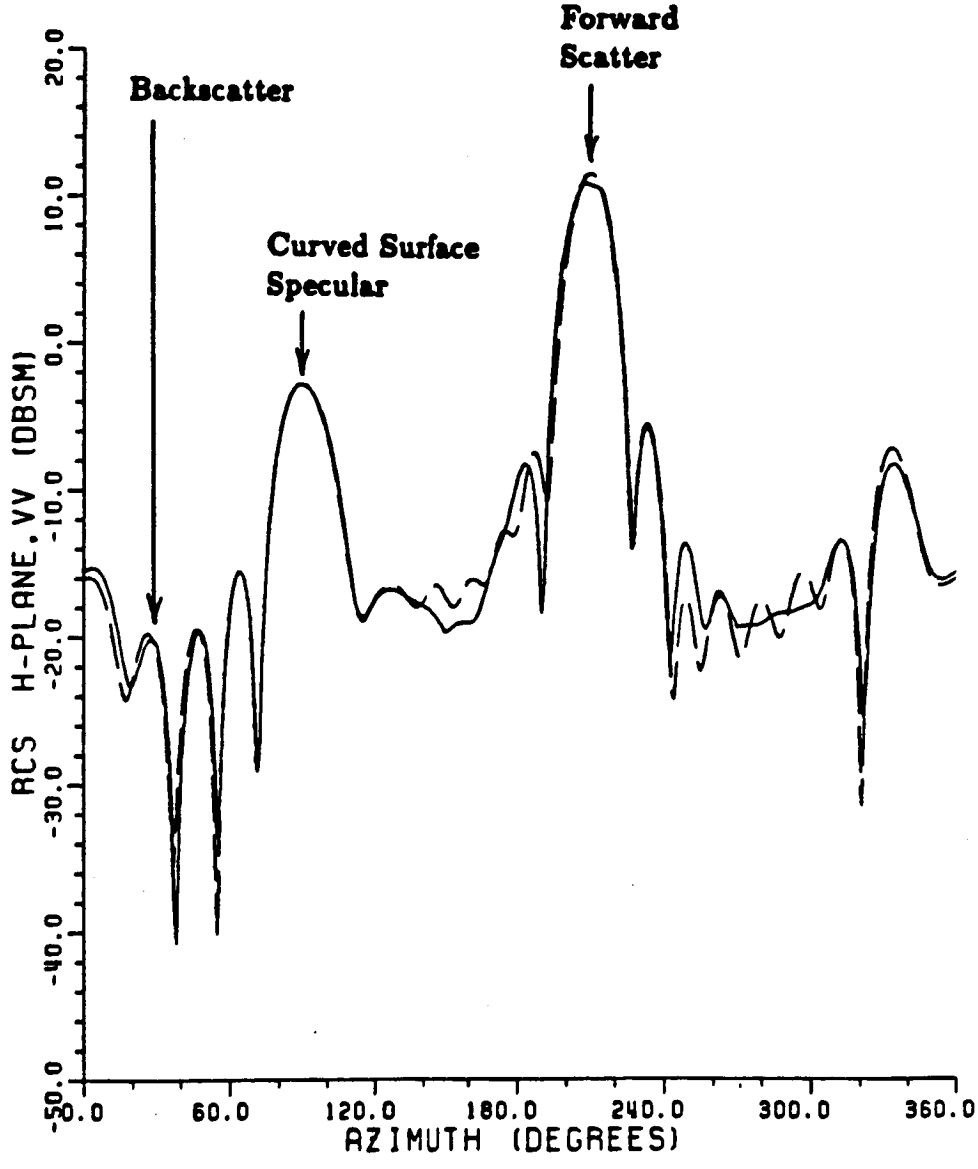

Figure 55: Bistatic principal plane pattern for fixed incidence at $\theta = 30$ degrees and vertical polarization, obtained using the moment method (dashed line) and UTD (solid line).

CHAPTER VIII

Summary and Conclusion

The objective of this work was to solve for the high-frequency scattered fields from a cone frustum. The desired solution needed to be practical—suitable for engineering applications. Thus, we chose a solution based on the methods of the geometric theory of diffraction—for its accuracy, for the physical insight that ray methods provide, and for its ease of application. The original GTD solution for the frustum, which we called the "diffraction-point method solution", provided fairly accurate results, but it failed in the specular region for the curved surface and in the rim-caustic regions.

We wanted to correct the original GTD solution in these regions, but we also wanted to avoid direct switching to alternate solution forms, such as the physical optics solution. The diffraction-point method solution has a simple and elegant form, and the virtues of a simple solution can be appreciated in applications dealing with complicated systems and computer codes. Therefore, to retain the original form, we developed correcting functions, called "transition functions", that modified the terms in the diffraction coefficients. The transition functions provide a uniform solution—in other words, they are modified so that they can be used in all regions. And as demonstrated in the last two chapters, they provide results that compare well with measurements and moment method results.

We have accomplished our objective, but many items still need further inves-

tigation. The following are a few questions and items that need more study:

- Rim-caustic transition functions. A single more general function is needed that works well for all regions, for elliptical as well as circular rims.
- Quasi-near-zone scattering. Can we model the behavior in the reflection caustic regions from far-zone to near-zone? Would it be possible to develop another transition function to do this?
- Scattering outside the principal plane. Do other mechanisms, such as creeping-wave interactions with the edge, become important?
- Higher-order diffraction effects. The development of solutions that consider muliply diffracted rays may extend the UTD solution to lower frequncies.
- Scattering from structures using cone frustums. Some of the applications, such as the scattering from multiple cone-frustum structures in combination with other geometries can be investigated. What shadowing and ray interactions between structures need to be considered?

The author hopes that some of these questions will be answered in future work, and hopefully this report will serve as a basis for that research.

APPENDIX A

Confluent Hypergeometric Functions

The confluent hypergeometric functions (also called Kummer functions) are solutions to the confluent hypergeometric equation,

$$zy''(z) + (b - z)y'(z) - ay = 0. \qquad (A.317)$$

The complete solution is given by,

$$y(z) = A\,\mathbf{M}(a, b, z) + B\,\mathbf{U}(a, b, z) \qquad (A.318)$$

where A and B are are arbitrary constants and $a \neq -n$, $b \neq -m$ (m, n are positive integers).

The confluent hypergeometric functions **M** and **U** have integral, series, and large argument forms. References for this section are [13] and [18]. The integral representation is given by

$$\mathbf{M}(a, b, z) = \frac{\Gamma(b)}{\Gamma(b-a)\Gamma(a)} \int_0^1 e^{zt} t^{a-1} (1-t)^{b-a-1} dt \qquad (A.319)$$
$$Re(b) \geq Re(a) \geq 0$$

$$\mathbf{U}(a, b, z) = \frac{1}{\Gamma(a)} \int_0^\infty e^{-zt} t^{a-1} (1+t)^{b-a-1} dt \qquad (A.320)$$
$$Re(z) \geq 0, Re(a) \geq 0$$

The series form of the functions are

$$\mathbf{M}(a, b, z) = \sum_{n=0}^{\infty} \frac{(a)_n}{(b)_n} \frac{z^n}{n!} \qquad (A.321)$$

$$(a)_n = a(a+1)(a+2)...(a+n-1)$$

$$(a)_0 = 1$$

$$\mathbf{U}(a,b,z) = \frac{\pi}{\sin \pi b}\left\{\frac{\mathbf{M}(a,b,z)}{\Gamma(1+a-b)\Gamma(b)} - z^{1-b}\frac{\mathbf{M}(1+a-b,2-b,z)}{\Gamma(a)\Gamma(2-b)}\right\} \qquad \text{(A.322)}$$

The large argument form, for $|z|$ large, (a and b fixed) is

$$\begin{aligned}\mathbf{M}(a,b,z) = {} & \frac{\Gamma(b)}{\Gamma(b-a)}e^{\pm j\pi a}z^{-a}\cdot \\ & \cdot\left\{\sum_{n=0}^{R-1}\frac{(a)_n(1+a-b)_n}{n!}(-z)^{-n}+O(|z|^{-R})\right\} \\ & +\frac{e^z z^{a-b}}{\Gamma(a)}\cdot \\ & \cdot\left\{\sum_{n=0}^{S-1}\frac{(b-a)_n(1-a)_n}{n!}z^{-n}+O(|z|^{-S})\right\}\end{aligned} \qquad \text{(A.323)}$$

where the sign is $(+)$ if $-\frac{1}{2}\pi < \arg z < \frac{3}{2}\pi$, or $(-)$ if $-\frac{3}{2}\pi < \arg z < -\frac{1}{2}\pi$.

$$\mathbf{U}(a,b,z) = z^{-a}\left\{\sum_{n=0}^{R-1}\frac{(a)_n(1+a-b)_n}{n!}(-z)^{-n}+O(|z|^{-R})\right\} \qquad (A.324)$$

where $-\frac{3}{2}\pi < \arg z < \frac{3}{2}\pi$.

The two confluent hypergeometric functions of interest in this work are $\mathbf{M}(1,2.5,-z)$ and $\mathbf{U}(1,2.5,-z)$. For small values of the argument, the series form should be used. The series form is given by

$$\mathbf{M}(1,2.5,-z) = \frac{3}{2}e^{-z}\sum_{n=0}^{\infty}\frac{z^n}{\left(n+\frac{3}{2}\right)n!} \qquad \text{(A.325)}$$

$$\mathrm{U}(1,2.5,-z) = -\frac{2}{3}\mathrm{M}(1,2.5,-z) + \frac{\sqrt{\pi}}{2(-z)^{\frac{3}{2}}}e^{-z} \qquad \text{(A.326)}$$

For large arguments, $|z|$ large,

$$\mathrm{M}(1,2.5,-z) = \frac{3}{4}\sqrt{\pi}e^{\pm j\frac{3}{2}\pi}\frac{e^{-z}}{z^{\frac{3}{2}}} + \frac{3}{2}\frac{1}{z}\sum_{n=0}^{S-1}\frac{(-.5)_n}{z^n} \qquad \text{(A.327)}$$

$$\mathrm{U}(1,2.5,-z) = \frac{1}{-z}\sum_{n=0}^{S-1}(-.5)_n z^{-n} \qquad \text{(A.328)}$$

Usually three terms, $S = 3$, are sufficient.

APPENDIX B

Bessel and Struve Functions

In Chapter 5, we use the zero and first order Bessel and Struve functions. These functions can be calculated by using a power series for small values of the argument, or by using the asymptotic form for large values of the argument. The references used are [18,19].

The power series expansions are given by the following:

$$J_n(x) = \sum_{k=0}^{\infty} \frac{(-1)^k (x/2)^{2k+n}}{k!\Gamma(k+1+n)} \tag{B.329}$$

$$J_0(x) = \sum_{k=0}^{\infty} \frac{(-1)^k (x/2)^{2k}}{(k!)^2} \tag{B.330}$$

$$J_1(x) = \frac{x}{2} \sum_{k=0}^{\infty} \frac{(-1)^k (x/2)^{2k}}{(k+1)(k!)^2} \tag{B.331}$$

$$\mathbf{H}_n(x) = (x/2)^{n+1} \sum_{k=0}^{\infty} \frac{(-1)^k (x/2)^{2k}}{\Gamma(k+1.5)\Gamma(k+n+1.5)} \tag{B.332}$$

$$\mathbf{H}_0(x) = \frac{2}{\pi} \sum_{k=1}^{\infty} (-1)^{k+1} x^{2k-1} \left[\frac{2^k k!}{(2k)!} \right]^2 \tag{B.333}$$

$$\mathbf{H}_1(x) = \frac{2}{\pi} \sum_{k=1}^{\infty} (-1)^{k+1} x^{2k} (2k+1) \left[\frac{2^{k+1}(k+1)!}{(2(k+1))!} \right]^2 . \tag{B.334}$$

In terms of the confluent hypergeometric function, the Bessel function is given by:

$$J_n(x) = \frac{(x/2)^n e^{-jx}}{\Gamma(n+1)} \mathrm{M}(n+.5, 2n+1, j2x)\,. \qquad (B.335)$$

The following are the asymptotic expansions for large $|x|$:

$$\begin{aligned} J_n(x) \;\sim\; & \sqrt{\frac{2}{\pi x}} \left[\cos\psi \left(1 - \frac{\alpha_1\alpha_2}{2!} + \frac{\alpha_1\alpha_3\alpha_5\alpha_7}{4!} - \cdots \right) \right. \\ & \left. - \sin\psi \left(\frac{\alpha_1}{1!} - \frac{\alpha_1\alpha_3\alpha_5}{3!} + \cdots \right) \right] \end{aligned} \qquad (B.336)$$

$$\begin{aligned} Y_n(x) \;\sim\; & \sqrt{\frac{2}{\pi x}} \left[\sin\psi \left(1 - \frac{\alpha_1\alpha_2}{2!} + \frac{\alpha_1\alpha_3\alpha_5\alpha_7}{4!} - \cdots \right) \right. \\ & \left. + \cos\psi \left(\frac{\alpha_1}{1!} - \frac{\alpha_1\alpha_3\alpha_5}{3!} + \cdots \right) \right] \end{aligned} \qquad (B.337)$$

where

$$\psi = x - \frac{n\pi}{2} - \frac{\pi}{4} \qquad (B.338)$$

$$\alpha_k = \frac{4n^2 - k^2}{8x} \qquad (B.339)$$

and

$$\begin{aligned} \mathrm{H}_0(x) \;\sim\; & \frac{2}{\pi} \left[\frac{1}{x} - \frac{1}{x^3} + \frac{1^2 \cdot 3^2}{x^5} - \frac{1^2 \cdot 3^2 \cdot 5^2}{x^7} + \cdots \right] \\ & + Y_0(x) \end{aligned} \qquad (B.340)$$

$$\begin{aligned} \mathrm{H}_1(x) \;\sim\; & \frac{2}{\pi} \left[1 + \frac{1}{x^2} - \frac{1^2 \cdot 3}{x^4} + \frac{1^2 \cdot 3^2 \cdot 5}{x^6} - \cdots \right] \\ & + Y_1(x)\,. \end{aligned} \qquad (B.341)$$

APPENDIX C

Computer Programs

This appendix contains some of the computer subroutines and functions that were used to calculate the confluent hypergeometric functions and the integrals used for the partial rim corrections. The programs are written in FORTRAN 77. They are based on the material found in Chapter 5 and Appendix A.

```
C*******************************************************
C       This function is the confluent
C       hypergeometric function of
C       U(1.,2.5,Z) in series form.
C       Used with small values of the
C       argument (magnitude of Z < 5 ). WE 8/9/85
C
        COMPLEX FUNCTION UFS(Z)
C-------------------------------------------------------
C       Z = function argument, complex
C-------------------------------------------------------
        COMPLEX CJ,MFS,Z,Z1,Z2
C-------------------------------------------------------
        CJ=(0.,1.)
        PI=3.14159265
C-------------------------------------------------------
        Z1=-(2./3.)*MFS(1.,2.5,Z)
        Z2=.5*SQRT(PI)*CEXP(Z)/(Z**1.5)
C       Z2 can become infinite if Z=0.
        UFS=Z1+Z2
        RETURN
        END
C*******************************************************
C       This function is the confluent
C       hypergeometric function of
C       U(1.,2.5,Z) in asymptotic form.
C       Used with large values of
C       the argument (magnitude of Z >> 1 ).
C
        COMPLEX FUNCTION UFL(Z)
C-------------------------------------------------------
C       Z = function argument, complex
C-------------------------------------------------------
        COMPLEX S,Z
C-------------------------------------------------------
        S=(0.,0.)
C-------------------------------------------------------
C       J is the number of terms.
        J=3
C-------------------------------------------------------
        DO 10 N=0,J-1
        X=N
        S=(PH(-.5,N)/(-Z)**X)+S
10      CONTINUE
        UFL=S/Z
C-------------------------------------------------------
        RETURN
        END
```

```
C*****************************************************
C       This function is used with functions UFL.
C       (It is often represented by the
C       Pochhammer symbol.)
C
        FUNCTION PH(A,N)
        P=1.
        IF(N.EQ.0)THEN
           PH=1.
        ELSE IF(N.EQ.1)THEN
           PH=A
        ELSE IF(N.GE.2)THEN
           DO 10 K=0,N-1
           P=(A+K)*P
10         CONTINUE
           PH=P
        ENDIF
C-------------------------------------------------
        RETURN
        END
C*****************************************************
C       This function is the confluent
C       hypergeometric function of M(A,B,Z) in
C       series form.  Used with small values of
C       the argument (magnitude of Z < 5 ).
C       WE 8/9/85
C
        COMPLEX FUNCTION MFS(A,B,Z)
C-------------------------------------------------
C       A,B = parameters of the hypergeometric
C             function (contants)
C       Z = function argument, complex
C-------------------------------------------------
        DIMENSION CN(0:40)
        COMPLEX SS,Z
C-------------------------------------------------
        SS=(0.,0.)
C-------------------------------------------------
        X=CABS(Z)
C-------------------------------------------------
C       K = number of terms used in the series
C
        K=3.*X+11.
        KMAX=40.
        IF(K.GT.KMAX)K=KMAX
```

```
C-------------------------------------------------
C       Small argument.
C
        IF(X.LT..01)MFS=(1.,0.)
C-------------------------------------------------
C       Series form.
C
        IF(X.GE..01)THEN
           CALL CS(A,B,K,CN)
           J=K-1
              DO 10 N=1,J
              M=J-(N-1)
              SS=Z*(CN(M)+SS)
10            CONTINUE
           SS=1.+SS
           MFS=SS
        ENDIF
C-------------------------------------------------
        RETURN
        END
C*************************************************
C       This subroutine calculates the constants
C       used in the series form of the
C       hypergeometric function M(a,b,jX).
C
        SUBROUTINE CS(A,B,K,CN)
C-------------------------------------------------
C       A,B = parameters of the hypergeometric
C             function
C       K = number of terms in the series
C       CN = array of constants to be returned
C-------------------------------------------------
        DIMENSION CN(0:40)
C-------------------------------------------------
        CN(0)=1.
C-------------------------------------------------
        DO 10 N=1,40
        X=N
        IF(N.LE.K)THEN
           CN(N)=CN(N-1)*(A+X-1)/((B+X-1)*X)
        ELSE
           CN(N)=0.
        ENDIF
10      CONTINUE
        RETURN
        END
```

```
C*************************************************
C       This function is the confluent
C       hypergeometric function of M(1.5,2.5,Z)
C       in asymptotic form.  Used with large
C       values of the argument
C       (magnitude of Z >> 1 ).  WE 85
C
        COMPLEX FUNCTION MFL(Z)
C-------------------------------------------------
C       Z = function argument, complex
C-------------------------------------------------
        COMPLEX C1,C2,CJ,S,Z
C-------------------------------------------------
        PI=3.14159265
        CJ=(0.,1.)
        S=(0.,0.)
C-------------------------------------------------
        ZI=AIMAG(Z)
        ZM=CABS(Z)
        IF(ZI.EQ.-ZM)C1=.75*SQRT(PI)
     1  *CEXP(-CJ*1.5*PI)/(Z**1.5)
        IF(ZI.EQ.ZM)C1=.75*SQRT(PI)
     1  *CEXP(CJ*1.5*PI)/(Z**1.5)
C-------------------------------------------------
C       J is the number of terms.
        J=3
C-------------------------------------------------
        DO 10 N=0,J-1
        X=N
        S=(PH(-.5,N)/Z**X)+S
10      CONTINUE
        C2=(1.5*CEXP(Z)/Z)*S
        MFL=C1+C2
C-------------------------------------------------
        RETURN
        END
```

```
C*************************************************
C       This subroutine approximately computes
C       the integrals used in the transition
C       functions from X1 to X2, for small
C       values of U.
C
        SUBROUTINE INTGRL(X1,X2,U,NINT,FX,ECODE)
C-------------------------------------------------
C       X1,X2 = limits of integration
C       U = variable in the exponential
C           (a real number with mag. < 8.)
C       NINT = 1   cos(x) * exp(j U cos(x))
C              2   ( cos(x)**2 ) * exp(j U cos(x))
C              3   ( sin(x)**2 ) * exp(j U cos(x))
C       FX = computed value of the integral
C       ECODE = error code
C
C       The subroutines INCOS and INSINCOS are
C       used with this routine.
C-------------------------------------------------
        COMPLEX CJ,FX,SUM
        DIMENSION FI(0:25),C(0:23),FACT(0:23)
C-------------------------------------------------
        DATA PI,TPI,DR/3.14159265,6.28318537,
     1  0.017453292/
        DATA FACT/1.,1.,2.,6.,24.,120.,720.,5040.,
     1  40320.,362880.,3628800.,39916800.,
     2  479001600.,6227020800.,8.7178291E10,
     3  1.3076743E12,2.0922789E13,3.5568742E14,
     4  6.4023737E15,1.2164510E17,2.4329020E18,
     5  5.1090942E19,1.1240007E21,2.5852016E22/
        CJ=(0.,1.)
C
        XMIN=.001
        NMAX=23
C-------------------------------------------------
        IF(ABS(U).GT.8.)THEN
           ECODE=4.
           GO TO 999
        ENDIF
C-------------------------------------------------
        DO 10 K=0,23
           C(K)=U**K/FACT(K)
           IF(ABS(C(K)).LT.XMIN)THEN
              NMAX=K
              GO TO 20
           ENDIF
10      CONTINUE
```

```
C-------------------------------------------------
20      CONTINUE
        SUM=(0.,0.)
        IF(NINT.EQ.1)THEN
           CALL INCOS(X1,X2,NMAX+1,FI)
              DO 30 K=0,NMAX
              SUM=SUM+(CJ**K)*C(K)*FI(K+1)
30            CONTINUE
        ELSE IF(NINT.EQ.2)THEN
           CALL INCOS(X1,X2,NMAX+2,FI)
              DO 40 K=0,NMAX
              SUM=SUM+(CJ**K)*C(K)*FI(K+2)
40            CONTINUE
        ELSE IF(NINT.EQ.3)THEN
           CALL INSINCOS(X1,X2,NMAX,FI)
              DO 50 K=0,NMAX
              SUM=SUM+(CJ**K)*C(K)*FI(K)
50            CONTINUE
        ENDIF
C-------------------------------------------------
        FX=SUM
999     CONTINUE
        RETURN
        END
C*************************************************
C       This subroutine computes the integral of
C       the cosine to the power N. It computes up
C       to a specified value of N and returns
C       the result in an array where the array
C       subscript corresponds to the value of N.
C
        SUBROUTINE INCOS(X1,X2,NMAX,FI)
C-------------------------------------------------
C       X1,X2 = limits of integration (radians)
C       NMAX = maximum value of power N
C              (an integer)
C       FI = the array of computed integrals
C-------------------------------------------------
        DIMENSION FI(0:25),F1(0:25),F2(0:25)
C-------------------------------------------------
        F1(0)=X1
        F2(0)=X2
        FI(0)=X2-X1
        F1(1)=SIN(X1)
        F2(1)=SIN(X2)
        FI(1)=F2(1)-F1(1)
        F1(2)=SIN(2.*X1)/4.+X1/2.
        F2(2)=SIN(2.*X2)/4.+X2/2.
        FI(2)=F2(2)-F1(2)
```

```
      IF(NMAX.GT.2)THEN
        DO 10 K=3,NMAX
        A=K
        F1(K)=(SIN(X1)*(COS(X1)**(K-1))/A)+
     1    ((A-1.)*F1(K-2)/A)
        F2(K)=(SIN(X2)*(COS(X2)**(K-1))/A)+
     1    ((A-1.)*F2(K-2)/A)
        FI(K)=F2(K)-F1(K)
10      CONTINUE
      ENDIF
      RETURN
      END
C*****************************************************
C     This subroutine computes the integral of
C     the cosine to the power N multiplied by
C     the sine squared. It computes up to a
C     specified value of N and returns the
C     result in an array where the array
C     subscript corresponds to the value of N.
C
      SUBROUTINE INSINCOS(X1,X2,NMAX,FI)
C-----------------------------------------------------
C     X1,X2 = limits of integration (radians)
C     NMAX = maximum value of power N
C            (an integer)
C     FI = the array of computed integrals
C-----------------------------------------------------
      DIMENSION FI(0:25),F1(0:25),F2(0:25),
     1  FCOS(0:25)
C-----------------------------------------------------
      CALL INCOS(X1,X2,NMAX,FCOS)
C
      DO 10 K=0,NMAX
      A=K
      F1(K)=-SIN(X1)*COS(X1)**(K+1)
      F2(K)=-SIN(X2)*COS(X2)**(K+1)
      FI(K)=((F2(K)-F1(K))+FCOS(K))/(A+2.)
10    CONTINUE
C
      RETURN
      END
```

References

[1] Chiang,K-C.,"Bistatic Scattering from a Finite Circular Cylinder," M.S. Thesis, The Ohio State University, Dept. of Electrical Engineering, Dec. 1984.

[2] Keller,J.B., "Geometrical Theory of Diffraction," *J. Opt. Soc. of America*, vol.52, no.2, Feb. 1962, p.116-130.

[3] Kouyoumjian,R.G., and P.H. Pathak, "A Uniform Geometrical Theory of Diffraction for an Edge in a Perfectly Conducting Surface," *Proc. IEEE*, vol. 62, Nov. 1974, p.1448-1461.

[4] Ross,R.A., "Bistatic Scattering Matrix for a Frustum," *IEEE Trans. on Antennas and Propagation*, vol. AP-17, Jan. 1969, p.877-882.

[5] Ruck,G.T., editor, *Radar Cross Section Handbook, Vol. 1*, New York:Plenum Press, 1970, p.413-416.

[6] Bectel,M.E.,"Application of Geometrical Diffraction Theory to Scattering from Cones and Disks," *Proc. IEEE*, vol.53,Aug.1965, p.877-882.

[7] Ryan,C.E.,Jr., and L. Peters,Jr., "Evaluation of Edge Diffracted Fields Including Equivalent Currents for the Caustic Regions," *IEEE Trans. on Antennas and Propagation*, vol.AP-17, May 1969, p.292-299.

[8] Chu,T.T., "First Order Uniform Geometrical Theory of Diffraction Analysis of the Scattering of Smooth Structures," Ph.D. Dissertation, The Ohio State

University, Dept. of Electrical Engineering, Dec. 1982.

[9] Ryan,C.E.,Jr., "A Geometrical Theory of Diffraction Analysis of the Radar Cross Section of a Sectionally Continuous Second-Degree Surface of Revolution," Technical Report 2430-4, March 1968, ElectroScience Laboratory, The Ohio State University, p.150-151.

[10] Kouyoumjian,R.G., "Asymptotic High-Frequency Methods," *Proc. IEEE*, vol.53, Aug. 1965, p.864-876.

[11] Pathak,P.H., W.D. Burnside, and R.J. Marhefka, "A Uniform GTD Analysis for the Diffraction of Electromagnetic Waves by a Smooth Convex Surface," *IEEE Trans. on Antennas and Propagation*, vol.AP-28, Sept. 1980, p.631-642.

[12] Volakis,J.L., and L.Peters,Jr., "Evaluation of Reflected Fields at Caustic Regions Using a Set of GO Equivalent Line Currents," *IEEE Trans. on Antennas and Propagation*, vol.AP-33, Aug.1985, P.860-866.

[13] Arfken,G., *Mathematical Methods for Physicists*, 2nd ed., Academic Press,Inc., 1970, p.103-106.

[14] Balanis,C.A., *Antenna Theory: Analysis and Design*, New York: Harper and Row Publishers,Inc., 1982, p.515-520.

[15] Sikta,F.A., W.D.Burnside, T.T.Chu, and L.Peters,Jr., "First-Order Equivalent Current and Corner Diffraction Scattering from Flat Plate Structures," *IEEE Trans. on Antennas and Propagation*, vol.AP-31, no.4, July 1983, p.584-589.

[16] Terzuoli,A.J.,Jr., C.W.Chuang, and L.Peters,Jr., "An Integral Equation Approach to Obtain the Significant Parameters of Dihedral Corrugated Horns," Report 3821-2, July 1976, The Ohio State University ElectroScience Laboratory, Department of Electrical Engineering.

[17] Chuang,C.W.,"Scattering by a Rotationally Symmetric Conducting Body," Technical Report 714614-2, Aug. 1983, The Ohio State University, ElectroScience Laboratory.

[18] Abramowitz,M., and I.A.Stegun,editors, *Handbook of Mathematical Functions*, New York: Dover Publications,Inc., 1972, p.504-535.

[19] Tuma,J.J., *Engineering Mathematics Handbook*, 2nd ed., New York: McGraw-Hill Book Co.,Inc., 1979.